Development of Spectroscopic Techniques for Potential Environmental and Biomedical Applications

THESIS

SUBMITTED FOR THE DEGREE OF

DOCTOR OF PHILOSOPHY (TECH.)

IN

APPLIED OPTICS AND PHOTONICS

BY

SOUMENDRA SINGH

DEPARTMENT OF APPLIED OPTICS AND PHOTONICS
UNIVERSITY OF CALCUTTA
INDIA

2021

To
Every Individual
Who Believed in Me

Acknowledgments

Undertaking this Ph.D. has been a truly life-shifting experience for me and it would not have been possible to do without the support and guidance that I received from many people.

First of all, I take this opportunity to express my sincere gratitude to my advisor Prof. Samir Kumar Pal, who allowed me to have a wonderful journey of Ph.D. I am extremely indebted to him for being an exceptional mentor. His all-round expertise, insight into various experimental problems, wisdom, and inspirational endeavors have allowed my research skills to develop, my creativity to flourish along with getting shaped as a working researcher. He has provided me with many opportunities to gain scientific experience, allowing me to explore new areas of research, interact and collaborate with talented researchers from several different national and international institutes. If it weren't for his ideas, constant support, guidance, motivation, and patience, none of this work would have been possible. He has taught me so much, inspired me to work hard, always taken time to listen to my crazy ideas, and made these years so enjoyable. I could not have wished for a better advisor. Thank you, Sir, for everything you have done for me.

I would like to thank Dr. Amitabha Mitra, my associate guide for being a constant support and motivation throughout this journey. His useful ideas and scientific inputs helped me to consolidate my work faster and in an effective manner. I wish to express sincere thankfulness to Prof. Sanjay K. Ghosh, Department of Physics, Bose Institute, for his motivational support and constant encouragement during this journey.

I have enjoyed fruitful collaborations with Prof. Saleh A. Ahmed, Dr. Ahmed Alharbi, and Dr. Rami J. Obaid, Dr. Ahmed M. Hameed from Department of Chemistry, Faculty of Applied Sciences, Umm Al-Qura University, Makkah, Saudi Arabia; Dr. Anirban Bhunia, Department of Biophysics, Bose Insitute; Prof. Maitree Bhattacharyya, Department of Biochemistry, University of Calcutta; Dr. Surajit Bose, Bharat Sevashram Sangha Hospital.

Great appreciation is extended to S N Bose National Centre for Basic Sciences staff and faculty members for their assistance in my research career. I owe a special thanks to the

Department of Technical Research Centre, Department of Science and Technology for funding the projects.

I'd like to express my sincere thanks to all my colleagues and juniors for providing a stimulating and enriching environment. Special thanks to Dr. Nabarun Polley for helping me at the initial stage of my research work. I am grateful to Animesh, Oindrila, Amrita, and Aniruddha for helping me out from many difficulties during my research works. My sincere appreciation goes to all the present group members: Animesh, Deep Shikha, Damayanti, Priya, Tuhin, Jayita, Aniruddha, Probir, Amrita, Ria, Susmita, Dipanajan, Nur, Arka, Pritam, Lopa, Neha, Alisha, and Nairit for providing a homely and a cheerful environment, and also for assisting me in research. I would like to mention Animesh and Oindrila's name for their gigantic cooperation and support in my research.

Finally, I would like to express my gratitude to my family who supported me through thick and thin, with love, affection, and patience. Without their sacrifices, moral supports, and blessings the thesis would not have taken its shape.

(Soumendra Singh)
Department of Chemical Biological and Macromolecular Sciences,
S N Bose National Centre for Basic Sciences,
Salt Lake, Kolkata 700106, India
Dated:

Contents

Chapter 1

Introduction

1.1. Background:

The use of light for environmental pollution monitoring and medical diagnosis/therapy is unanimous [1,2]. High sensitivity, a wide range of applications, lesser sample preparation or in-situ measurements, well-resolved and high-resolution spectra, adaptability with all sample types, and simpler instrumentation techniques are significant advantages of optical spectroscopic techniques over other methods. In recent years, spectroscopic techniques have come to be regarded as attractive and promising analytical tools for analyses conducted in research and industrial laboratories [2,3]. These techniques are increasingly considered by researchers as an obvious solution. This trend stems from instrumental developments, the extensive use of computers, and the development of appropriate chemo-metric procedures. Daily, new applications of spectroscopic techniques in the fields of biomedical and environmental analysis are being demonstrated and published.

Spectroscopy is a broad field in which many sub-disciplines exist, each with numerous implementations of specific spectroscopic techniques [4]. Detection of individual atmospheric constituents with optical methods is based on some kind of selective interaction process between radiation and matter [5]. Considering the detection of gaseous species, the main interaction processes are (a) Raman scattering, (b) fluorescence emission, and (c) absorption processes [6-8]. During the last quarter of the century, there has been a tremendous revolution in the use of instrumentation and spectroscopic techniques in the field of meteorological research and air quality control [9,10]. The dynamically changing climatic

conditions and their adverse effects on life make it extremely important to detect and quantify the composition of the air around us [11]. Various spectroscopic techniques and interferometers provide us greater insight into the composition of matter and suspended particulates [12]. Remote sensing of physically inaccessible locations or locations unfit for human presence has always been a challenge for scientists and technologists. For example, detection of poisonous gasses in coal mines, volcanic eruption sites, and probing the composition of air in upper atmosphere for efficient meteorological applications is only achievable by remote sensing techniques which are contemporary, automated and remotely controlled. The demand is to develop sensors and instruments which are a cheap alternative to costly bench-top instruments to be easily "spent" in potentially dangerous sites [13].

On the other hand, the interaction of light within biological tissue has been used to recognize disease since the mid-1800. The recent developments of small light sources, detectors, and fiber optic probes provide opportunities to quantitatively measure these interactions, which yield information for diagnosis at the biochemical, structural, or physiological level within intact tissues. The interaction of light with biological medium covers the general field of biomedical optics and it has its own role in developing different modern clinical diagnostic and therapeutic techniques. The contemporary challenges in the above-mentioned fields include the design and realization of low-cost techniques without compromising the sensitivity and overall performance of the device.

1.2. Introduction:

In view of recent scientific developments, photon-based detectors and optical fiber-based light probes have made significant advancements towards the quality of measurements and diagnostic techniques, resulting in greater insight into the macromolecular light interactions

on biologicals and meteorological targets. Better quality of receivers, spectroscopic advancements, and novel electro-optical strategies have seen significant advancements in recent times. In the following sections, few contemporary similar techniques with possible environmental and biomedical applications have been discussed.

1.2.1. Optical Spectroscopy in the Environmental Application:

The use of optical techniques for various meteorological applications is widespread. The use of optical sun photometers to costly optical Raman Lidars is widespread which proves the strong presence of optical spectroscopy as a probing tool [14]. In this section, we will discuss few optical techniques used in environmental applications. Arguably, spectroscopy can be identified as the only technique that may be utilized for remote probing of the environment. Remote sensing in form of continuous monitoring is important to study the temporal and spatial nature of atmospheric parameters [15]. In situ, optical techniques are in use commonly for atmospheric research, which includes short-lived reactive species that play important role in driving the dynamics of the environment, isotopologue concentrations, and the attributes of particles under optical, regime which substantially change radiative forcing and affect long term weather. Data obtained using spectroscopic techniques determine the air quality index, identification of sources of atmospheric sources of pollution, measuring the amplitude and spread of atmospheric enforcing factors, enabling actions with policies, and reforming atmospheric management at global levels. For the above-mentioned reasons, UV/VIS spectrometers utilizing Beer-Lambert law form the basis of almost all laboratories around the world. This is well applicable for water-soluble as well as other samples soluble in a variety of solvents. Recent advances in environmental spectroscopic techniques have been made both on the instrumentation aspect and on the spectrum analysis

side. Continuous development in the instrumentation domain continues to be worked upon using the latest developments in optical sources, measurement strategies, and novel detection strategy. Additionally, more capability and the quest of acquiring high-resolution information over time and geographical extent provides encouragement to continue to promote the importance of novel spectral analysis strategies. So, with the improvement of better techniques, primitive spectroscopic techniques are evolving in both scope and performance.

1.2.2. Optical Spectroscopy in the Biomedical Application:

Spectroscopic techniques are not limited to environmental applications only. Optical interactions with biological targets are a matter of live research throughout the world. Especially, non-invasive methods of disease diagnosis are gaining popularity as they have shown immense potential in replacing conventional methods of blood parameter determination [16]. For example, a conventional technique to measure the total serum bilirubin (TSB) is determined from a blood sample, obtained in an invasive way. Although the method is approved for monitoring jaundice but has several drawbacks. Invasive blood sampling is painful and stressful for the neonates, resulting in blood loss and an increased risk of osteomyelitis and infection at the site of sampling. However, recent advances have shown great potential in deriving multiple blood parameters including bilirubin by the incidence of white light and application of absorption spectrometry. Similarly, fluorescence and Raman spectroscopy have also shown great potential in probing various parameters involving biological samples. Optical Emission Spectroscopy (OES) is another useful tool often used to understand the composition of various elements with short and longer life cycles. For example, understanding the components of Non-Thermal Atmospheric Plasma

is a matter of active research. However, OES provides an easy and deeper probing ability into the complex molecular interactions happening inside the plasma shower. With the advancement of CCD-based spectrograph, these experiments and their respective analysis have become cost-effective, easy to perform yet accurate.

1.3. Scope and Objective:

The development of cost-effective design and realization of highly sensitive spectroscopy-based instruments for potential applications in environmental monitoring and medical diagnosis is the key objective of the works under the thesis. Following are the representative examples of the proposed achievements towards the said objective. Fourier transform spectroscopy is a well-known technique to diagnose and quantify the presence of pollutants in the earth's atmosphere. Such remote sensing techniques do not require personnel to be physically present at the location. Michelson's Interferometry has been successfully utilized for simultaneous measurement of multiple pollutants in the atmosphere. Nonetheless, the detailed study of the detection process is still fully not explored. The potential use of such kind of detection can have a good impact on the development of really novel, low-cost, and portable diagnostic tools. Thus, designing such sensors for effective monitoring of pollutants in the atmosphere with meteorological relevance is one of the main objectives of the proposed work. We have constructed a low-cost, sensitive, laser-based (Helium Neon) optical Fourier-transformed (multiplexed) spectrometer for the quantification of suspended particulates in the air [17]. Further improvement in the instrument design and its applicability to other areas is under development.

Inductively coupled plasma mass spectrometry and laser-induced breakdown spectroscopy are the most popular techniques for monitoring toxic gases in the environment.

These techniques suffer from multiple problems including portability and increasingly high cost. The manual error involved due to sample preparation and substantially non-in-situ measurement is a major defect of existing techniques. Quantification of residual gas using spark spectrometry can be a potential tool for in-situ, automated, and online measurement. Such a low-cost, portable tool is absent from the contemporary literature and thus is one of the major focus areas of this work. We have introduced several toxic smokes into a gas chamber containing our developed instrument. We have also investigated the capability of the instrument for online analysis of suspended particulate matter as well as various gaseous elements in the smokes. Dedicated software for the practical interface has also been developed. The apparatus has been successfully tested to monitor several toxic fumes including cigarette smoke and NO_x [18].

Non-thermal plasma is used in applications of cleaning the exhaust gases from various sources such as factories or automobiles [19]. It is not new a concept, but in spite of extensive research in the following area, the details of the interaction of gasses and the in-situ plasma are not understood well. It has been well realized that the area and its application are still unexplored there is ample scope for further research in this area. Exploration of the possibility of simultaneous detection and control of indoor and outdoor pollutants is another objective of our work. Non-thermal plasma and its biomedical use will also be investigated in our current work [20]. The utilization pathogenic capability of non-thermal plasma is also one of the objectives of our work.

From the spectrum of scattered light originating from a suspension of particles in a fluid or gas one, quantitative information about the motion of a fluid can be obtained. By measuring the spectrum of the photocurrent, the intensity fluctuation of the scattered light

which is collected by a sensitive photodetector, efficient modeling backed by experimental verification is one of the major focuses of our work. The same model can be utilized to probe the eye spectrum of the incident laser beam and can be a potential device to diagnose glaucoma in a non-invasive way.

1.4. Summary of the Work Done:

1.4.1. Design and Development of Spark Spectrometry-Based Toxic Gas Detector:

1.4.1.1. Spark Spectrometry of Toxic Smokes: Towards a Portable, Inexpensive and High-resolution Environment Monitoring Instrument [21]:

In this work, we present the design and construction of a low-cost portable spectroscopic instrument for monitoring air quality in various environmental conditions. Apart from the detection of oxygen, nitrogen, water vapor, the instrument was shown to monitor toxic fumes including cigarette smoke, NO_X, and reactive oxygen radicals. We have also developed software for the online monitoring of toxic fumes in the environment. The role of the presence of water vapour in the sensitivity of detection has also been explored. General use of the instrument for any gas detection in the environment has also been discussed. In this study, we also made a prototype for the low-cost automated detection of toxic fumes. The portability of the unit will facilitate its placement at potentially dangerous places unfit for a human presence like volcanic eruption sites and jungle fire. The setup is shown to identify the presence of toxic gasses and aerosols in the high voltage spark. The experiment has been repeated with the introduction of cigarette smoke from various brands in the gas chamber and the results are found to be absolutely repetitive. We have found that an emission doublet (767.67 nm and 769.90 nm) is unanimously present in all the man-made toxic gasses including fumes from firecrackers, mosquito repellant, and cigarettes. In order to make the

setup to be cost-effective, we have replaced the combination of the interference filter and CCD detector specifically sensitive at the K^+ doublet line. The center wavelength of the filter is chosen to be around 769 nm to accommodate the potassium doublet and reject all other light signals which may be the signature of different other constituents of the atmosphere. The designed setup is capable of monitoring NO_2 in the gas chamber. Emission peaks at the wavelength band from 400 to 600 nm reflecting the unambiguous presence of NO_2 are evident from the spectrum. The enhancement of the N(II) line compared to that in ambient air. It has to be noted that the presence of NO, when excited by the spark, will result in emission lines of N(I) which are characterized mostly by peaks in the band of 700 nm to 900 nm. Thus, the recorded spectrum is evident to be due to the presence of NO_2 only. We have also tested our setup for the detection of extremely reactive atomic oxygen radicals. The tentative cost of the prototype for the detection of cigarettes is tentatively 100 USD including the filter. The long-term and short-term stability of the instrument are found to be reasonably good.

1.4.2. Detection of Heavy Metal Ions in Water Using Nanoparticle-Based Turn On Scattering Mechanism:

1.4.2.1. Nanoparticle-Based 'Turn-On' Scattering and Post-Sample Fluorescence for Ultrasensitive Detection of Water Pollution in Wider Window [22]:

In this scientific developmental work, we have demonstrated that the 'turn-on' Rayleigh scattering relies on the specific interaction of functionalized Ag NPs (Surface Plasmon Resonance (SPR) at 420 nm) with several model water pollutants, including mercury, methylmercury, and lead. It can be an efficient alternative strategy for the development of NP-based sensors with enhanced sensitivity in detection with a wider detection window. The

decreasing SPR band of the sensor's NPs indicated the interaction of the sensor with the model pollutants, and high-resolution electron microscopy and enhanced Rayleigh scattering of 356 nm excitation light indicated the enlargement of the NPs due to agglomeration. The post sample High Pass (HP) filter offers significant fluorescence upon receiving scattered light at 365 nm, which was shown to be useful for the detection of higher concentrations of pollutant in the test water. We have also using the above strategy to develop a prototype for the detection of model pollutants and demonstrated its efficacy. In this study, we have developed an optical technique combining Rayleigh scattering and post-sample fluorescence detection from colloidal Ag NPs having an SPR band at 420 nm. The spectra acquired from the developed device with various concentrations of model pollutants (Hg^{2+} ions in water) were observed. The post sample emission spectra with peaks at 395 nm (365 nm LED with 50 nm spectral width after 400 nm HP filter) and 520 nm (filter emission) was demonstrated. The intensity plots corresponding to various concentrations of Hg at 395 and 520 nm, respectively. The sensitivity of the developed sensor is exceptionally high because the Rayleigh scattering depends on the sixth power of the particle size. The Ag NPs were seen to increase in size with increasing concentration of the metal ions, in the presence of toxic metal ions. Therefore, the sensitivity of our device is very high. The efficacy of the technique is tested for the detection of several toxic ions including mercury, lead, and methylmercury in aqueous media. We have also monitored the concentrations of lead and methylmercury and validated the efficacy of the novel strategy for these pollutants. We developed a user-friendly LabVIEW-based Graphical User Interface (GUI) for data acquisition and real-time analysis of the results. The software acquires data sequentially by turning on the LED light, setting the spectrograph parameters, including the wavelength range, integration time, and

acquisition interval, and analyzing the data. Initially, the software checks the health of various components of the instrument. Subsequently, it turns on the blue LED and initializes the data acquisition; it displays a graph on the computer screen and stores all desired parameters as American Standard Code for Information Interchange (ASCII) files at the desired location.

1.4.3. Study of Non-Thermal Atmospheric Plasma on Biological Targets:

1.4.3.1. Non-Thermal Atmospheric Plasma (NTAP) induced cellular Envelope damage of *Staphylococcus aureus* and *Candida albicans* Biofilms: Spectroscopic and Biochemical Investigations [23]:

In this work, ambient air non-thermal plasma was generated using 15 kV potential difference, and utilizing the principle of Dielectric Barrier Discharge (DBD) and the effect of the generated plasma on *S. aureus* and *C. albicans* biofilm was observed. The possibility of using various flexible materials e.g., the liquid electrode was investigated and found to be effective in the successful generation of NTAP. The use of ambient atmospheric air for the production of NTAP has also been designed. Atomic emission spectroscopy was utilized to evaluate the components of the generated NTAP and its mechanism of action was carefully investigated. It was found that the generated plasma was effective in the disadherence of *S. aureus* biofilm from the titanium plate. Water was used as an electrode and glass acted as the dielectric barrier. The effect of NTAP was also investigated on *C. albicans* biofilm and the inactivation process was studied. The formation of new peaks in Nuclear Magnetic Resonance (NMR) spectra was observed confirming the compensation of the integrity of cells. This was further established from Scanning Electron Microscope (SEM) images of bacteria and fungi which show cell death occurs after the application of NTAP. The presence

of Reactive Oxygen & Nitrogen Species (RONS) in the non-thermal plasma is known to be the anti-microbial agent and hence can be an effective tool for the design of a low-cost-sterilizer under low resource setting. The potential of the setup and the ease of installation was utilized to design and develop a wall-mounted instrument capable of generating NTAP for potential use in hand sanitization in the non-invasive and non-contact method without the application of any chemical. The set-up is extremely cost-effective and easy to use. We believe this set-up will be a cheap alternative to the conventional method of disinfection from *S. aureus* and *C. albicans* and can be used in public places e.g., hospital environments for hand and hospital tool sterilization. The setup for NTAP production was done using a glass di-electric barrier, 15 kV Neon Sign Transformer from Canon, India, and a high voltage copper electrode. A glass test-tube manufactured by Borosil, India was used as a dielectric barrier and ambient atmospheric air acted as the dielectric barrier. In order to incorporate uniform plasma density in the application, we have used water in the test tube. Water from a reliable source with a resistivity value of 1200Ω at 20°C was used as one of the electrodes. The uniform surface coverage of the tip of the test-tube by water makes the DBD discharge to be uniform. The use of water inside test-tube made of flexible dielectric materials would expectedly offer flexibility in various biomedical applications. The Spectroscopic analysis of the generated NTAP was performed using HR4000 (Ocean Optics, Florida, USA) and SpectraSuite software. We investigated the effect of NTAP on biofilm growth of *S. aureus* on a titanium plate prepared in the laboratory. Biofilm is a microbial community encapsulated within a matrix which consists of an intensive network of cells that are attached to abiotic surfaces. Biofilm formed by *S. aureus* was considered for NTAP treatment after 48 Hrs of incubation. The titanium plate was treated with NTAP for five minutes and then

Crystal Violet (CV) staining was used for the quantitative assay of the total adhered biomass of *S. aureus* biofilm in the control and the NTAP treated titanium plates. The plasma-treated titanium plates showed no marked staining with CV whereas in the control or untreated titanium plate presence of CV stain was visually evident. Spectroscopic analysis of the solubilized CV (using 95% alcohol) was monitored by the absorbance at 595 nm. To understand the effect of NTAP treatment on fungal cells, Candida albicans was used as a model system as it is well known for its deadly infections in immunocompromised patients. NMR spectroscopy is a powerful technique to probe small chemical changes in a system at an atomistic resolution. Solution state live-cell NMR analysis provided insight into the morphological changes of the microbial cells before and after the treatment of NTAP.

1.4.4. Development of A Non-Contact Optical Spectroscopy-Based Device for Oral Cancer Detection:

1.4.4.1. Spectroscopic Studies on the Biomolecular Recognition of Toluidine Blue: Key Information Towards Development of a Non-Contact, Non-Invasive Device for Oral Cancer Detection [24]:

Molecular interaction of aromatic dyes with biological macromolecules are important for the development of minimally invasive disease diagnostic biotechnologies. In the present work, we have used Toluidine Blue (TB) as a model dye, which is a well-known staining agent for the diagnosis of oral cancer, and have studied the interaction of various biological macromolecules (protein and DNA) with the dye at different pH. Our spectroscopic studies confirm that TB interacts with Human Serum Albumin (HSA), a model protein at very high pH conditions which is very hard to achieve physiologically. On the other hand, TB significantly interacts with the DNA at physiological pH value (7.4). Our molecular studies strengthen the understanding of the TB staining of cancer cells, where the relative ratio of

the nucleic acids is higher than the normal intracellular content. We have also developed a non-invasive, non-contact spectroscopic technique to explore the possibility of quantitatively detecting oral cancer by exploiting the interaction of TB with DNA. We have also reported the development of a prototype named “Oral-O-Scope” for the detection of Oral cancer and have carried out human studies using the prototype.

In our work, we are interested in exploring the basic photochemistry behind the application mentioned above and simultaneously explore the possibility of quantitatively detecting oral cancer via spectroscopic methods exploiting the interaction of TB with DNA. In a recent study, it is shown that the absorption spectrum of TB can be fitted into different bands of six different aggregation species simultaneously present in the sample under investigation [25,26]. The overall TB spectrum may be mainly attributed to the H-type aggregation, although some of the species also show the J-type bands with distinct spectrum bands. The interest is to recheck the evidence of interaction between the dye and the macromolecules such as DNA and protein. Though it has already been reported in the literature with the stress that the dye must interact with the nucleic material of the virtue of its anionic and acidic nature [27], the strong confirmation of whether this dye interacts with protein at different pH is still unrevealed and this area will be focused in our work by exploiting the spectroscopic or absorption properties of the chosen model protein and the dye. The understanding of the pH-dependent interaction of TB will enable us to exploit its character in a direction where we can use it for oral cancer detection. We are also reporting the development of a prototype for malignant cell detection utilizing the fundamentals of reflection spectroscopy. The prototype has also been shown to be producing significantly accurate data when used in patients for preliminary clinical studies. The prototype has shown

the potential to successfully measure malignancy in a small number of human subjects. Although, extensive clinical trials need to be undertaken in future for the data to be statistically significant. We hope that toluidine blue staining method which was considered unreliable for its classical dependence on the experience of practitioner [28], would gain significant importance with its complementary use with Oral-O-Scope.

1.4.5. A Cost-Effective Method of Water Quality and Size Determination of Suspended Particulate Matter:

1.4.5.1. An Optical Scattering Based Cost-Effective Approach Towards Quantitative Assessment of Turbidity and Particle Size Estimation in Drinking Water Using Image Analysis [29]:

In the present work, we have used image analysis of a Red and a Blue dot on an optically lit cast screen across a model turbid medium to estimate the optical density (turbidity) and computational analysis of the captured image-edge blurring phenomena to conclude on the diameter of dominant suspended particulate matter in the turbid colloidal solution. We have also explored the possibility of using a submersible camera to acquire data for long term data acquisition of a natural water body. Data acquired remotely has been analyzed in our indigenously developed software for online monitoring. The proposed set-up finally produces real-time data of particle size estimation and fitness of consumption of contaminated water samples with sub-micron suspended particulate matter, which are difficult to assess via visual inspection. The system is effective in measuring bacterial growth and the acquired data have been compared with that of the growth curve obtained from the conventional method. The limit of detection (LOD) of the set-up was found to be 48 ppm. The extremely cost-effective nature of the set-up, the innovative method of analysis, and easy availability of components would expectedly make water quality assessment very easy

and user friendly. The developed set-up efficiently estimates the presence of suspended particulate matter including micro-organism to a level of 48 ppm (and hence defines the LOD of the system) which is well below the WHO level of 300 ppm in drinking water [30]. Water samples with coarser particles will be easier to identify and screen for consumption visually have not been included in this study.

1.5. Plan of Thesis:

The plan of the thesis is as follows

Chapter 1: This chapter discusses the different optical methodologies used in various biomedical and environmental applications. The future possibilities and spectra of the work and its relevance have also been discussed.

Chapter 2: This chapter focuses on the available instrumentation techniques relating to various forms of spectroscopy. The availability of such tools, their efficacy in areas relating to environmental and biomedical sensing has also been discussed.

Chapter 3: This chapter deals with instrumentation, data analysis techniques, and experimental procedures.

Chapter 4: This chapter describes the design and development of a Spark Spectrometry based portable, inexpensive and high-resolution environment monitoring instrument

Chapter 5: This chapter details the studies on a nanoparticle-based 'turn-on' scattering and post-sample fluorescence for detection of heavy metals in available water.

Chapter 6: This chapter describes the antimicrobial action of Non-thermal Plasma induced cellular cell damage.

Chapter 7: This chapter focuses on the Spectroscopic Studies on the Biomolecular Recognition of Toluidine Blue: Key and development of a non-contact, non-invasive device for oral cancer detection.

Chapter 8: This chapter details the development of an optical scattering based electro-optical strategy which is cost-effective and provides a quantitative assessment of turbidity and particle size estimation in drinking water using image analysis.

References

[1] C. Liu, S. Chen, X. Li, H. Xian, Performance evaluation of adaptive optics for atmospheric coherent laser communications, Opt. Express 22 (2014) 15554.

[2] M.W. Grenn, P. Perconti, J. Vizgaitis, J. Pellegrino, Medical infrared imaging, 2007, London, CRC Press .

[3] T.T. Wu, J.Y. Qu, Optical imaging for medical diagnosis based on active stereo vision and motion tracking, Opt. Express 15 (2007) 10421.

[4] E. Li Chan, The applications of Raman spectroscopy in food science, Trends Food Sci. Technol. 11 (1996) 361.

[5] R.O. Dubayah, J.B. Drake, Lidar remote sensing for forestry, J. For. 98 (2000) 44.

[6] G.D. Christian, Inorganic and analytical chemistra, Springer, 1972, Berlin, Springer

[7] A. Shahzad, G. Köhler, M. Knapp, E. Gaubitzer, M. Puchinger, M. Edetsberger, Emerging applications of fluorescence spectroscopy in medical microbiology field, J. Transl. Med. 7 (2009) 99.

[8] D. Müller, A. Ansmann, I. Mattis, M. Tesche, U. Wandinger, D. Althausen, G. Pisani, Aerosol-type-dependent lidar ratios observed with Raman lidar, J. Geophys. Res. Atmos. 112 (2007) 1.

[9] R.M. Gendreau, Spectroscopy in biomedical sciences, 2018, Florida, CRC Press.

[10] R.S. Harmon, F.C. DeLucia, C.E. McManus, N.J. McMillan, T.F. Jenkins, M.E. Walsh, A. Miziolek, Laser-induced breakdown spectroscopy-an emerging chemical sensor technology for real-time field-portable, geochemical, mineralogical, and environmental applications, Appl. Geochem. 21 (2006) 730.

[11] N. Castell, F.R. Dauge, P. Schneider, M. Vogt, U. Lerner, B. Fishbain, D. Broday, A. Bartonova, Can commercial low-cost sensor platforms contribute to air quality monitoring and exposure estimates?, Environ. Int. 99 (2017) 293.

[12] C.T. Nguyên, A. Galais, G. Fortunato, Pollution imagery by optical interferometry: Application to SO_2 gas, Appl. Opt. 34 (1995) 5398.

[13] P. Francis, M.R. Burton, C. Oppenheimer, Remote measurements of volcanic gas compositions by solar occultation spectroscopy, Nature 396 (1998) 567.

[14] M. Chin, P. Ginoux, S. Kinne, O. Torres, B.N. Holben, B.N. Duncan, R.V. Martin, J.A. Logan, A. Higurashi, T. Nakajima, Tropospheric aerosol optical thickness from the GOCART model and comparisons with satellite and sun photometer measurements, J. Atmos. Sci. 59 (2002) 461.

[15] M. Vojtisek-Lom, J.E. Allsop, Development of heavy-duty diesel portable, on-board mass exhaust emissions monitoring system with NO_x, CO_2 and qualitative pm capabilities, SAE Tech. Pap. 3641 (2001) 1.

[16] A. Halder, M. Banerjee, S. Singh, A. Adhikari, P K. Sarkar, A.M. Bhattacharya, P. Chakrabarti, D. Bhattacharyya, A.K. Mallick, S.K. Pal, A novel whole spectrum-based non-invasive screening device for neonatal hyperbilirubinemia, IEEE J. Biomed. Health Inform. 23 (2019) 2347.

[17] S. Singh, B. Saha, S.S. Sinha, S.K. Pal, Construction of a low-cost laser-based multiplexed spectrometer: a potential probe for environmental pollution monitoring, Int. J. Environ. Waste Manage. 9 (2012) 388.

[18] S. Singh, N. Polley, A. Mitra, S. Pal, Spark spectrometry of toxic smokes: Towards a portable, inexpensive, and high-resolution environment monitoring instrument, Clean Technol. Environ. Policy 16 (2014) 1703.

[19] Y. Xing, Z. Liu, R.A. Couttenye, W.S. Willis, S.L. Suib, P.T. Fanson, H. Hirata, M. Ibe, Processing of hydrocarbons in an AC discharge nonthermal plasma reactor: An approach to generate reducing agents for on-board automotive exhaust gas cleaning, J. Catalysis 253 (2008) 28.

[20] M. Golkowski, C. Golkowski, J. Leszczynski, S.R. Plimpton, P. Maslowski, A. Foltynowicz, J. Ye, B. McCollister, Hydrogen-peroxide-enhanced nonthermal plasma effluent for biomedical applications, IEEE Trans. Plasma Sci. 40 (2012) 1984.

[21] S. Singh, N. Polley, A. Mitra, S.K. Pal, Spark spectrometry of toxic smokes: Towards a portable, inexpensive, and high-resolution environment monitoring instrument, Clean Technol. Environ. Policy 16 (2014) 1703.

[22] S. Singh, A. Halder, O. Sinha, P.K. Sarkar, P. Singh, A. Banerjee, S.A. Ahmed, A. Alharbi, R.J. Obaid, S.K. Ghosh, Nanoparticle-based 'turn-on' scattering and post-sample fluorescence for ultrasensitive detection of water pollution in wider window, PloS One 15 (2020) e0227584.

[23] S. Singh, A. Halder, S.A. Mohid, D. Bagchi, O. Sinha, A. Banerjee, P.K. Sarkar, A. Bhunia, S.K. Ghosh, A. Mitra, Nonthermal atmospheric plasma-induced cellular envelope damage of *Staphylococcus aureus* and *Candida albicans* biofilms: Spectroscopic and biochemical investigations, IEEE Trans. Plasma Sci. 48 (2020) 2768.

[24] S. Singh, A. Halder, O. Sinha, N. Chakrabarty, T. Chatterjee, A. Adhikari, P. Singh, D. Shikha, R. Ghosh, A. Banerjee, Spectroscopic studies on the biomolecular recognition of toluidine blue: Key information towards development of a non-contact, non-invasive device for oral cancer detection, Front. Oncol. 10 (2020) 2293.

[25] R. Matassa, C. Sadun, L. D'Ilario, A. Martinelli, R. Caminiti, Supramolecular organization of toluidine blue dye in solid amorphous phases, J. Phys. Chem. B 111 (2007) 1994.

[26] L. D'Ilario, A. Martinelli, Toluidine blue: Aggregation properties and structural aspects, Model Simul. Mater. Sci. 14 (2006) 581.

[27] J. Wang, Y. Guo, B. Liu, C. Cheng, Z. Wang, G. Han, J. Gao, X. Zhang, Spectroscopic analyses on interaction of bovine serum albumin (BSA) with toluidine blue (TB) and its sonodynamic damage under ultrasonic irradiation, J. Lumin. 131 (2011) 231.

[28] M. Mascitti, G. Orsini, V. Tosco, R. Monterubbianesi, A. Balercia, A. Putignano, M. Procaccini, A. Santarelli, An overview on current non-invasive diagnostic devices in oral oncology, Front. Physiol. 9 (2018) 1510.

[29] S. Singh, A. Halder, A. Banerjee, M.N. Hasan, A. Bera, O. Sinha, S.K. Ghosh, A. Mitra, S. Pal, An optical scattering based cost-effective approach towards quantitative assessment of turbidity and particle size estimation in drinking water using image analysis, Eco. Evo. Rxiv. 1 (2020) 1.

[30] W.H. Organization, Silver in drinking-water: Background document for preparation of who guidelines for drinking-water quality. 2 (2003) 1.

Chapter 2

Overview of Spectroscopic Tools and Systems

The use of various optical spectroscopy-based tools to extract hidden information from environmental and biological targets is widespread. In this chapter, we will review few available spectroscopic techniques which provide better insight into various molecular level interactions enriching our knowledge in the above-mentioned fields.

2.1. Measurement and Analysis Tools:

2.1.1. Absorption Spectroscopy:

The Beer-Lambert law relates to the relative absorption of optical signals using an emitter detector pair whilst passing among a medium of certain pathlength and is presented numerically [1,2] as given in Eq. 2.1.

$$A = log_{10}(\frac{I_0}{I}) = \varepsilon lc \tag{2.1}$$

where A is the absorbance, I_o and I are the initial and final intensity of light, ε is the molar extinction coefficient of the solution under test with units $M^{-1}cm^{-1}$. The optical path length l and the concentration of the solution c are expressed in cm and molarity (M) respectively. Recent advances in spectrometer technologies including charge-coupled device (CCD) and complementary metal-oxide-semiconductor (CMOS) array have made detection technology easy to use, accurate, and cost-effective [3]. Such progress in the detector domain has made spectroscopy much popular than colour and image analysis. RGB analysis is one of the examples of image analysis which also has found many applications in the practical world [4]. Often air/water quality has been determined using airborne cameras and subsequent image analysis [5].

2.1.2. Diffuse Reflectance Spectroscopy:

Light incidence on biological targets and interacts with the skin and other targets and the retro-reflected beam carries meaningful information back to the receiver as shown in Figure 2.1. The UV and visible spectrum contribute in exciting electrons to the valence band and the spectrum receiver analyses the contribution of each wavelength. Optical scattering in biological targets in random trajectory, or diffusion, of incident photons, experiences multiple elastic scattering from cells, extracellular matrix, blood vessels, and other tissue components [6]. Optically scattered signals from the skin, brain tissues, and vessel walls have helped the development of new technologies and hence have attracted the attention of scientists all over the world [7].

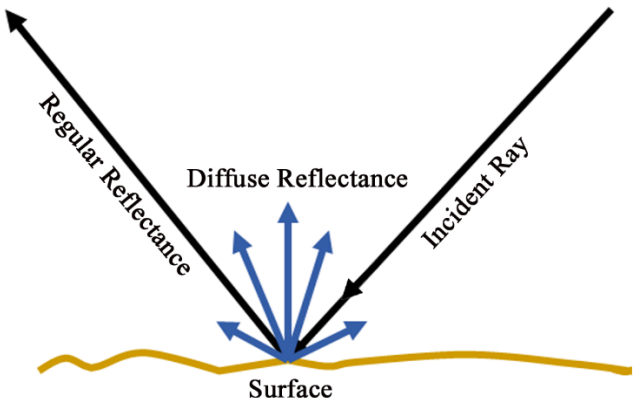

Figure 2.1: *Schematic representation of the diffuse reflection from a solid sample. The diffuse light can be collected for spectroscopic studies.*

Similarly, the optical scattering method finds interesting applications in the meteorological field. Optical propagation in aerosols may mathematically be predicted with acceptable precision by single-scattering methods. Nevertheless, multiple scattering effects need to be considered for denser targets like clouds [8]. Several optical instruments have been designed based on this principle. Lidar is a classic example of such an instrument.

The difference between specular spectroscopy and diffuse reflection spectroscopy [9] is, the former measures the direct change in the light intensity, whereas the latter measures the relative change in the amount of reflected light from a surface. Light scattering spectroscopy [10] is another form of reflectance spectroscopy. It determines the tissue structures by observing the intrinsic elastic scattering properties. The rate of the electrons jumping from the valence band to the conduction band due to optical excitation depends upon the absorbance of the light at a given bandgap (E_g) independent of the transmittance. In the diffuse reflectance spectroscopy, the Kubelka-Munk theory [11] determines from the diffused reflectance spectra. For an object under test, with a particle diameter that is comparable to the wavelength of incident light then diffuse reflectance no longer permits the secondary contributions of reflection, refraction, and diffraction, the absorption coefficient can be given by Eq. 2.2.

$$\frac{K}{S} = \frac{(1 - R_\infty)^2}{2R_\infty} \equiv F(R_\infty) \tag{2.2}$$

R_∞ is the diffuse reflectance and $F(R_\infty)$is the Kubelka-Munk function. The term K and S are the absorption coefficient and scattering coefficient respectively. The absorption coefficient becomes equal to twice of absorption coefficient (α) when the incident light scatters in a perfectly diffuse manner. In this case, considering the scattering coefficient as constant concerning wavelength, Kubelka-Munk theory is used to determine the E_g as shown in Eq. 2.3

$$[F(R_\infty)h\mu]^2 = C(h\mu - E_g) \tag{2.3}$$

Where μ is light frequency, h is Plank's constant, and C is the proportionality constant. This mode of optical detection finds relevance in remote sensing of unknown samples where the same cannot be put in the cuvette or point of care measurement is necessary.

2.1.3. Fluorescence Spectroscopy:

Fluorescence detection is a powerful and effective tool for the sensitive and selective monitoring of the physical and chemical performance of compounds under study [12]. The Jablonski diagram [13] offers a convenient representation of electrons in the ground state with the relevant transitions. The excitation procedure to the excited state (S_1) from the ground state (S_0) is very fast. After excitation, the fluorophore quickly relaxed from the singlet electronic state to an allowable vibrational level in the electronic ground state and fluorescence emission occurs. The fluorescence quantum yield (ϕ_f) gives the efficiency of the fluorescence process and is described by the ratio of photons emitted to photons absorbed. It can also be described by the radiative rate constant k_r, and the non-radiative rate constant k_{nr}, comprising all possible competing deactivation pathways, such as phosphorescence, intersystem crossing, internal conversion, etc. as given in Eq. 2.4.

$$\varphi_f = \frac{k_r}{(k_r + k_m)} \tag{2.4}$$

The fluorescence intensity I_f is given by the amount of light absorbed and the fluorescence quantum yield, ϕ as expressed in Eq. 2.5.

$$I_f = k\, I_0 \varphi [1 - 10^{-\epsilon bc}] \tag{2.5}$$

By simplifying the Eq. 2.5 can be rewritten as,

$$I_f = k\, I_0 \varphi [\epsilon bc] \tag{2.6}$$

where K is the proportionality constant attributed to the instrument, I_0 is the incident light intensity ε is the molar absorptivity, b is the path length, and c is the concentration of the substrate. This simplified relationship shows that fluorescence intensity is proportional to concentration.

2.1.4. Spark Optical Emission Spectroscopy:

Spark Optical Emission Spectroscopy is a very useful technique in materials processing because the plasma features can be correlated with the characteristics of the liquid samples and gas samples [14,15]. An electric arc or spark is passed through the sample, heating it to a high temperature to excite the atoms within it. The excited analyte atoms emit light at characteristic wavelengths that can be dispersed with a monochromator and detector [16].

2.1.5. Scanning Electron Microscopy:

One of the most extensively used for the investigation and analysis of microstructure, morphology, and chemical analysis is SEM [17]. A normal eye can resolve objects subtending about 1/60° visual angle which may be converted to -0.1 mm from a view distance of 25 cm. The discovery that electrons can be deflected by the magnetic in numerous experiments has been proved [18].

References

[1] D.F. Swinehart, The Beer-Lambert law, J. Chem. Educ. 39 (1962) 333.

[2] L. Kocsis, P. Herman, A. Eke, The modified Beer-Lambert law revisited, Phys. Med. Biol. 51 (2006) N91.

[3] T.S. Yeh, S.S. Tseng, A low cost LED based spectrometer, J. Chin. Chem. Soc. 53 (2006) 1067.

[4] Y.-C. Chang, J.F. Reid, RGB calibration for color image analysis in machine vision, IEEE Trans. Image Process. 5 (1996) 1414.

[5] L. Goddijn, M. White, Using a digital camera for water quality measurements in Galway Bay, Estuar. Coast. Shelf Sci. 66 (2006) 429.

[6] A. Moy, J. Tunnell, Diffuse reflectance spectroscopy and imaging, in imaging in dermatology, Imaging in Dermatology, 2016, Austin, Elsevier.

[7] V.V. Tuchin, Light scattering study of tissues, Phys. Uspekhi 40 (1997) 495.

[8] L.R. Bissonnette, P. Bruscaglioni, A. Ismaelli, G. Zaccanti, A. Cohen, Y. Benayahu, M. Kleiman, S. Egert, C. Flesia, P. Schwendimann, LIDAR multiple scattering from clouds, Appl. Phys. B 60 (1995) 355.

[9] B. van Ginneken, M. Stavridi, J.J. Koenderink, Diffuse and specular reflectance from rough surfaces, Appl. Opt. 37 (1998) 130.

[10] I. Georgakoudi, B.C. Jacobson, J. Van Dam, V. Backman, M.B. Wallace, M.G. Müller, Q. Zhang, K. Badizadegan, D. Sun, G.A. Thomas, Fluorescence, reflectance, and light-scattering spectroscopy for evaluating dysplasia in patients with Barrett's esophagus, Gastroenterology 120 (2001) 1620.

[11] W.E. Vargas, G.A. Niklasson, Applicability conditions of the Kubelka-Munk theory, Appl. Opt. 36 (1997) 5580.

[12] A. Shahzad, G. Köhler, M. Knapp, E. Gaubitzer, M. Puchinger, M. Edetsberger, Emerging applications of fluorescence spectroscopy in medical microbiology field, J. Transl. Med. 7 (2009) 99.

[13] D. Frackowiak, The jablonski diagram, J. Photoch. Photobio. B 2 (1988) 399.

[14] S. Singh, N. Polley, A. Mitra, S.K. Pal, Spark spectrometry of toxic smokes: Towards a portable, inexpensive, and high-resolution environment monitoring instrument, Clean Technol. Environ. Policy 16 (2014) 1703.

[15] A. Halder, S. Singh, A. Adhikari, S. Ghosh, D. Shikha, D. Saha, R. Chakraborty, A. Kundu, S.K. Tripathi, S.K. Pal, NaLiK, an self-developed device for rapid, reliable and simultaneous assessment of sodium, lithium and potassium for management of fluid balance and bipolar disorder in human subjects, J. Anal. At. Spectrom. 34 (2019) 1875.

[16] D. Ottesen, J. Wang, L. Radziemski, Real-time laser spark spectroscopy of particulates in combustion environments, Appl. Spectrosc. 43 (1989) 967.

[17] K. Vernon-Parry, Scanning electron microscopy: An introduction, III-Vs Review 13 (2000) 40.

[18] W. Zhou, R. Apkarian, Z.L. Wang, D. Joy, Fundamentals of scanning electron microscopy (SEM), Scanning Microscopy for Nanotechnology, 2006, New York, Springer.

Chapter 3

Instrumentation and Sample Preparation

This chapter focuses on the experimental and instrumentation details used during the thesis work. The testing, calibration, and validation of various biological and environmental samples were performed using developed instruments that were designed at certain times particularly for the development. However, calibration and validation were performed using conventional equipment available in various laboratories. In the following sections, the details of the experimental set-up from the instrumentation point of view have been discussed. The details of the sample preparation mechanism and sensor development details have also been discussed in detail.

3.1. Instrumental Set-up:

3.1.1. Steady-State Absorption and Fluorescence Spectroscopy:

A UV-Visible Spectrophotometer from Shimadzu, Japan (Model: UV-2450) was used to carry out all the absorption measurements on the probing samples. With a wavelength range between 190-900 nm, excellent performance, and a user-friendly interface, the instrument is a highly rated spectrophotometer [1,2]. For all the fluorescence measurements FluoroMax®-3 from HORIBA Jobin Yvon, Inc. Japan was used, which is a compact spectrofluorometer, offers the ultimate sensitivity in fluorescence investigations [3] have been used in the project for measuring the light emission from the probing molecules. The basic schematic diagrams of these two instruments have been shown in Figures 3.1 and 3.2 respectively.

For the studies on the development of a cost-effective sensor arrangement as well as low-cost detection set-up of spark spectroscopy-based system [4], a digital camera (QAWACHH) was used as the optical detector array [5,6].

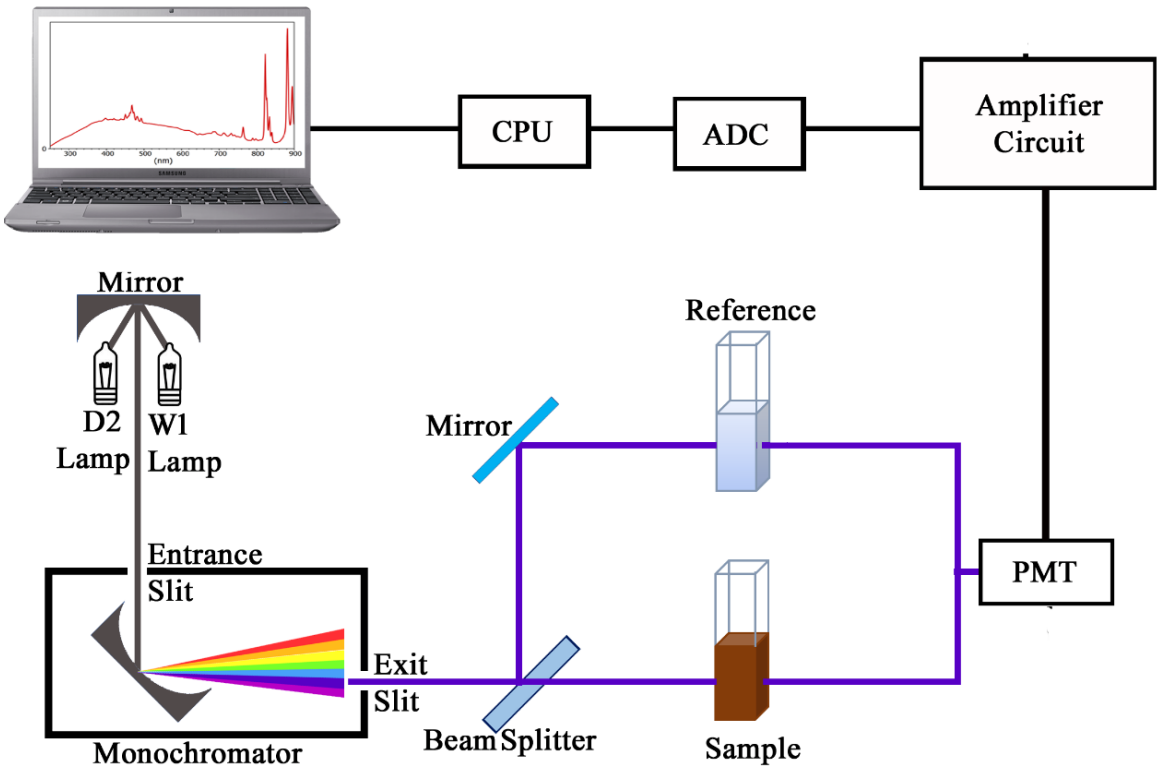

Figure 3.1: *Schematic diagram of a basic UV/Vis spectrophotometer. Here tungsten halogen lamp (W1) and deuterium lamps (D2) are used as light sources while PMT is the photomultiplier tube as detector. CPU and ADC indicate central processing unit, analog to digital converter and high-voltage amplifier circuit, respectively.*

All the Nuclear Magnetic Resonance (NMR) experiments were done at 298 K in a Bruker Advance III 500-MHz spectrometer using a 5-mm SmartProbe. A series of 1-D proton NMR spectra were obtained after each treatment by using "zgesgp" pulse program with 10% D_2O for locking the sample. The biological samples (*Candida albicans*) were analyzed using NMR equipment [7].

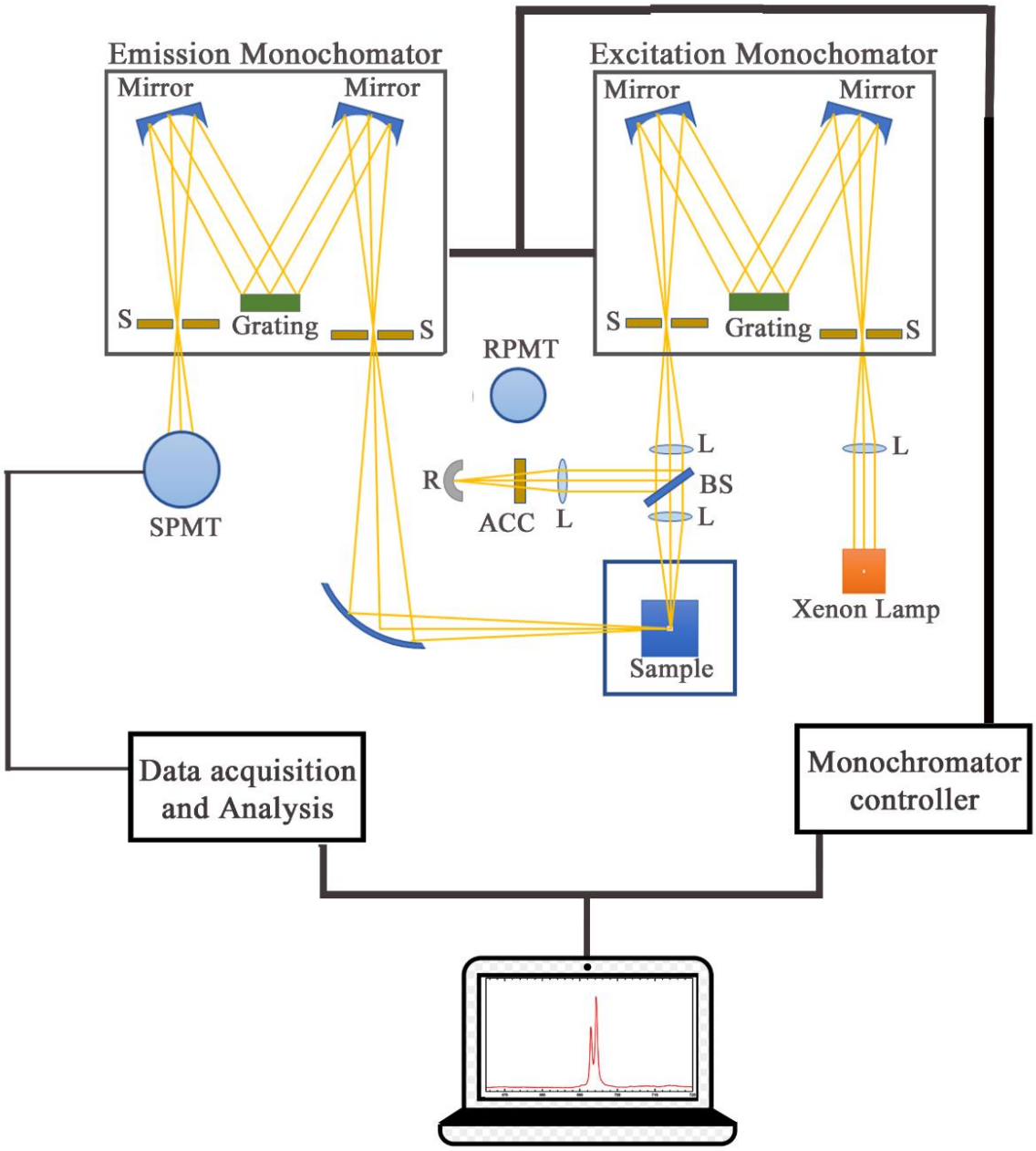

Figure 3.2: *Schematic diagram of a basic emission spectrofluorometer. L, S, BS, ACC, R, RPMT and SPMT represent lens, shutter, beam splitter, absorbance compensating cell, white reflector, reference photomultiplier tube and sample photomultiplier tube respectively.*

For the development of a non-invasive and non-contact device used in the detection of neonatal jaundice, STS-VIS Spectrometers (Figure 3.3) from Ocean Optics, USA was used. For detection of the electrolytes in the human body, a device has been developed using a

micro spectrometer (Model: C12880MA) manufactured by Hamamatsu, Japan, and the results have been validated with a conventional AU480 Chemistry Analyzer from Beckman Coulter, Inc. United States.

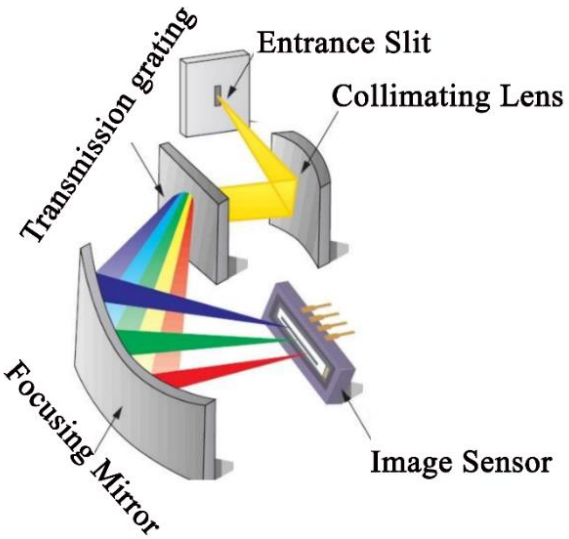

Figure 3.3: *Basic internal ray diagram of CCD array detector-based STS-VIS spectrographs.*

3.1.2. Dynamic Light Scattering (DLS):

DLS study is a proficient method for the determination of the particle size. For characterization of the developed nano-sensor to detect fluoride concentration in drinking water [8], commercially available Zetasizer Nano S from Malvern Panalytical, United Kingdom has been used. The instrument comes with a He-Ne laser of wavelength 633 nm with max 4 mW optical power. The Zetasizer Nano S provides the highest sensitivity for size diameter measurement ranging from 0.3 nm to 10 microns [9]. The basic schematic diagram of a DLS system [10] has been demonstrated in Figure 3.4. This instrument provides particle size distribution among liquid samples and provides reliable data in graphical and textual format. The hydrodynamic diameter measured with DLS is in good agreement with microscopy data.

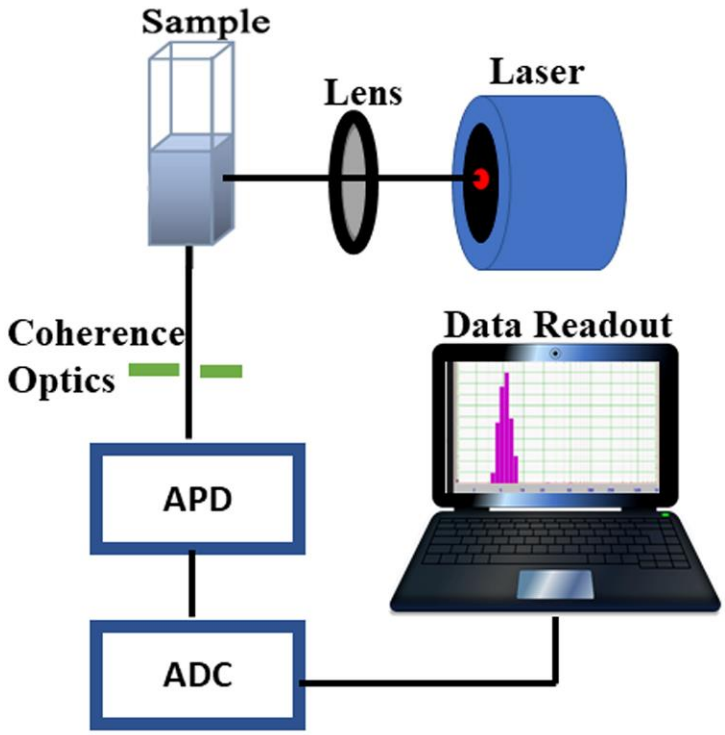

Figure 3.4: *Schematic ray diagram of a dynamic light scattering (DLS)*

3.1.3. Light Sources and Optical Components:

Light sources are the most important component for the development of an optical device. In the present work, both light-emitting diode (LED) of different wavelengths and tungsten-halogen have been used. Especially, for projects relating to oral cancer and other optical reflectometry studies, 3 W LED available from reliable sources was used to incident light on the cells under test and the subsequent acquisition was performed using fiber optic cable. An appropriate power supply was used to provide 5 volts to necessary sensors and components. The retro-reflected light after the incident on the cells was collected and fed to the receiver or spectrometer. A lab-grade diffuse reflectance probe (Ocean Optics, Florida) having six illumination fibres around one acquisition fiber was used to transmit the light from the LED source and to accept the diffuse optical signal from the sample and send the

signal to the spectrometer respectively. For another work, in the detection of heavy metals in available water, the measurement system consisted of three basic components: a 3 W LED of 365 nm wavelength (Ocean Optics, Florida, USA, a customized cuvette holder, and a Charged Couple Device (CCD)-based detector (Black-Comet, C-SR-200, StellarNet Inc., USA). The cuvette holder was designed in such a way that the detector and the LED remain orthogonal to each other. An optical filter (Ocean Optics, Florida, USA) with a passband > 400 nm was placed in front of the detector. In this setup, the light passing through the customized cuvette holder excites the sample and, after being scattered, was collected by the detector. A microcontroller (Arduino Uno) was used to control the LED through a solid-state relay. After passing through the sample, the UV scattered light reaches the filter, which emits a broadband fluorescence light spectrum. An HP filter (λ_{pass}> 400 nm) was used to split the excitation light beam and provide broad-spectrum fluorescence. The HP filter acts as a secondary detector as the scattered light saturates the receiver quickly [11].

3.2. Sample Preparation and Device Development:

In this section, the different sample preparation methods which are required for relevant device have been discussed.

3.2.1. Synthesis of Ag NPs:

A process including the reduction of $AgNO_3$ with $NaBH_4$ resulted in the synthesis of nitrate-capped Ag NPs at pH 6.5. Initially, a quick mixture containing stock solutions of 1 mM sodium citrate and 5 mM of both $NaBH_4$ and $AgNO_3$ in an aqueous solution was prepared. A stirrer was used for the smooth amalgamation of 16 mL of 1 mM solution in water and 1 mL aqueous $AgNO_3$ solution, maintained at a temperature of 0°C with a thermal

bath. Drops of instantly produced aqueous $NaBH_4$(150 mL of 5 mM) solution were added for 5 min. This solution was stirred for 2.5 Hrs. An absorption peak at 420 nm (SPR spectroscopic signature) from the X-ray absorption spectra confirmed the successful synthesis of the Ag NPs with the above-mentioned process.

For the oral cancer detection experiments Phosphate Buffer Saline (PBS, pH 7.4) was prepared by dissolving 0.13 M of NaCl, 2.7 mM of KCl, 1.4 mM of KH_2PO_4, 0.01 M of Na_2HPO_4 in 1-liter Millipore water. Glycine-Hydrochloric acid buffer (0.1M, pH 2) was prepared by dissolving 0.1 M of Glycine and 0.02 M HCl into water. Glycine-NaOH buffer (pH 11) was prepared by dissolving 0.01 M Glycine and 0.01 M NaOH in water. A stock concentration of 42 mM TB was prepared in distilled water. For absorption measurement, the stock solution of TB was diluted to 100X and 200X times for further use. Stock solutions of Human Serum Albumin (HSA) and DNA were prepared in 50 mM phosphate buffer of pH 7.4. A stock solution of TB in water was prepared daily for the spectroscopic measurements. To study the interaction of HSA with TB, HSA was used in the increasing ratio of 1:1, 1:10, 1:25, 1:50, and 1:100. To study the effect of pH in the interaction of TB and HSA, the latter was dissolved in buffers of different pH, keeping the concentration of TB constant [7].

3.2.2. Spectrometric Device for Detection of Oral Cancer (Oral-O-Scope):

Reflection spectrometry was used for the development of a device capable of non-invasive and non-contact development of oral cancer cells. This device consists of primarily a light source, a spectrograph, and a lab-grade reflectance probe. A 3 W LED light available in the local market was used to collect light and incident on the cells under test. An appropriate power supply was provided using a 5 Volt AC-DC adapter. The retro-reflected

light from the sample was collected and fed to a spectrograph purchased from Pure Engineering, USA. The optical signals after the successful acquisition were passed on to a computer via a microcontroller (Arduino Uno). An in-house designed software acquires the necessary information and produces the plot in real-time. A lab-grade diffuse reflectance probe (Ocean Optics, Florida) having six illumination fibers around one acquisition fiber was used to transmit the light from the LED source and to accept the diffuse optical signal from the sample and send the signal to the spectrometer respectively.

The clinical study was carried out in 20 patients after obtaining ethical clearance (ADCH/OP-513/16-11/906) issued by "The Ethical Committee", Awadh Dental College & Hospital, Jamshedpur, India. All methods in this study were carried out strictly following guidelines and regulations set by the ethical committee.

3.2.3. NTAP Generation:

The setup for Non-Thermal Atmospheric Plasma (NTAP) production was done using a glass dielectric barrier, a 15 kV neon sign transformer from Canon, and a high-voltage copper electrode. A glass test tube manufactured by Borosil as well as ambient atmospheric air. In order to incorporate uniform plasma density in the application, we used water in the test tube. Water from a reliable source with a resistivity value of 1200Ω at 20°C was used as one of the electrodes. The uniform surface coverage of the tip of the test tube by water makes the Dielectric Barrier Discharge (DBD) to be uniform. The use of water inside the test tube made of flexible dielectric materials would expectedly offer flexibility in various biomedical applications. The spectroscopic analysis of the generated NTAP was performed using HR4000 (Ocean Optics, FL, USA) and SpectraSuite software.

3.2.4. Development of Bacterial Biofilms:

Staphylococcus aureus strain was purchased from MTCC (MTCC3160). The bacterial culture in Luria broth having optical density OD_{600}~1 was spread on a 1-cm/1-cm cleaned titanium plate and incubated at 37°C for two days. Crystal Violet (CV, purchased from Sigma-Aldrich, India) [0.1%(w/v)] was used for performing the quantification process. Unattached cells were washed with 1 mL of water after being briefly aspirated. After 30 min of aspiration, CV solution (2 mL) was added to the titanium plates kept on a Petri dish. Titanium plates were washed with 1 mL of water, and 95% ethanol was used to solubilize the remaining CV. The absorbance at 595 nm (A595) was used for the evaluation of the degree of CV staining. The index of bacteria adherence to the titanium plates and formation of biofilm are calculated using the A595 values. Further, a UV-VIS spectrophotometer (Shimadzu UV-2600) was used to measure the extent of CV staining [12].

3.2.5. Scanning Electron Microscopy:

The *C. albicans* biofilms were prepared on sterile squared aluminum sheets as described above in the MTT assay and washed thrice with phosphate buffer solution (pH 7.4) to remove the planktonic cells. Next, the NTAP treatment was done following the same time points used in the flow cytometry assay, followed by fixing the cells with 2% glutaraldehyde. The samples were then washed thrice in PBS and dried by using 50, 80, and 100% ethanol gradation for 5 min each. The gold coating was done before SEM (ZEISS, Germany) data acquisition.

References

[1] C. Wan, Y. Yu, S. Zhou, W. Liu, S. Tian, S. Cao, Antioxidant activity and free radical-scavenging capacity of gynura divaricata leaf extracts at different temperatures, Pharmacog. Mag. 7 (2011) 40.

[2] W. Park, B.-c. Bae, K. Na, A highly tumor-specific light-triggerable drug carrier responds to hypoxic tumor conditions for effective tumor treatment, Biomaterials 77 (2016) 227.

[3] R.M. Cory, M.P. Miller, D.M. McKnight, J.J. Guerard, P.L. Miller, Effect of instrument-specific response on the analysis of fulvic acid fluorescence spectra, Limnol. Oceanogr. Methods 8 (2010) 67.

[4] A. Halder, P.K. Sarkar, P. Pal, S. Chakrabarti, P. Chakrabarti, D. Bhattacharyya, R. Chakraborty, S.K. Pal, Digital camera-based spectrometry for the development of point-of-care anemia detection on ultra-low volume whole blood sample, IEEE Sens. J. 17 (2017) 7149.

[5] S. Singh, N. Polley, A. Mitra, S.K. Pal, Spark spectrometry of toxic smokes: Towards a portable, inexpensive, and high-resolution environment monitoring instrument, Clean Technol. Envir. Policy 16 (2014) 1703.

[6] A. Halder, S. Singh, A. Adhikari, S. Ghosh, D. Shikha, D. Saha, R. Chakraborty, A. Kundu, S.K. Tripathi, S.K. Pal, NaLiK, an self-developed device for rapid, reliable and simultaneous assessment of sodium, lithium and potassium for management of fluid balance and bipolar disorder in human subjects, J. Anal. At. Spectrom. 34 (2019) 1875.

[7] S. Singh, A. Halder, O. Sinha, N. Chakrabarty, T. Chatterjee, A. Adhikari, P. Singh, D. Shikha, R. Ghosh, A. Banerjee, Spectroscopic studies on the biomolecular recognition of toluidine blue: Key information towards development of a non-contact, non-invasive device for oral cancer detection, Front. Oncol. 10 (2020) 2293.

[8] A. Halder, M. Banerjee, S. Singh, A. Adhikari, P.K. Sarkar, A.M. Bhattacharya, P. Chakrabarti, D. Bhattacharyya, A.K. Mallick, S.K. Pal, A novel whole spectrum-based non-invasive screening device for neonatal hyperbilirubinemia, IEEE J. Biomed. Health Inform. 23 (2019) 2347.

[9] L. Böhmert, M. Girod, U. Hansen, R. Maul, P. Knappe, B. Niemann, S.M. Weidner, A.F. Thünemann, A. Lampen, Analytically monitored digestion of silver nanoparticles and their toxicity on human intestinal cells, Nanotoxicology 8 (2014) 631.

[10] W. Jiahang, H. Zhenrong, M. Xinsheng, Y. Chengjun, Design and application of multi-function pick-up instrument DLS with high precision, Earthq. Eng. Eng. Vib. 6 (2005) 1.

[11] S. Singh, A. Halder, O. Sinha, P.K. Sarkar, P. Singh, A. Banerjee, S.A. Ahmed, A. Alharbi, R.J. Obaid, S.K. Ghosh, Nanoparticle-based 'turn-on'scattering and post-sample fluorescence for ultrasensitive detection of water pollution in wider window, PloS One 15 (2020) 1.

[12] S. Singh, A. Halder, S.A. Mohid, D. Bagchi, O. Sinha, A. Banerjee, P.K. Sarkar, A. Bhunia, S.K. Ghosh, A. Mitra, Nonthermal atmospheric plasma-induced cellular envelope damage of staphylococcus aureus and candida albicans biofilms: spectroscopic and biochemical investigations, IEEE T. Plasma Sc. 48 (2020) 2768.

Chapter 4

Spark Spectrometry of Toxic Smokes: Towards a Portable, Inexpensive, High-resolution Environment Monitoring Instrument

4.1. Introduction:

Multiple health conditions including respiratory tract infections, heart disease, and lung cancer have been attributed to breathing polluted air [1]. Apart from "smoking", the sources of air pollution causing a deadly influx of CO, SO_2, NO_2, Pb, do not need much introduction and a mammoth of information is already present in the contemporary literature. World-wide cigarette smoking is the leading cause of preventable death and a major public health concern [2]. Tobacco use leads most commonly to diseases affecting the heart and lungs. Smoking is a major risk factor for heart attacks, strokes, chronic obstructive pulmonary disease (COPD), emphysema, and cancer (namely lung cancer, cancers of the larynx and mouth, and pancreatic cancer). Some nontrivial sources of air pollution, however, very much intense in some of the countries are also becoming potential threat to the environment [3]. Particularly, in developing and underdeveloped countries, there are some nontrivial sources of air pollution including traditional biomass burning [4,5]. The most dangerous practice of cooking among lower-income group people by burning "garbage" containing various kinds of plastics is considered to be sources of lots of poisons in the air [6]. The smoke out of the garbage-burning commonly contains vapors and solid compounds suspended in the air called particulate matter. The toxic chemicals released during burning include nitrogen oxides, sulfur dioxide, volatile organic chemicals (VOCs), and polycyclic organic matter (POMs).

Burning plastic and treated wood also release heavy metals and toxic chemicals such as dioxin [7]. Smoke from wood and trash contains very small particles that can be breathed deep into the lungs. Once trapped in the lungs, these particles can cause cell damage [8]. Associations have been found between day-to-day particulate air pollution and increased risk of various adverse health outcomes, including cardiopulmonary mortality [9,10]. These alarming figures indicate the need for identification and constant monitoring of suspended particulates with special emphasis on toxic smoke present in ambient air [11]. There is some evidence that long-term exposure to NO_2 at concentrations above 40-100 $\mu g/m^3$ may decrease lung function and increase the risk of respiratory symptoms [12,13]. NO_x reacts with ammonia, moisture, and other compounds to form nitric acid vapor and related particles. Small particles can penetrate deeply into sensitive lung tissue and damage it, causing premature death in extreme cases. Inhalation of such particles may cause or worsen respiratory diseases, such as emphysema or bronchitis, or may also aggravate existing heart disease [14].

Inductively Coupled Plasma -Mass Spectrometry (ICP-MS) has by far been proven as the best technique for evaluation of constituents in a mixture [15-17]. In the conventional elemental analysis, samples of various types are usually prepared or digested and then introduced as solutions to the plasma by a nebulizer. However, sample digestion is a tedious, labor-intensive, and time-consuming process, and there is a risk of analyte loss and contamination that may occur during sample preparation [18]. Moreover, sample preparation involves the risk of human errors and thus repeatability of results may not be possible. For an ideal case, a sample should be analyzed in its natural form to overcome these drawbacks [16]. Recently, injection and testing of direct analyte particularly in gaseous form have been

reported [15]. Other disadvantages of ICP-MS include extremely high cost and non-portability of the instrument to the in-situ measurement site. The instrument is a benchtop model and requires a relatively clean environment to operate and sustain.

Laser-induced breakdown spectroscopy or (LIBS) can be an alternative to ICP-MS as the former technique has distinct advantages over the latter. The principal advantages of LIBS over ICP-MS include the simplicity of the technique, sampling speed, and most importantly less sample preparation. In particular, sample size, analysis time, and less sample manipulation provide a distinct advantage in this instrument. Another very important advantage is the suitability for remote and in-situ measurements and the instrument's adaptability for field portability [19,20]. LIBS, like any other technique, is not free from limitations. They include material specific laser sample interactions, difficulty in obtaining suitable standards, large interference effects, low sensitivity, and the possibility of ocular sample damage [21]. Once again, LIBS systems available commercially or indigenously developed in labs are remarkably costly and are not free from the shortcomings of low sensitivity and poor accuracy.

In this work, we design and construct low-cost and hand-held instruments for environmental pollution monitoring. The design utilizes the principles of spark optical emission spectroscopy. The light emitted by high voltage spark through the test sample is collected by collimating optics and is focused on the CMOS detector. The widely available extremely low-cost CMOS detector has been utilized to acquire data for online monitoring of the instrument. The presence of oxygen and nitrogen in the ambient environment has been detected by the instrument as a benchmark. We have detected the presence of potassium in the toxic fumes including cigarette smoke. Possibilities of efficient detection of other toxic

gases including NO_x have also been attempted. The effect of water vapor in the environment in the detection of toxic fumes has been explored in our studies. By monitoring the emission line at 777 nm, a very reactive oxygen radical resulting due to the high voltage discharge has been detected. We have also developed software in the MATLAB platform for the online analysis and trigger alarm for the toxic gases in various environments.

4.2. Materials and Methods:

4.2.1. Materials:

All the materials used in the prototype design have been purchased from reliable sources. To the extent of our knowledge and capacity, the materials used were of the highest purity but also keeping in mind the cost feasibility of the crude materials. A vacuum desiccator (8 Litre) from Tarson, India was used as a gas chamber for creating desired pressure levels of various analytes. A vacuum pump and pressure gauge were also used to suck the air out of the mentioned gas chamber and hence create a partial vacuum for pressure-dependent studies. Copper sparking electrodes of the highest purity, plano-convex lenses, optical mounts, High Voltage (HV) source, and cheap CMOS chip is from Rohini Astrophysics, India. To verify the OD of the gas chamber highly coherent laser (He-Ne 632.8 nm) and detector from Melles Griot were used to get an estimation of the optical density of the smoke in a gas chamber. Cigarettes from various brands were used to verify the results hence can be treated as a confirmation of the constituents of various cigarette smoke. Optical Filter (AVJ Optics, India) of 10 nm FWHM (centered at 768.5 nm) was used in front of the CMOS chip for the specific detection of the K^+ line. All chemicals used in this procedure are analytical grade with the highest purity were purchased from reputed brands. A spectrometer (HR4000) from Ocean Optics, USA, was used for the spectral analysis of the spark emission.

Efforts to identify NO_2 present in the atmosphere has been tried and successfully achieved. NO_2 was prepared using copper strips and allowing them to react with concentrated HNO_3. The chemical reaction is shown below.

$$4HNO_3 + Cu \rightarrow Cu(NO_3)_2 + 2NO_2 + 2H_2O \qquad (4.1)$$

4.2.2. Design:

The design of the optomechanical component setup including a ray diagram has been explained in Figure 4.1(a). The setup essentially consists of two copper electrodes connected to a high voltage supply typically at 15 kV. We have used a high voltage current limiting

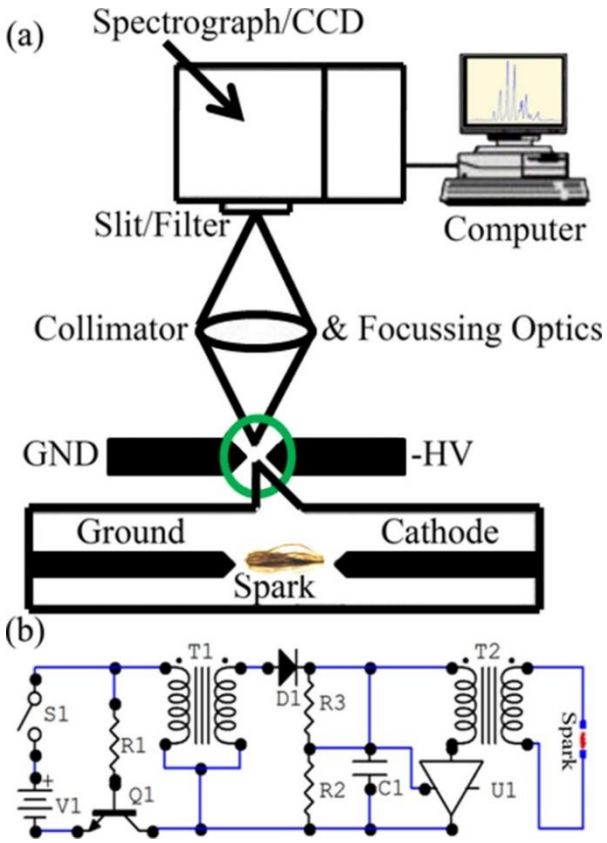

Figure 4.1: *(a) Schematic diagram of the designed setup. (b) Circuit diagram of the battery operated high-voltage power supply.*

transformer (typically used in powering neon sign) for the spark voltage supply. The electrodes when kept at a distance equal to the spark gap produce an electrical discharge in

the open air. The electrical discharges across the electrode knock off electrons of the residual gas to higher energy orbital and when these electrons return to their ground or stable orbital, they emit photons which are normally captured by a photosensitive device to provide spectral information. The electrodes are attached with a granite housing which is mounted over four long screws.

The light emitted by the spark set-up is collected by a pair of plano-convex lenses on each side of the electrodes. In another low-cost design, the electrodes and the optical detector are kept at the respective focus of the lenses. The high voltage current limiting transformer has been replaced by 1.5 volts (AA battery) operated sparker. The modification leads the set-up to be ultra-portable (handheld). The detailed circuit diagram of the sparker circuit is shown in Figure 4.1(b). The benchmark spectra obtained from both the set-ups show the difference in the emission lines (in the UV-VIS region) of nitrogen and oxygen due to the difference in the spark voltage and gap, however, consistent with the reported values of the emission lines [22,23]. We have also observed that emission lines for water vapour (Hα) and K^+ are independent of the set-up [24]. The entire setup as shown in Figure 4.2, except the computer can be placed inside the gas chamber for performing controlled pressure-dependent experiments.

4.2.3. Charge-Coupled Device (CCD) Detector:

The set-up is connected to a computer via a USB wire for real-time data monitoring and analysis. Commercially available CMOS array offers reasonably good Signal to Noise Ratio (SNR), reduce the cost as well as Radio Frequency Interference (RFI) free output signal. A computer program has been developed for online monitoring of the signal from the detector. An alarm sounding system has been designed to set off as soon as the signal value crosses a

certain threshold value. The data are also stored in a data file on the computer hard drive for future offline analysis.

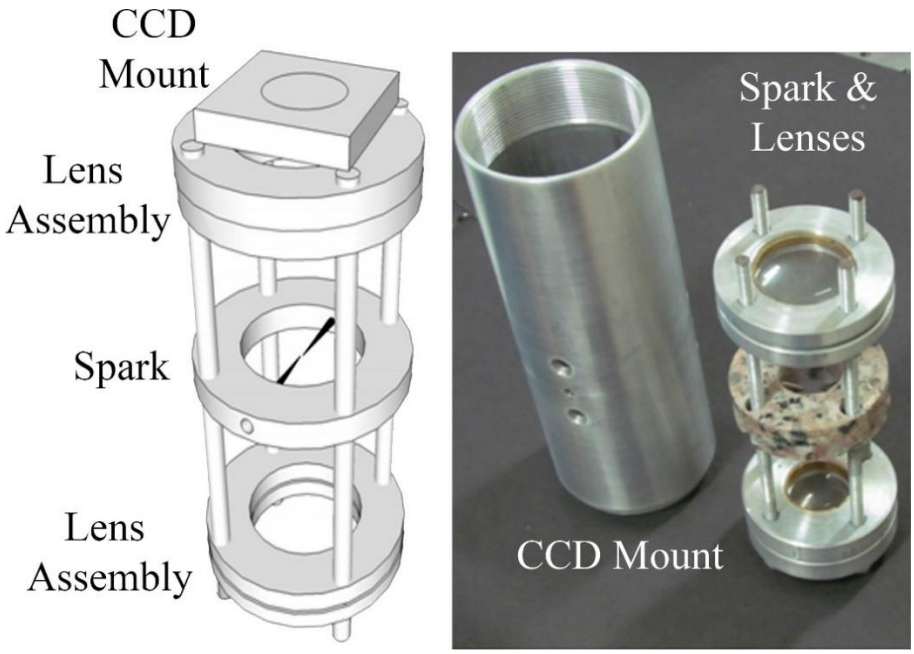

Figure 4.2: *Mechanical design of the design setup is shown in the left panel. Right panel shows photograph of the setup. Simplicity and portability can easily be evident from the picture.*

4.2.4. Software:

The programming code has been developed on the MATLAB platform. As shown in Figure 4.3, the flow chart clearly shows that the input signal is disintegrated into RGB

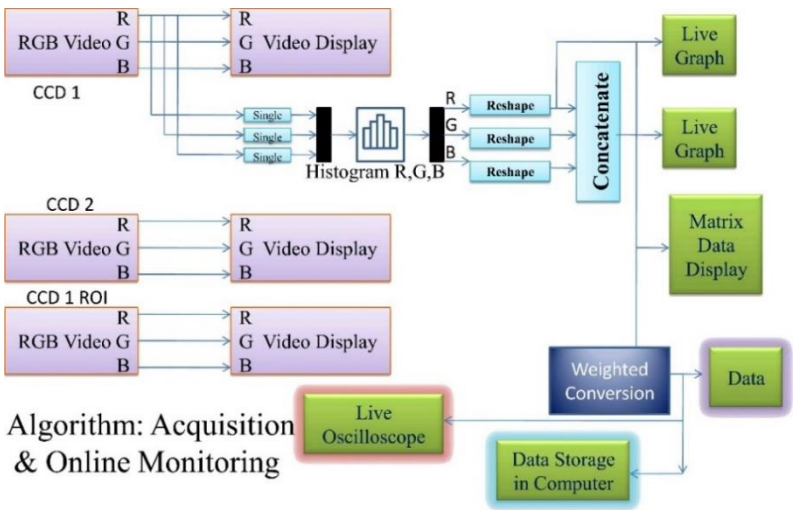

Figure 4.3*: Flow chart of the developed software in the MATLAB platform for the data acquisition and online monitoring/alarm sounding*

component values. Each matrix is separately plotted and the red components (characteristic of K^+ ion) are connected to a virtual scope for the display of current values. The matrix of values is converted to unique numbers considering the weight of each bit of the matrix. A threshold value has been provided in the software for alarm considering the toxicity of the gas and the sensitivity of the site under monitoring. For example, hospitals and schools are more likely to have very low threshold levels whereas other public places may have a higher tolerance.

4.3. Results and Discussion:

4.3.1 Test of the Instrument with Standard Samples for Benchmarking:

Figure 4.4 shows typical emission spectra of the spark in our instrument with various discharge voltages. As shown in Figure 4.4(a) the emission spectrum of air contains several characteristic emission lines of nitrogen (500.23 nm, 516.95 nm, 567.21 nm, 592.98 nm) and oxygen (462.69 nm). A relative faint characteristic of Hα line (656.56 nm) [25], indicating the presence of water vapor in the ambient atmosphere is distinct from the spectrum. Upon insertion of water vapour to the experimental gas chamber (desiccator), enhancement of the Hα line is evident from Figure 4.4(b). It has to be noted that the emission spectrum of the spark discharge in the air very much depends on the DC voltage (HV, Figure 4.1), the spark gap, and the material used in the electrode [26]. The spectrum of the spark discharge in air at a DC voltage of 15 kV shows emission in the UV region. The characteristic emission lines of air are indicated in the spectrum Figure 4.4(c). The spectra of air as indicated in Figure 4.4(a) and Figure 4.4(c) are consistent with that of the reported literature in a similar

experimental condition, thus, can be considered as a benchmark of our experimental setup [27].

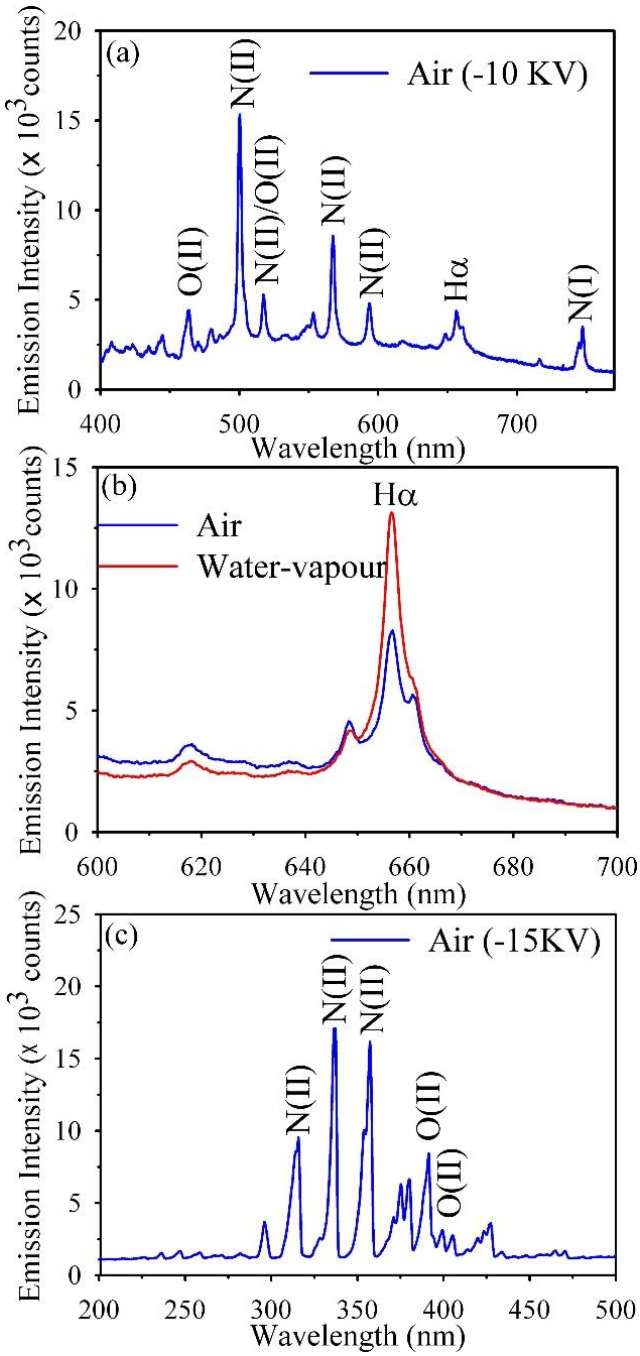

Figure 4.4: *Benchmark spectra of air and water vapour from the designed setup (see text for details).*

The set-up is shown to identify the presence of toxic gasses and aerosols in the high voltage spark. The experiment has been repeated with the introduction of cigarette smoke

from various brands in the gas chamber and the results are found to be repetitive. We have found that an emission doublet (767.67 nm and 769.90 nm) is unanimously present in all the man-made toxic gasses including fumes from firecrackers, mosquito repellant, and cigarettes. It is well known that Potassium Nitrate is one of the active ingredients of those products for their continuous burning [28]. Thus, our finding of K^+ emission is consistent with the fact and could be used as a marker of the toxic fumes. Figure 4.5 shows scanning and zoomed spectra in the presence and absence of cigarette smoke.

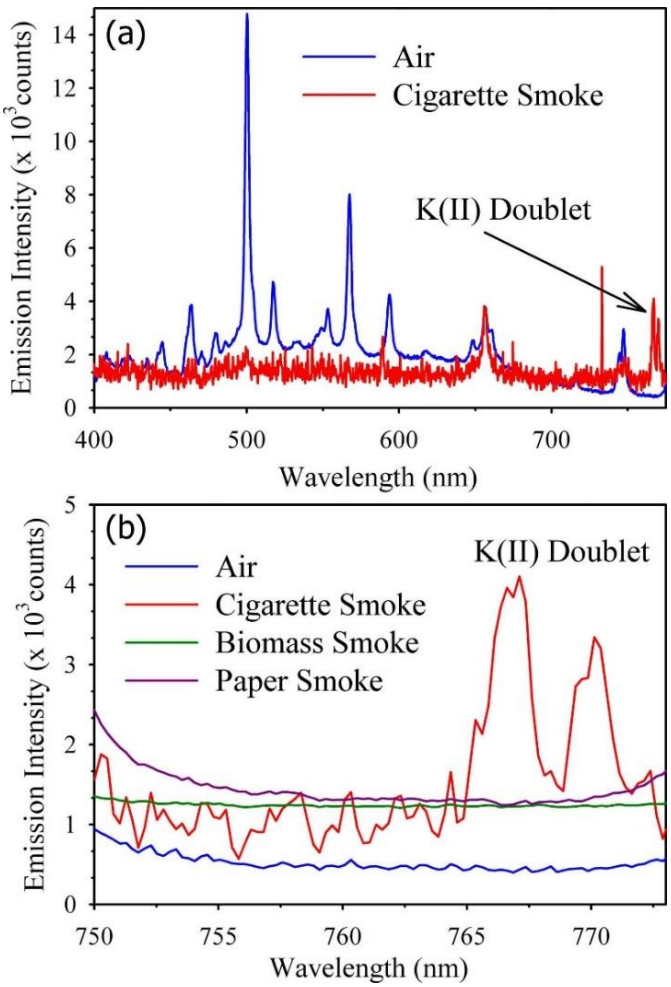

Figure 4.5: *Spectroscopic detection of K^+ ion emission as a distinct marker of cigarette smoke.*

The experiments were repeated with smoke from other non-polluting sources like burning paper, cow manure, etc. and the results compared with emission lines of indoor air. No K^+

spectroscopic lines are present in the spectrum other than the cigarette smoke. Cow manure is commonly used as burning material for cooking and other purposes, particularly in developing countries.

In order to make the set-up to be cost-effective, we have replaced the combination of the interference filter and CCD detector specifically sensitive at the K^+ doublet line. The center wavelength of the filter is chosen to be around 769 nm to accommodate the potassium doublet and reject all other light signals which may be the signature of different other constituents of the atmosphere. Figure 4.6(a) shows the passband of the filter along with the transmission efficiency in percentage. It is quite evident that the filter has a transmission efficiency of around 60% at a peak wavelength of 769 nm.

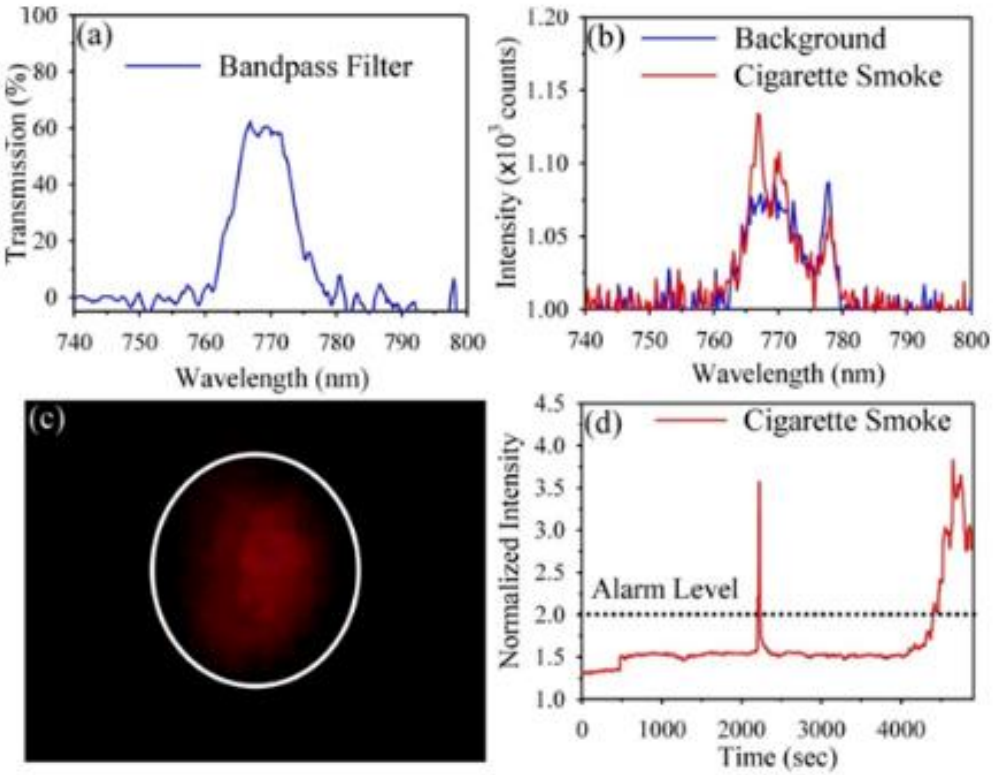

Figure 4.6: *(a) Transmission characteristics of the optical filter used as a replacement of the costly spectrograph. (b) Spectrum of the Cigarette smoke through the filter. (c) Signal acquired by computer through the filter-CCD combination in the place of spectrograph. (d) Test results of the low-cost version of the setup. The data acquisition and monitoring/alarm sounding is done through our developed software.*

The signal characteristics in presence of the filter are shown in Figure 4.6(b). The optical signal received from the setup suppresses all other wavelengths and allows the signal of K^+ ions' emission spectra to the spectrometer. The spectrometer was then removed and a CMOS chip was introduced to capture a live signal (red) from the spark in presence of cigarette smoke. As expected, the CMOS array recorded no signal for spark under ambient conditions in the absence of toxic smoke. However, with the introduction of cigarette smoke, and the signal was recorded on the computer screen. Figure 4.6(c) shows a screenshot of the live signals recorded during the acquisition. The region of interest has been marked with a circle. The developed software was programmed to set a threshold level as soon as the signal crosses a certain pre-fixed level (e.g. 2.0 here). The threshold level can be fixed according to the sensitivity of the place under test. As shown in Figure 4.7(a) the designed set-up is capable of monitoring NO_2 in the gas chamber. Emission peaks at the wavelength band from 400 to 600 nm reflecting the unambiguous presence of NO_2 are evident from the spectrum. The inset of Figure 4.8(a) shows the enhancement of the N(II) line compared to that in ambient air. It has to be noted that the presence of NO, when excited by the spark, will result in emission lines of N(I) which are characterized mostly by peaks in the band of 700 nm to 900 nm. Thus the recorded spectrum is evident to be due to the presence of NO_2 only [27]. We have also tested our set-up for the detection of extremely reactive atomic oxygen radicals. A recent study using atomic spectroscopy in the visible region shows that emission at 777 nm is a clear indication of the presence of the very reactive oxygen radicals [29]. The origin of the emission line at 777 nm is found to correspond to the oxygen atom transition O ($3p^5p \rightarrow 3s^5s$) as shown in Figure 4.7(b). The details of the species and their interaction with other organic molecules are described in the earlier literature. A simple modification as

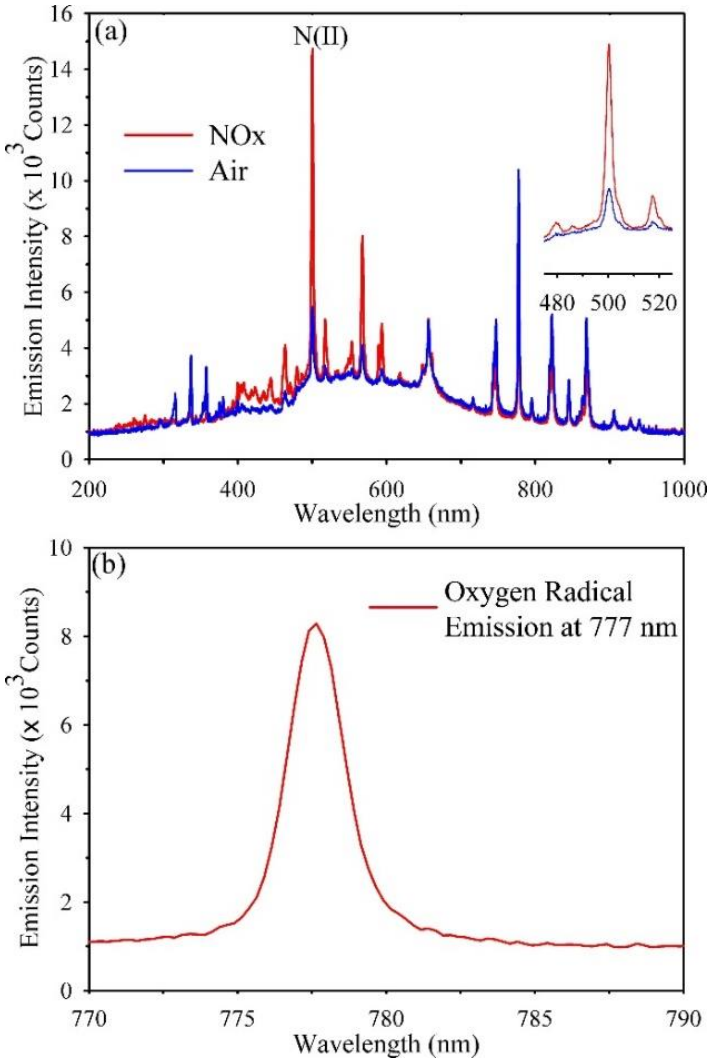

Figure 4.7: *Detection of toxic NOx (a) and highly reactive oxygen radical (b), using our setup.*

described earlier would be able to replace the costly spectrometer with the filter-CCD (centered at 777 nm) for the atomic oxygen detector.

In a practical application of the design setup, we intend to use the same in an open environment (not in a gas chamber). However, the presence of water vapour (humidity) with various proportions in an ambient open environment is unavoidable. Thus, in order to investigate the role of humidity in the detection sensitivity of toxic fumes, we have allowed controlled water vapour in the gas chamber during the spectroscopic detection of various emission lines of the fumes. As shown in Figure 4.8(a), we have observed a significant

enhancement of the K^+ emission line, reflecting higher smoke detection sensitivity in presence of water vapour.

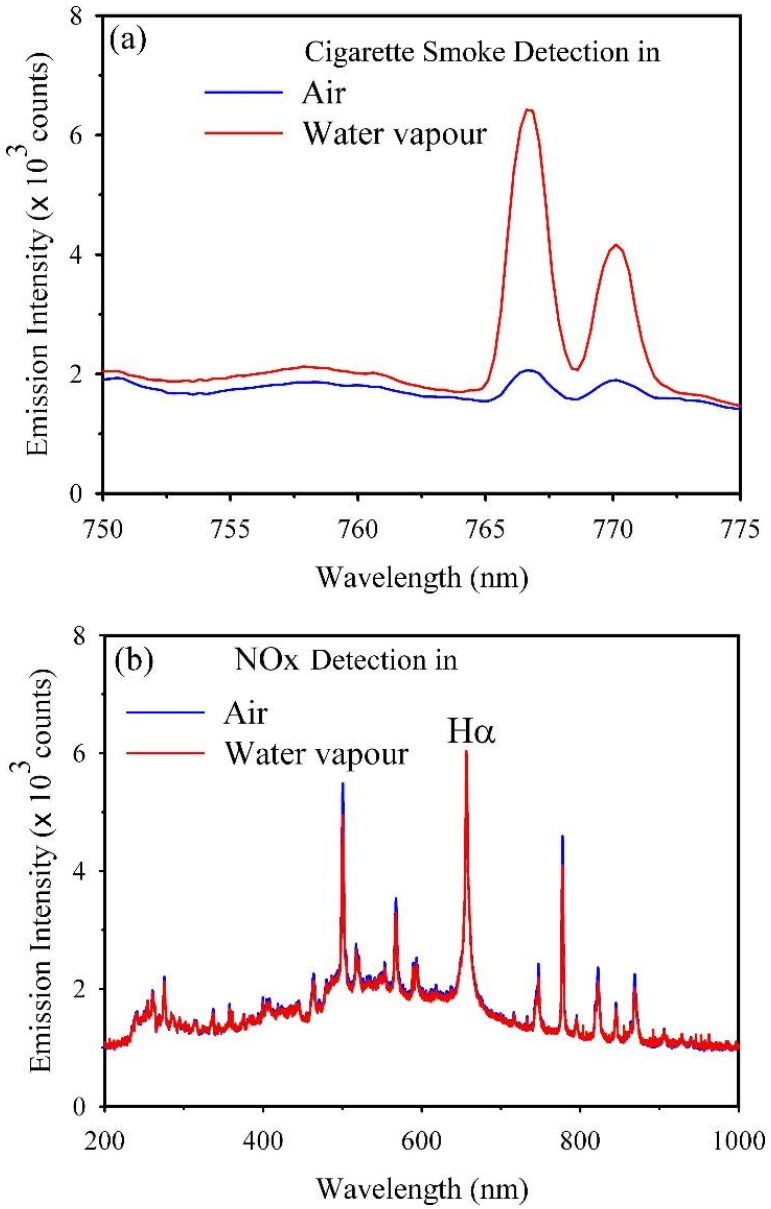

Figure 4.8: *Detection of cigarette smoke (a) and NO_2 in presence of water vapour (b). Enhancement of detection sensitivity in the case of cigarette smoke is clearly evident from panel (a).*

Thus, to calibrate the setup, one has to take care of the humidity in the environment under investigation. We have also observed an insignificant effect of the NO_x detection sensitivity in presence of water vapour as shown in Figure 4.8(b). It has to be noted that ingestion of both gases will have the same affinity towards water. Although, a detailed conclusion on

enhanced sensitivity of K^+ ion and NO_x lines invites further experimental and theoretical investigations. Some qualitative arguments may be made for the explanation of the observation. From the spectra Figure 4.8(b) the position of Hα line (due to water vapour) in comparison to the emission line under investigation is concluded to play a significant role. K^+ (at 767.67 nm) indicating the cigarette smoke, is lower in energy compared to that of the Hα line (656.56 nm). Thus K^+ ion duly solubilized in the water cluster can be excited without much interference from the host matrix (water cluster). On the other hand, the characteristic peak of N(II) (500.32 nm) is higher in energy as compared to that of Hα. Thus, the host water cluster is expected to absorb energy from the excitation source and hinder the excitation of the digested NO_2 in the water cluster. Ease of excitation of metal ions due to solvation of water cluster is reported in the literature [30]. Our Observation of enhanced detection of K+ line in presence of water vapour is consistent with the theoretical prediction [31]. The developed instrument was calibrated using OD data as shown in Figure 4.9.

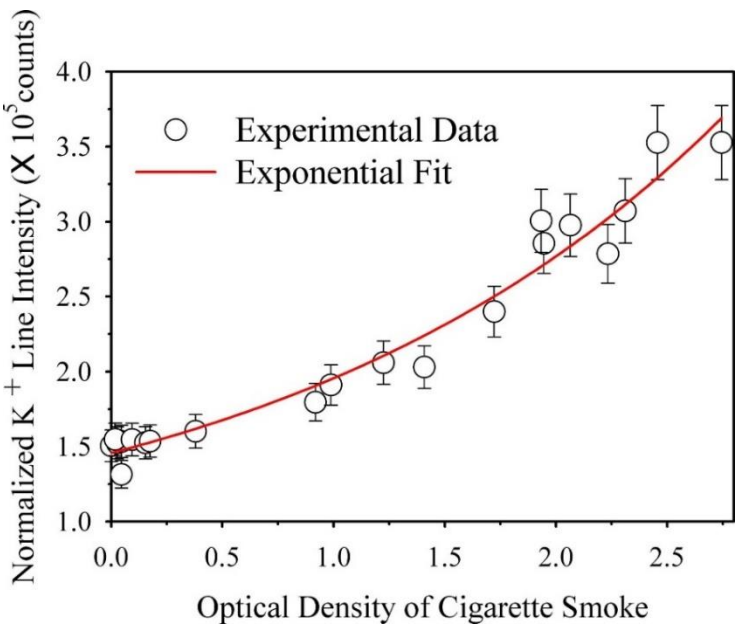

Figure 4.9: *Intensity of the K^+ emission line in the cigarette smoke as a function of optical density (OD) of the smoke in the gas chamber (open circles). The solid line is the exponential growth function fit to the experimental data points.*

4.4. Conclusion:

The design and construction of a low-cost portable spectroscopic instrument for monitoring air quality in various environmental conditions are presented. Apart from the detection of oxygen, nitrogen, water vapor, the instrument is shown to monitor toxic fumes including cigarette smoke, NO_X, and reactive oxygen radicals. We have also developed software for the online monitoring of toxic fumes in the environment. The role of the presence of water vapour in the sensitivity of detection has also been explored. General use of the instrument for any gas detection in the environment has also been discussed. In the present study, we have made a prototype for the low-cost automated detection of toxic fumes (from cigarette smoke) using the K^+ emission lines at 767.67 nm. We have also calibrated the prototype concerning optical densities at 632.8 nm (He-Ne laser), of the cigarette smoke in a designed gas chamber. In principle, our methods can be modified to design low-cost automated gas detection systems for any toxic fumes including NO_x, SO_2, O_3 by calibrating the system at 400-600 nm, 7.28 μm & 7.35 μm and near 350 nm respectively. The instrument can be a cheap alternative for costly methods of detection of indoor air pollution (e.g. cigarette smoking) as well as for outdoor air quality management studies. The portability of the unit facilitates its placement at potentially dangerous places unfit for a human presence like volcanic eruption sites and jungle fire. The tentative cost of the prototype for the detection of cigarette and other polluting smoke is tentatively 100 USD.

References

[1] J.E. Fielding, Smoking: Health effects and control, N. Engl. J. Med. 313 (1985) 555.

[2] P. Boyle, Cancer, cigarette smoking and premature death in Europe: A review including the recommendations of european cancer experts consensus meeting, Lung Cancer 17 (1997) 1.

[3] J. Cao, C. Yang, J. Li, R. Chen, B. Chen, D. Gu, H. Kan, Association between long-term exposure to outdoor air pollution and mortality in China: A cohort study, J. Hazard. Mater. 186 (2011) 1594.

[4] M.O. Andreae, P. Merlet, Emission of trace gases and aerosols from biomass burning. Global biogeochemical cycles, Global Biogeochem. Cycles 15 (2001) 955.

[5] M. Galanter, H. Levy, G.R. Carmichael, Impacts of biomass burning on tropospheric CO, NO_x, and O_3, J. Geophys. Res. Atmos. 105 (2000) 6633.

[6] C.R. Estrellan, F. Iino, Toxic emissions from open burning, Chemosphere 80 (2010) 193.

[7] N. Menad, B. Björkman, E.G. Allain, Combustion of plastics contained in electric and electronic scrap, Resour. Conserv.Recycl. 24 (1998) 65.

[8] J. Regalado, R. Pérez-Padilla, R. Sansores, J.I. Paramo Ramirez, M. Brauer, P. Paré, S. Vedal, The effect of biomass burning on respiratory symptoms and lung function in rural Mexican women, Am. J. Respir. Crit. Care Med. 174 (2006) 901.

[9] C.A. Pope Iii, R.T. Burnett, M.J. Thun, E.E. Calle, D. Krewski, K. Ito, G.D. Thurston, Lung cancer, cardiopulmonary mortality, and long-term exposure to fine particulate air pollution, JAMA 287 (2002) 1132.

[10] C.A. Pope III, R.T. Burnett, G.D. Thurston, M.J. Thun, E.E. Calle, D. Krewski, J.J. Godleski, Cardiovascular mortality and long-term exposure to particulate air pollution: Epidemiological evidence of general pathophysiological pathways of disease, Circulation 109 (2004) 71.

[11] F. Duan, X. Liu, T. Yu, H. Cachier, Identification and estimate of biomass burning contribution to the urban aerosol organic carbon concentrations in Beijing, Atmos. Environ. 38 (2004) 1275.

[12] W.H. Organization, Health aspects of air pollution with particulate matter, ozone and nitrogen dioxide, 3 (2003) 1.

[13] M. Kampa, E. Castanas, Human health effects of air pollution, Environ. Pollut. 151 (2008) 362.

[14] D.B. Menzel, The role of free radicals in the toxicity of air pollutants (nitrogen oxides and ozone), Free Radic. Biol. 2 (2012) 181.

[15] M.J. Chang, J.D. Naworal, K. Walker, C.T. Connell, Investigations on the direct introduction of cigarette smoke for trace elements analysis by inductively coupled plasma mass spectrometry, Spectrochim. Acta Part B: At. Spectrosc. 58 (2003) 1979.

[16] G. Jenner, H. Longerich, S. Jackson, B. Fryer, ICP-MS-A powerful tool for high-precision trace-element analysis in Earth sciences: Evidence from analysis of selected USGS reference samples, Chem. Geol. 83 (1990) 133.

[17] D. Ionov, L. Savoyant, C. Dupuy, Application of the ICP-MS technique to trace element analysis of peridotites and their minerals, Geostan. Newslet. 16 (1992) 311.

[18] G. Álvarez-Llamas, M.a. del Rosario Fernández de laCampa, A. Sanz-Medel, ICP-MS for specific detection in capillary electrophoresis, TrAC Trends Analyt. Chem. 24 (2005) 28.

[19] Y.-I. Lee, J. Sneddon, Recent developments in laser-induced breakdown spectrometry, ISIJ Int. 42 (2002) S129.

[20] K. Song, Y.-I. Lee, J. Sneddon, Recent developments in instrumentation for laser induced breakdown spectroscopy, Appl. Spectrosc. Rev. 37 (2002) 89.

[21] W.T.Y. Mohamed, Improved LIBS limit of detection of Be, Mg, Si, Mn, Fe and Cu in aluminum alloy samples using a portable Echelle spectrometer with ICCD camera, Opt. Laser Technol. 40 (2008) 30.

[22] J. Kuffel, P. Kuffel, High voltage engineering fundamentals, 2000, Woburn, Elsevier.

[23] K. Kasuya, H. Okayama, M. Watanabe, New method for thin-film formation with cryogenic diode and cryogenic target., Fusion Eng. Des. 44 (1999) 327.

[24] A. Vodacek, R. Kremens, A. Fordham, S. VanGorden, D. Luisi, J. Schott, D. Latham, Remote optical detection of biomass burning using a potassium emission signature, Int. J. Remote Sens. 23 (2002) 2721.

[25] M.R. Leahy-Hoppa, J. Miragliotta, R. Osiander, J. Burnett, Y. Dikmelik, C. McEnnis, J.B. Spicer, Ultrafast laser-based spectroscopy and sensing: Applications in LIBS, CARS, and THz spectroscopy, Sensors 10 (2010) 4342.

[26] W. Frey, M. Sack, R. Wuestner, G. Mueller, Gas-insulated self-breakdown spark gaps: Aspects on low-scattering and long-lifetime switching, Acta Physica. Polonica. A 115 (2009) 1016.

[27] Y. Ralchenko, A. Kramida, J. Reader, NIST atom. spec. database 8 (2008) 96.

[28] S.G. Wannamethee, A.F. Lever, A.G. Shaper, P.H. Whincup, Serum potassium, cigarette smoking, and mortality in middle-aged men, Am. J. Epidemiol. 145 (1997) 598.

[29] N. Krstulović, I. Labazan, S. Milošević, U. Cvelbar, A. Vesel, M. Mozetič, Optical emission spectroscopy characterization of oxygen plasma during treatment of a PET foil, J. Phys. D: Appl. Phys. 39 (2006) 3799.

[30] L. Partanen, M.-H. Mikkelä, M. Huttula, M. Tchaplyguine, C. Zhang, T. Andersson, O. Björneholm, Solvation at nanoscale: Alkali-halides in water clusters, J. Chem. Phys. 138 (2013) 44301.

[31] C. Zhang, T. Andersson, S. Svensson, O. Björneholm, M. Huttula, M.-H. Mikkelä, M. Tchaplyguine, G. Öhrwall, Ionic bonding in free nanoscale NaCl clusters as seen by photoelectron spectroscop, J. Chem. Phys. 134 (2011) 124507.

Chapter 5

Nanoparticle-based 'Turn-on' Scattering and Post-sample Fluorescence for Ultrasensitive Detection of Water Pollution in Wider Experimental Window

5.1. Introduction:

Heavy metal ion pollution is a severe problem threatening the environment, human health, and ecosystem balance [1]. Some of the most hazardous and ubiquitous pollutants that threaten the integrity of the ecosystem and have a deleterious effect on the health of humans and future generations are Mercury(II) (Hg^{2+}) and its organic form (i.e. methylmercury) [2] and Lead(II) (Pb^{2+}) [1,3]. Hg^{2+} can easily permeate through biological membranes and the blood-brain barrier and can damage DNA, impair cell division, and cause neurological damage [1,4,5]. The more potent form of Hg^{2+} is its organic form, i.e. methylmercury [6]. Thousands of individuals were affected by the Minamata disaster in Japan, one of the first large-scale accidents of methylmercury poisoning, and several other such accidents in other parts of the world affected many others [7]. Methylmercury has higher potency due to its high lipid solubility, which aids it in bio-accumulation and bio-amplification using the food chain of the ecosystem [8]. Mercury and methylmercury are dangerous neurotoxins, which are particularly hazardous for infants and pregnant women [9,10].

Although the Minamata accident raised global concern regarding the detrimental effects of mercury, the ill-effects of heavy metals, including mercury, were known to mankind

previously. Mercury is categorized as a neuro-toxicant, powerful, and dangerous to fetuses and children because it has the ability to pass through the placenta [11]. Even decades after the industrial dumping, survivors of mercury-pollution accidents still suffer from acute intoxication and its consequences [7]. The high toxicity of mercury and other heavy metal ions, even in trace amounts, calls for a very specific and highly sensitive determination. Sensitive detection of Mercury will lead to more effective toxicological, environmental, and biological monitoring.

The established techniques for monitoring and determining the Hg^{2+} concentration in environmental samples include atomic absorption/emission spectroscopy, X-ray absorption spectroscopy, inductively coupled plasma mass spectrometry (ICPMS), and surface-enhanced Raman scattering (SERS) [12-17]. However, these techniques require sophisticated and expensive instrumentation and are highly time-consuming. Recently, a variety of 'turn-on' spectroscopic methods have been reported and used; these include fluorescence and colorimetry, which are advantageous for analyzing complex biological samples and monitoring dynamic biological processes in living cells [18-23]. Great potential in the sensitive detection of Mercury is displayed by various fluorescent probes, such as semiconductor quantum dots and organic molecules [24-26]. However, the practical application of these fluorescent probes is hindered by their complex synthesis routes and the expensive and toxic reagents that are employed. The turbidity of the sample also interferes with the testing and determination of the concentration of heavy metal ions in the solution. Recently, few studies have been carried out using the wavelength and size-dependent 'Faraday-Tyndall' effect in gold nanoparticles (NPs) and the associated surface plasmon resonance (SPR) phenomena [27]. In a recent study, laser-induced microbubbles (LIMBs)

in gold colloid were reviewed, and their various properties including scattering and SPR were investigated in detail [28]. However, instances of heavy-ion detection in water are sparse in literature and few sensors have been developed based on the 'Faraday-Tyndall' effect.

Contemporary sensors of environmental pollutants can be classified into two categories: Higher sensitivity with a limited detection window and lower sensitivity with a wider detection window. Measurement strategies of real-world samples are often associated with complicated sample preparation in order to comply with the requirements of conventional sensors [29], which sometimes becomes cumbersome in a field-based measurement setting. It is preferable to have multiple parameters to monitor pollutants with higher sensitivity in wider measurement windows [30]. These can originate from different physical phenomena due to the interaction of the target pollutant with the sensor. Here, we developed a strategy of monitoring environmental water pollutants based on the enhanced Rayleigh scattering upon the interaction of the target pollutant with the NPs of the sensor and post sample fluorescence from a high-pass (HP) optical filter. Citrate-functionalized silver (Ag) NPs with an SPR band at 420 nm are used as a model sensor and the detection of a variety of water pollutants, including mercury ions, lead, and methylmercury is tested to justify the efficacy of the proposed strategy. Using our strategy, we also designed a cost-effective, user-friendly, and highly efficient device based on an optical technique, combining the principles of 'turn-on' Rayleigh scattering and post sample fluorescence from an optical filter in a wider detection window. Our device is shown to be useful for detecting heavy metal ions (mercury, methylmercury, and lead) with very high sensitivity in a wider detection window. We hope this device will a cost-effective alternative to conventional equipment.

5.2. Materials and Methods:

All chemicals used are of analytical grade. No further purification of the chemicals was performed. Ag nitrate ($AgNO_3$, 99.99%), sodium borohydride ($NaBH_4$), sodium citrate ($Na_3C_6H_5O_7$), and sodium hydroxide (NaOH) were purchased from Sigma-Aldrich. The samples were in the form of nitrate or chloride salts, which were used as received from Merck and Aldrich without further purification. A known amount of chloride or nitrate salts were used in the aqueous medium to prepare the stock solution (50 mM) of the metal ions. Millipore water (from Merck) was used as the aqueous solvent.

5.2.1. Synthesis of Ag NPs:

A process including the reduction of $AgNO_3$ with $NaBH_4$ resulted in the synthesis of nitrate-capped Ag NPs at pH 6.5. Initially, we prepared a quick mixture containing stock solutions of 1 mM sodium citrate and 5 mM of both $NaBH_4$ and $AgNO_3$ in an aqueous solution. A stirrer was used for the smooth amalgamation of 16 mL of 1 mM solution in water and an mL aliquot of $AgNO_3$ solution maintained at a temperature of 0°C with an ice bath. Drops of instantly produced aqueous $NaBH_4$ (150 mL of 5 mM) solution were added for 5 min. A distinct shift of the solution from colorless to intense yellow was observed. This solution was stirred for 2.5 Hrs. An absorption peak at 420 nm (SPR spectroscopic signature) from the X-ray absorption spectra confirmed the successful synthesis of the Ag NPs with the above-mentioned process. [31,32].

5.2.2. Development of the Detection Setup:

The detection system consisted of three basic components: An LED source, a customized cuvette holder, and the detector. We used a 3 W UV LED with 365 nm wavelength (Ocean

Optics, Florida, USA) and a CCD-based detector (Black-Comet, C-SR-200, StellarNet Inc., USA). The cuvette holder was designed in such a way that the detector and the LED remain orthogonal to each other. An optical filter (Ocean Optics, Florida, USA) with a passband > 400 nm was placed in front of the detector. In this setup, the light passing through the customized cuvette holder excites the sample and, after being scattered, is collected by the detector. A microcontroller (Arduino Uno) was used to control the LED through a solid-state relay. The overall algorithm, including data acquisition, data processing, data analysis, and decision making, was controlled by a self-developed LabVIEW-based software. Figure 5.1 presents a schematic of the self-developed low-cost electro-optical set-up based on 'turn-on' Rayleigh scattering and post sample fluorescence.

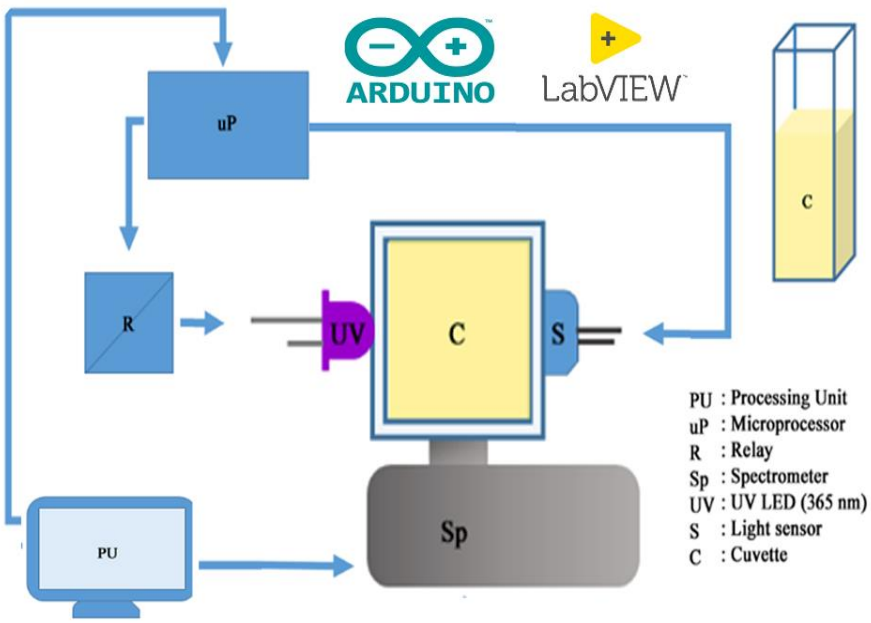

Figure 5.1: *Electro-optical set-up of the proposed device, which works on the principle of 'turn-on' Rayleigh Scattering.*

The UV light excites the sample, and the emission is collected at an angle of 90° relative to the incident light beam by the spectrometer; the absorption of the sample is collected by

an array detector at an angle of 0° relative to the exciting light beam. After passing through the sample, the 465 nm scattered light reaches the filter, which emits a broadband fluorescence light spectrum. An HP filter (λ_{pass} > 400 nm) is used to split the excitation light beam and provide broad-spectrum fluorescence. The HP filter acts as a secondary detector as the scattered light saturates the receiver quickly due to the increased diameter of the Ag NP in the mercury solution. Figure 5.2 presents a schematic of the 'turn-on' scattering sensor for the high-sensitive detection of pollutants (Mercury here). UV light (365 nm) from an LED hits the Ag NPs with an SPR absorption at 420 nm.

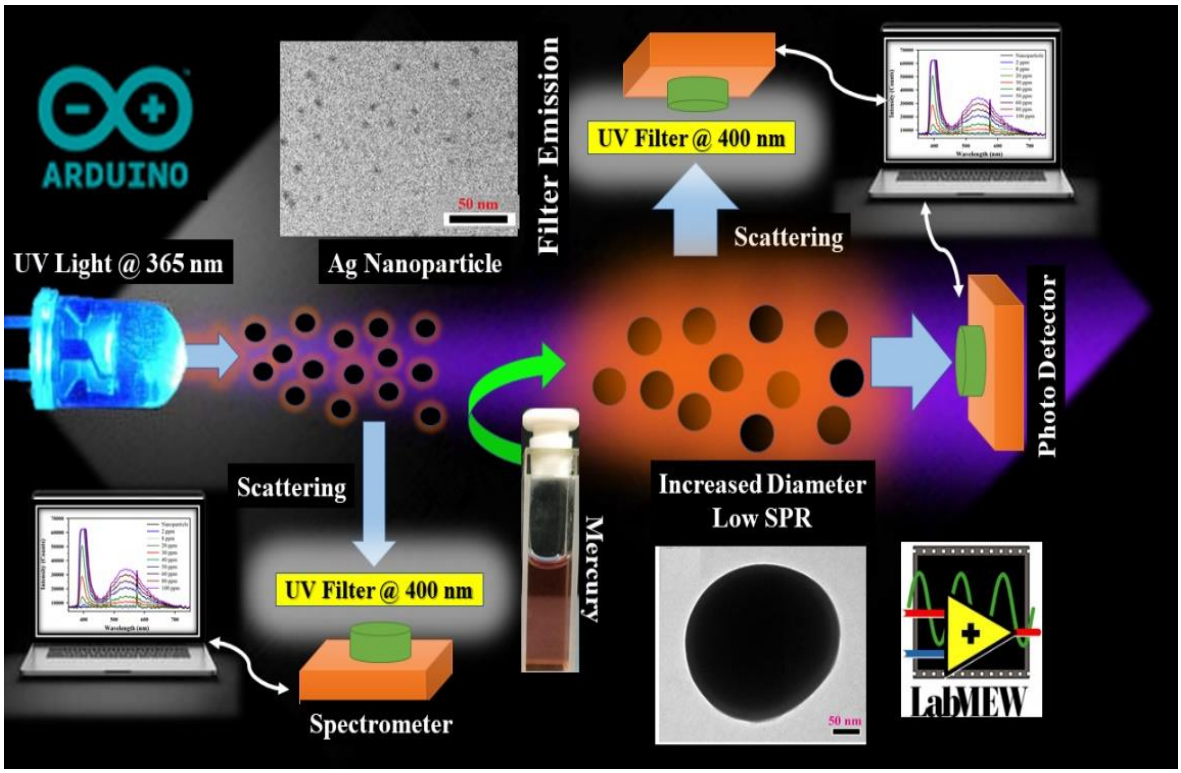

Figure 5.2: *Schematic of 'turn-on' scattering sensor for highly sensitive detection of pollutants (Mercury in this study).*

In the absence of mercury, the NPs exhibit significant absorption of the excitation light and scatter the light very weakly to the HP filter in front of the spectrometer. The light scattered by the HP filter and its fluorescence is shown to peak at 395 and 520 nm,

respectively. In the presence of mercury, the NPs agglomerate, and the overall size of the particles increases, decreasing the SPR absorption and enhancing the light scattering to the HP filter, which eventually increases the fluorescence intensity of the filter.

5.2.3. Software Design:

We developed a user-friendly LabVIEW-based GUI for data acquisition and real-time analysis of the results. The software acquires data sequentially by turning on the LED light, setting the spectrograph parameters, including the wavelength range, integration time, and acquisition interval, and analyzing the data.

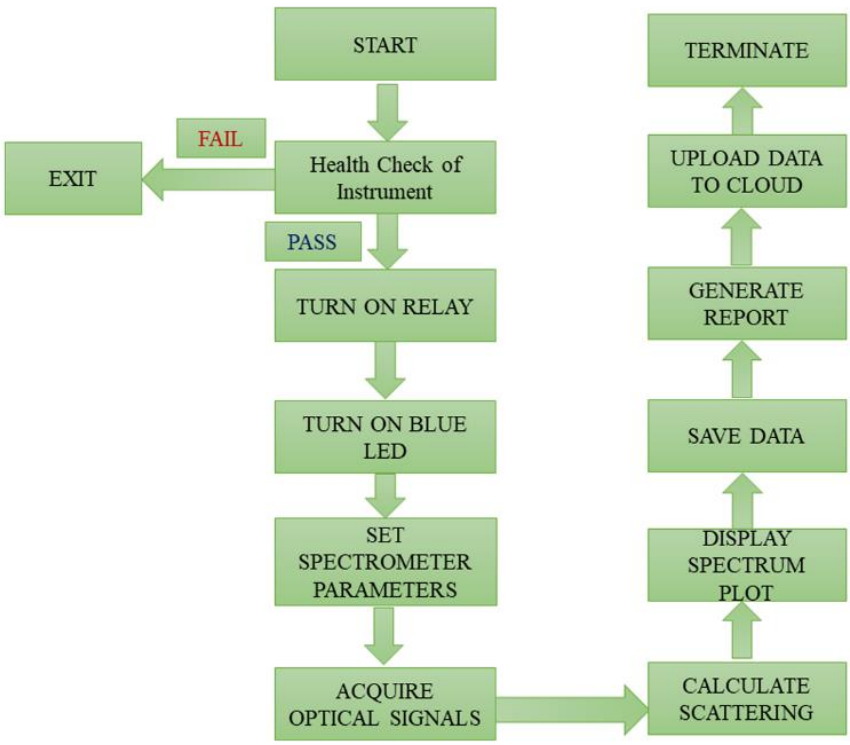

Figure 5.3: *Workflow/algorithm of the self-developed software to control the device with a proper graphical user interface.*

Initially, the software checks the health of various components of the instrument. Subsequently, it turns on the blue LED and initializes the data acquisition; it displays a graph

on the computer screen and stores all desired parameters as ASCII files at the desired location. Figure 5.3 illustrates the workflow/algorithm of the self-developed software to control the device with the proper graphical user interface.

5.2.4. Optical Studies:

A Shimadzu 2600 absorption spectrometer was used to conduct the optical density (OD) spectrometric studies of the films. Water baseline was performed, and data were used as a reference for all OD observations. The particle size and morphology before and after interaction with the heavy metal ions were determined using (HRTEM) high-resolution transmission electron microscopy (FEI Technai S-Twin) with an acceleration voltage of 200 kV. Copper grids coated with carbon were drop-casted with dilute samples to prepare the thin films necessary for HRTEM.

5.3. Results and Discussion:

5.3.1. Interaction of Ag NPs with Poly Vinyle Alcohol (PVA-Ag-NPs):

Optical absorption spectrometry and high-resolution microscopy were employed to characterize the prepared Ag NP. Figure 5.4 displays a TEM image of the citrate-capped Ag NPs (a) before and (b) after interaction with the Hg ions in an aqueous solution. The change in diameter is due to Hg-induced agglomeration. The Ag NPs were found to be sphere-shaped and distributed uniformly throughout the solution. From the TEM image, the mean radius of the particles was calculated to be approximately 5 nm. Figure 5.4(b) illustrates the microscopic data of the NPs with single directional continuous lattice fringes. The inter-planar separation of the Ag NPs was estimated to be approximately 0.23 nm. Figure 5.5 depicts the absorption spectra of the Ag NP before and after interaction with various model

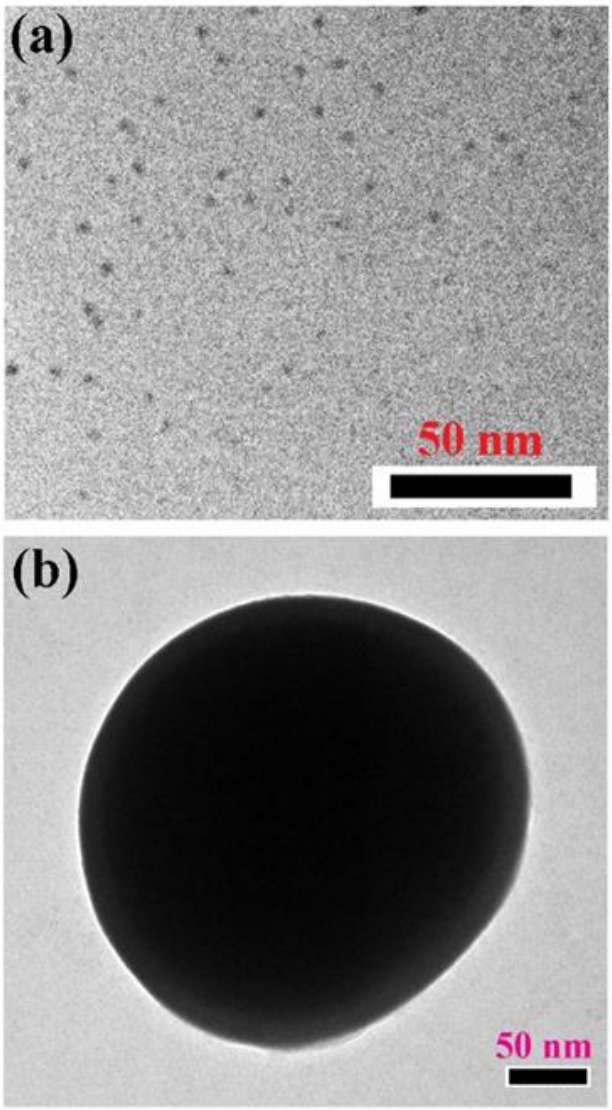

Figure 5.4: *HRTEM images of Ag NPs (a) before and (b) after interaction with mercury ions in aqueous environments. Diameter change is due to* Hg^{2+}*-induced agglomeration.*

pollutants, including mercury, lead, and methylmercury in an aqueous solution. A clear absorbance band peak can be observed from the figure at approximately 395 nm. Dynamic light scattering (DLS) was performed to assess the expected growth of the NPs diameter owing to the addition of mercury, lead, and methylmercury. Figure 5.6 presents the DLS data of the Ag NPs before and after their interaction with the various model pollutants in an aqueous solution. It is observed that the change upon interaction with Hg^{2+} ions is consistent with the HRTEM results. The enhanced particle diameter should trigger an enhanced optical

scattering mechanism, which indicates the concentration of the pollutants in the aqueous solution. This detection strategy of heavy metals in available water can be a potential tool

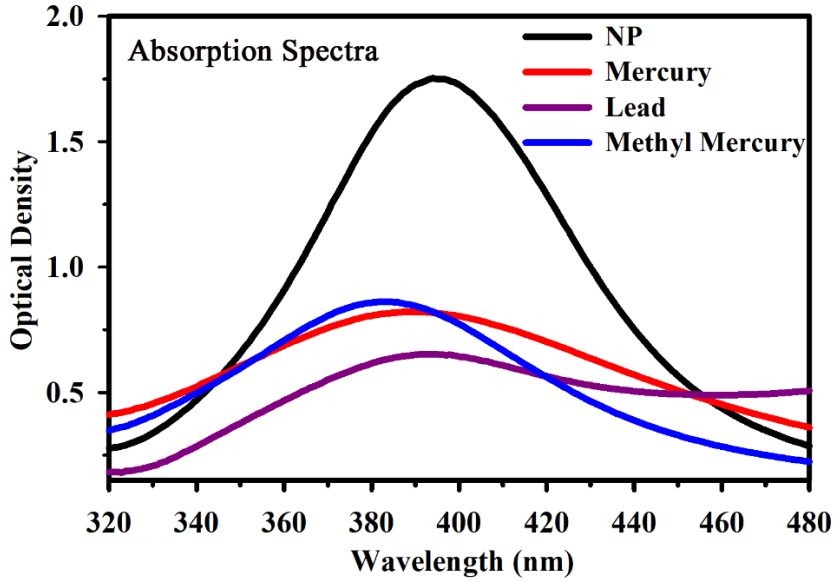

Figure 5.5: *UV-VIS absorption spectra of the Ag NPs before and after their interaction with mercury, lead, and methylmercury in aqueous solution.*

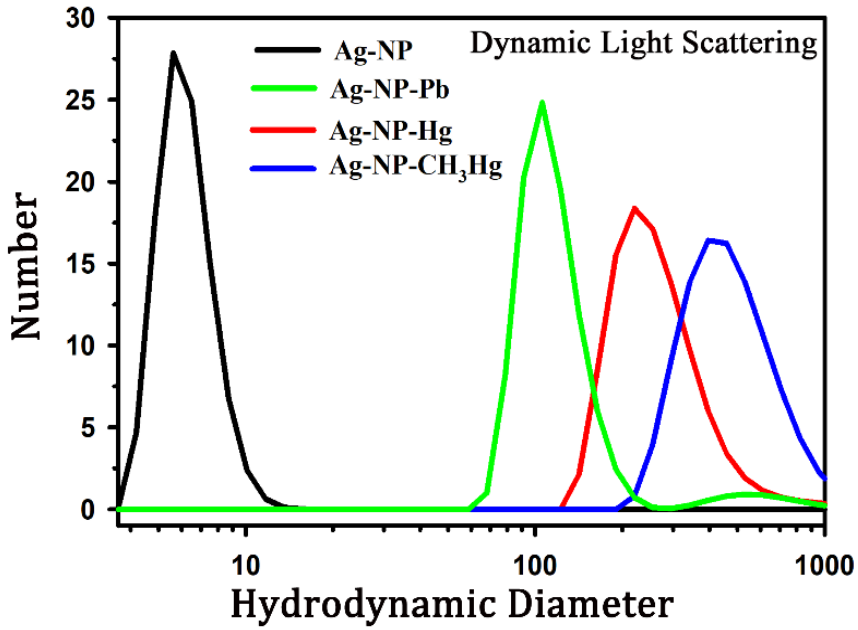

Figure 5.6: *DLS of the Ag NPs before and after interaction with various model pollutants including mercury, lead, and methylmercury in aqueous solution.*

for a quick, easy, and cost-effective way to assess water quality in a point of care setting with a low resource setup.

5.3.2. Sensing Mechanism and Toxic Metal Ions Detection:

The interaction of the Ag NPs with mercury was investigated by studying the SPR spectra before and after the introduction of the Hg^{2+} aqueous solution (Figure 5.7). The spectra

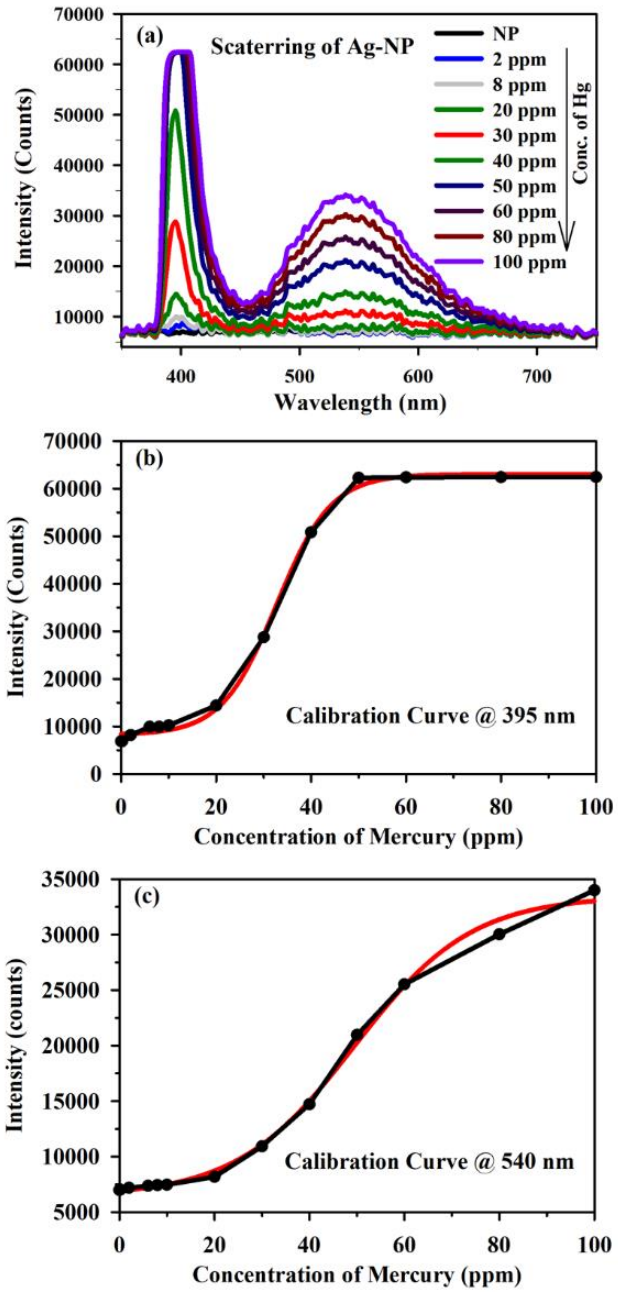

Figure 5.7: *Spectra acquired from the developed device with various concentration of model pollutant (Hg^{2+} ions in water). (a) Post sample emission spectra with peaks at 395 nm (365 nm LED with 50 nm spectral width after 400 nm HP filter) and 520 nm (filter emission). Intensity plot corresponding to various concentrations of Hg^{2+} at (b) 395 nm and (c) 520 nm.*

acquired from the developed device with various concentrations of model pollutants (Hg^{2+} ions in water) were observed. Figure 5.7(a) illustrates the post sample emission spectra with peaks at 395 nm (365 nm LED with 50 nm spectral width after 400 nm HP filter) and 520 nm (filter emission). Figure 5.7 (b) and (c) depict the intensity plots corresponding to various concentrations of Hg at 395 and 520 nm, respectively. A difference in the ion sensitivity and experimental window is observed for different detection wavelengths. As illustrated in the figure, a minor but consistent reduction in the absorbance was observed within a few seconds of the introduction of the lowest possible mercury concentration of 2 ppm.

However, a significant decrease in the spectroscopic peak was observed for higher concentrations of Hg^{2+} ions such as 8 ppm, 30 ppm, 50 ppm, 80 ppm, and 100 ppm (Figure 5.8). (A blue shift in the SPR band was also observed, especially at higher concentrations of Hg^{2+}. Figure 5.8 demonstrates that for few selective concentrations (in the range of 2-100

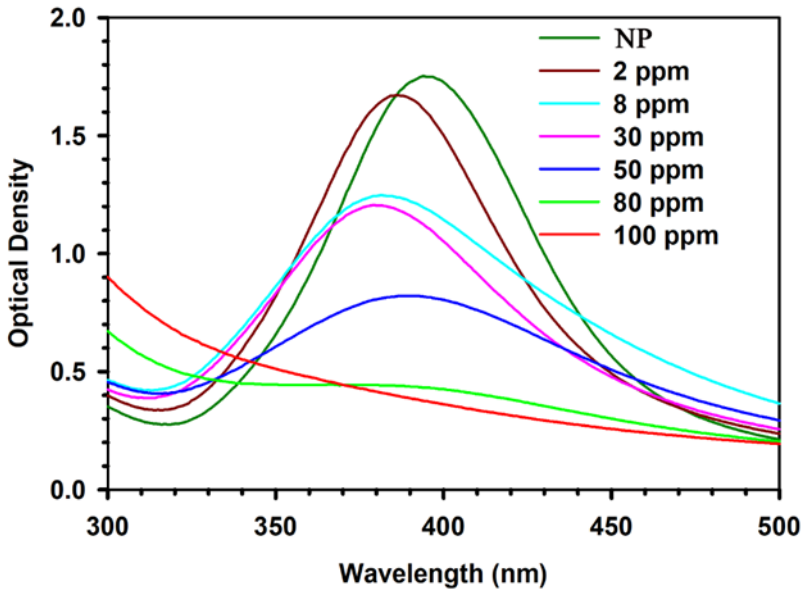

Figure 5.8: *UV-VIS absorption spectra of Ag NPs before and after interaction with various concentrations of mercury ions in aqueous solution.*

ppm) of Hg^{2+} ions, the developed sensor exhibits a non-linear nature, which can be described in the equations as follows

$$Y = \frac{X}{(10.63 + 1.4 * X - 2.66\sqrt{X})} \tag{5.1}$$

where Y represents the difference in OD (I_0 - I), X is the Hg^{2+} ion concentration (in ppm), and I_0 and I are the light intensities of the NPs at 405 nm.

The surface amalgamation or improper amalgamation, resulting in smaller NPs, might be attributed to the blue shift of the SPR band. Nevertheless, a complete amalgamation may occur when inducing agglomeration to develop bigger Ag-Hg NPs [33]. In this study, we have developed an optical technique combining Rayleigh scattering and post-sample fluorescence detection from colloidal Ag NPs having an SPR band at 420 nm. The sensitivity of the developed sensor is exceptionally high because the Rayleigh scattering depends on the sixth power of the particle size. The Ag NPs were seen to increase in size with increasing concentration of the metal ions, in the presence of toxic metal ions. Therefore, the sensitivity of our device is very high. The efficacy of the technique is tested for the detection of several toxic ions including mercury, lead, and methylmercury in aqueous media. Figure 5.8(a) reveals that the light scattering at 395 nm from the Hg-included/inflated Ag NP increased (scattering 'turn-on') with a concentration of mercury ions as low as 2 ppm. However, with higher concentrations of mercury ions, saturation occurred due to the large increase in the particle size, which indicates that the developed technique is highly efficient and sensitive (Figure 5.8(a)). The saturation effect was also predicted by the calibration equation (Eq 5.2) above a 50 ppm concentration, as shown in Figure 5.8(b).

$$Y = \frac{A_2 - A_1}{1 + e^{X - X_0 / dx}} \tag{5.2}$$

where A_2 and A_1 denote the final and initial values respectively. X_0 denotes the center and dx denotes the time constant. The calibration equation reveals that the developed sensor can detect mercury ions in a water medium at concentrations as low as 2 ppm. As mentioned above, the developed sensor cannot determine higher concentrations of pollutants efficiently. For the measurement of higher concentrations of pollutants in a water medium, we use the fluorescence of the HP filter (cut-off at 400 nm) at 520 nm. The HP filter fluorescence is effective in determining concentrations of up to several hundreds of ppm. We have also monitored the concentrations of lead and methylmercury and validated the efficacy of the novel strategy for these pollutants. Figure 5.9 (a) and 10(a) illustrate the scattering spectra

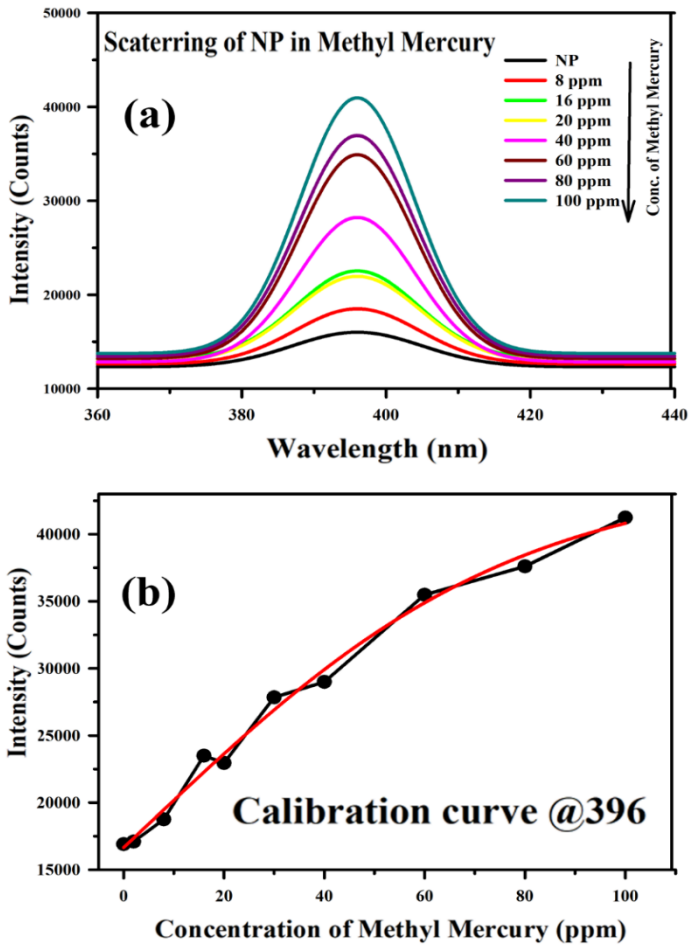

Figure 5.9: *(a) Scattering spectra from the Ag NP with various concentrations of methylmercury. (b) Intensity plot corresponding to various concentrations of methylmercury at 395 nm.*

of the Ag NP with methylmercury and lead, respectively, at various concentrations. Figure 5.9(b) and 5.10(b) represent the intensity plots corresponding to various concentrations of methylmercury and lead at 395 nm. It can be observed from the figures that the scattering

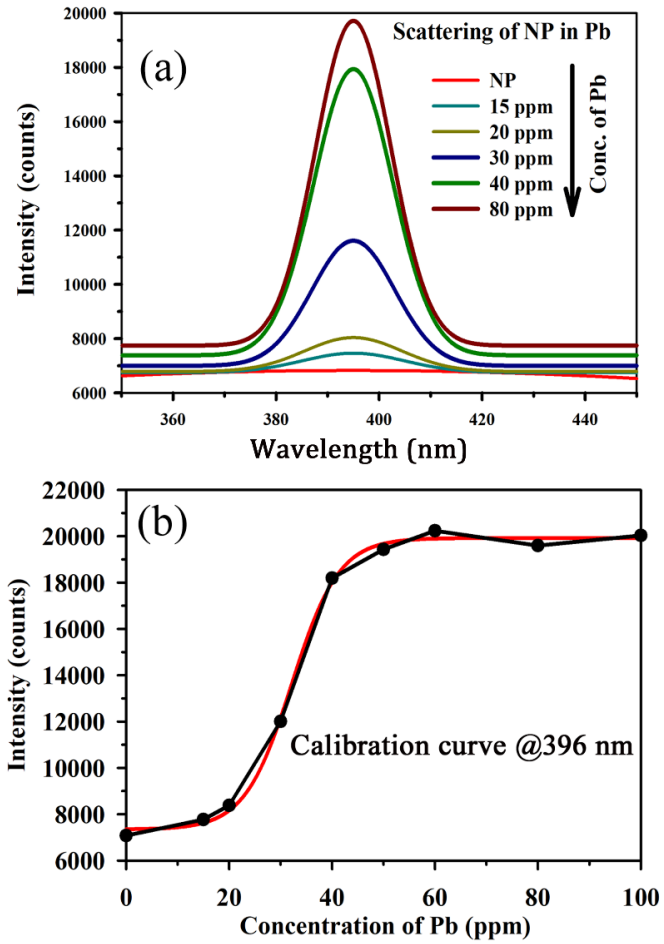

Figure 5.10: *(a) Scattering spectra from the Ag NP with various concentrations of lead. (b) Intensity plot corresponding to various concentrations of lead at 395 nm.*

intensities increase with increasing concentrations of lead and methylmercury. These results demonstrated that the developed technique possesses an excellent potential for the detection of lead and methylmercury in aqueous media.

5.4. Conclusions:

In summary, we have demonstrated that the 'turn-on' Rayleigh scattering relies on the specific interaction of functionalized Ag NPs (SPR at 420 nm) with several model water

pollutants, including mercury, methylmercury, and lead. It can be an efficient alternative strategy for the development of NP-based sensors with enhanced sensitivity in detection with a wider detection window. The decreasing SPR band of the sensor's NPs indicated the interaction of the sensor with the model pollutants, and high-resolution electron microscopy and enhanced Rayleigh scattering of 356 nm excitation light indicated the enlargement of the NPs due to agglomeration. The post sample HP filter offers significant fluorescence upon receiving scattered light at 365 nm, which was shown to be useful for the detection of higher concentrations of pollutant in the test water. We have also using the above strategy to develop a prototype for the detection of model pollutants and demonstrated its efficacy. Furthermore, the so-called Faraday-Tyndall effect was proved to be useful to develop novel NP-based sensors for monitoring model pollutants.

References

[1] M. Lan, J. Zhang, Y.-S. Chui, P. Wang, X. Chen, C.-S. Lee, H.-L. Kwong, W. Zhang, Carbon nanoparticle-based ratiometric fluorescent sensor for detecting mercury ions in aqueous media and living cells, ACS Appl. Mater. Interfaces 6 (2014) 21270.

[2] I. Costas-Mora, V. Romero, I. Lavilla, C. Bendicho, In situ building of a nanoprobe based on fluorescent carbon dots for methylmercury detection, Anal. Chem. 86 (2014) 4536.

[3] A. Renzoni, F. Zino, E. Franchi, Mercury levels along the food chain and risk for exposed populations, Environ. Res. 77 (1998) 68.

[4] D.W. Boening, Ecological effects, transport, and fate of mercury: A general review, Chemosphere 40 (2000) 1335.

[5] P.B. Tchounwou, W.K. Ayensu, N. Ninashvili, D. Sutton, Environmental exposure to mercury and its toxicopathologic implications for public health, Environ. Toxicol.18 (2003) 149.

[6] N. Langford, R. Ferner, Toxicity of mercury, J. Hum. Hypertens. 13 (1999) 651.

[7] R. Kessler, The Minamata Convention on Mercury: A first step toward protecting future generations, Environ. Health Perspect. 121(2013) A304.

[8] S. Díez, S. Delgado, I. Aguilera, J. Astray, B. Pérez-Gómez, M. Torrent, J. Sunyer, J.M. Bayona, Prenatal and early childhood exposure to mercury and methylmercury in Spain, a high-fish-consumer country, Arch. Environ. Contam. Toxicol. 56 (2009) 615.

[9] F.M. Morel, A.M. Kraepiel, M. Amyot, The chemical cycle and bioaccumulation of mercury, Annu. Rev. Ecol. Syst. 29 (1998) 543.

[10] A.F. Castoldi, T. Coccini, S. Ceccatelli, L. Manzo, Neurotoxicity and molecular effects of methylmercury, Brain Res. Bull. 55 (2001) 197.

[11] T. Yorifuji, T. Tsuda, M. Harada, Late Lessons from Early Warnings: Science, Precaution, Innovation, Eur. Environ. Agency 1 (2013) 92.

[12] T.z. Guo, J. Baasner, M. Gradl, A. Kistner, Determination of mercury in saliva with a flow-injection system, Analytica Chimica. Acta 320 (1996) 171.

[13] H.-T. Wang, B. Kang, T. Chancellor Jr, T. Lele, Y. Tseng, F. Ren, S. Pearton, W. Johnson, P. Rajagopal, J. Roberts, Fast electrical detection of Hg (II) ions with AlGaN⁄GaN high electron mobility transistors, Appl. Phys. Lett. 91 (2007) 42114.

[14] K. Leopold, M. Foulkes, P. Worsfold, Methods for the determination and speciation of mercury in natural waters-A review, Anal. Chim. Acta 663 (2010) 127.

[15] A. Bernaus, X. Gaona, J.M. Esbrí, P. Higueras, G. Falkenberg, M. Valiente, Microprobe techniques for speciation analysis and geochemical characterization of mine environments: The mercury district of Almadén in Spain, Environ. Sci. Technol. 40 (2006) 4090.

[16] T. Senapati, D. Senapati, A.K. Singh, Z. Fan, R. Kanchanapally, P.C. Ray, Highly selective SERS probe for Hg (II) detection using tryptophan-protected popcorn shaped gold nanoparticles, ChemComm. 47 (2011) 10326.

[17] Y. Chen, L. Wu, Y. Chen, N. Bi, X. Zheng, H. Qi, M. Qin, X. Liao, H. Zhang, Y. Tian, Determination of mercury (II) by surface-enhanced Raman scattering spectroscopy based on thiol-functionalized silver nanoparticles, Microchim. Acta 177 (2012) 341.

[18] J. Wu, W. Liu, J. Ge, H. Zhang, P. Wang, New sensing mechanisms for design of fluorescent chemosensors emerging in recent years, Chem. Soc. Rev. 40 (2011) 3483.

[19] M. Lan, J. Wu, W. Liu, W. Zhang, J. Ge, H. Zhang, J. Sun, W. Zhao, P. Wang, Copolythiophene-derived colorimetric and fluorometric sensor for visually supersensitive determination of lipopolysaccharide, J. Am. Chem. Soc. 134 (2012) 6685.

[20] M. Lan, W. Liu, Y. Wang, J. Ge, J. Wu, H. Zhang, J. Chen, W. Zhang, P. Wang, Copolythiophene-derived colorimetric and fluorometric sensor for lysophosphatidic acid based on multipoint interactions, ACS Appl. Mater. Interfaces 5 (2013) 2283.

[21] R. Miao, L. Mu, H. Zhang, G. She, B. Zhou, H. Xu, P. Wang, W. Shi, Silicon nanowire-based fluorescent nanosensor for complexed Cu^{2+} and its bioapplications, Nano Lett. 14 (2014) 3124.

[22] M.H. Lee, H.J. Kim, S. Yoon, N. Park, J.S. Kim, Metal ion induced FRET OFF- ON in Tren/Dansyl-appended rhodamine. Organic letters, Org. Lett. 10 (2008) 213.

[23] M.H. Lee, T. Van Giap, S.H. Kim, Y.H. Lee, C. Kang, J.S. Kim, A novel strategy to selectively detect Fe(III) in aqueous media driven by hydrolysis of a rhodamine 6G Schiff base, ChemComm. 46 (2010) 1407.

[24] J.M. Costa-Fernández, R. Pereiro, A. Sanz-Medel, The use of luminescent quantum dots for optical sensing, Trends Analyt. Chem. 25 (2006) 207.

[25] M. Frasco, N. Chaniotakis, Semiconductor quantum dots in chemical sensors and biosensors, Sensors 9 (2009) 7266.

[26] R. Freeman, I. Willner, Optical molecular sensing with semiconductor quantum dots (QDs), Chem. Soc. Rev. 41 (2012) 4067.

[27] S.Y. Yu, Y. J. Chen, J. W. Liaw, Faraday-Tyndall effect of gold colloids, 2015 International Symposium on Next-Generation Electronics (ISNE). IEEE, 2015, 1.

[28] J.-W. Liaw, S.-W. Tsai, H.-H. Lin, T.-C. Yen, B.-R. Chen, Wavelength-dependent Faraday–Tyndall effect on laser-induced microbubble in gold colloid, J. Quant. Spectrosc. Radiat. Transf. 113 (2012) 2234.

[29] G. Zhang, M. Liu, Effect of particle size and dopant on properties of SnO2-based gas sensors, Sens. Actuators B: Chem. 69 (2000) 144.

[30] J.S. Velázquez-González, D. Monzón-Hernández, D. Moreno-Hernández, F. Martínez-Piñón, I. Hernández-Romano, Simultaneous measurement of refractive index and temperature using a SPR-based fiber optic sensor, Sens. Actuators B: Chem. 242 (2017) 912.

[31] C. Flores, C. Diaz, A. Rubert, G. Benítez, M. Moreno, M.F.L. de Mele, R. Salvarezza, P. Schilardi, C. Vericat, Spontaneous adsorption of silver nanoparticles on Ti/TiO2 surfaces: Antibacterial effect on *Pseudomonas aeruginosa*, J. Colloid Interface Sci. 350 (2010) 402.

[32] P.K. Sarkar, N. Polley, S. Chakrabarti, P. Lemmens, S.K. Pal, Nanosurface energy transfer based highly selective and ultrasensitive “turn on” fluorescence mercury sensor, ACS Sens. 1 (2016) 789.

[33] P.K. Sarkar, A. Halder, N. Polley, S.K. Pal, Development of highly selective and efficient prototype sensor for potential application in environmental mercury pollution monitoring, Water Air Soil Pollut. 228 (2017) 314.

Chapter 6

Non-Thermal Atmospheric Plasma (NTAP) Induced Cellular Envelope Damage of *Staphylococcus aureus* and *Candida albicans* Biofilms: Spectroscopic and Bio-Chemical Investigations

6.1. Introduction:

Antibiotics are the main source of therapy against various micro-organisms. However, excessive and uncontrolled use of antibiotics has led to the emergence of various multi-drug resistant strains of micro-organisms [1]. Therefore, finding alternatives for existing antibiotics is of paramount importance [2]. Non-Thermal Atmospheric Plasma (NTAP) promises to be a very suitable alternative method of conventional topical medication of a variety of drug-resistant microbial organisms [3]. NTAP in the biological field has various medical applications like sterilization, blood coagulation, bacterial inactivation, and cancer therapy [4]. The essential advantages of NTAP in the biomedical application include selectivity, targeted activity, and minimal damage to the surrounding living tissues of the target area [5]. It is known that NTAP-induced treatment employs ROS and RNS which are formed during the DBD [6] leading to DNA damage of the living target cells including various harmful microbes.

The co-appearance of Ultraviolet (UV) radiation with NTAP is obvious. The wavelength of radiation depends on the strategy of NTAP generation (the energy content) which includes voltage, power, frequency of operation, and finally the composition and the concentration of gas used (in the case of plasma jet). While a few of the advances in these areas have

demonstrated the feasibility of producing UV-C radiation along with the plasma [7], most researchers have demonstrated the availability of UB-B only [8]. The use of UV light for the micro-organism inactivation is well-studied [9,10]. The effect of UV alone was found to be weak for the purpose, nevertheless, UV was found to behave as an assistant with NTAP facilitating plasma for DNA damage [9]. UV-C although is known to have anti-microbial properties [11], but also is potentially harmful and can act as a mutating agent for short and long-term cell exposure [12]. However, UV-B (290 to 320 nm) is known to be harmful to chronic exposure only [13]. The combinational effect of NTAP with UV was found to be more effective in the inactivation of microbial organisms [14].

NTAP has found its application in various biomedical therapies [15]. It has also been recognized as an important tool for several industrial applications and decontamination of pollutants [16]. Various methods of yielding NTAP has been reviewed and associated limitations have been identified [17]. In this regard, different methods for NTAP generation at ambient condition under atmospheric pressure has been reported [18]. The NTAP generated is activated plasma with short-and long-lived species formation. In a further development, direct discharge of atmospheric NTAP without using any carrier gas has been used for demonstrating rapid blood coagulation [19]. Usage of ambient NTAP has also shown promising results in wound healing/sterilization and is reported to be safe for future external application under prescribed dose [20]. DBD is reported to be one of the efficient ways for the generation of ambient NTAP without the use of any carrier gas [21]. The study explored the dose-dependent effect of NTAP on normal mammalian cells and concluded to be variable from proliferation to the apoptotic limit. Using 220V pulse-based NTAP through direct ionization of ambient air has been reported in the eradication of bacterial biofilms like

Pseudomonas aeruginosa and *Staphylococcus aureus* [22]. Direct and indirect mechanism of action has been reported thoroughly reported in contemporary literature [15]. However, NTAP through DBD for the potential disinfection of biofilms is still demanding.

Here, we have employed time-varying sinusoidal voltage and DBD type of plasma generation process using atmospheric air at ambient conditions without any special carrier gas. We have also designed an electrode using water in glass dielectric, replacing metals for uniform plasma density on the target surface. Our recent study also addresses the contemporary need for an alternative treatment for multi-drug resistant bacterial infection and proper disinfection, which sometimes leads to a complicated pathological condition in humans. Humans, as well as animals, can be infected by the clinical pathogen *Staphylococcus aureus* and *Candida albicans.* The special ability of *S. aureus* to form a multilayer structure that adheres to the extracellular polymeric matrix surface as indwelling medical devices endows it with the potency to cause various nosocomial infections among hospitalized patients [23,24]. The diversity of *S. aureus* virulence presents a huge challenge to eradicate it without making it mutated to tolerate the antibiotic [23]. We have used the ambient air and pressure for the NTAP production which was applied for the destruction of the *S. aureus* biofilm. *S. aureus* contamination on hands is also a serious issue, improper disinfection can lead to severe health hazards [25]. Recently, skin antiseptics have shown a major use in health-care worldwide for the treatment and sterilization of such microbes. However, the cytotoxicity of wounds and skins caused by these medications is a serious problem [26]. In a study, five antiseptics used clinically were tested [27]. Similarly, candidiasis is the most common fungal infection in humans causing invasive diseases like candidemia and candidiasis [28,29]. Additionally, mucocutaneous disorders such as oral

candidiasis, vaginal and vulvovaginal candidiasis, are a matter of increasing concern in contemporary society [30]. The planktonic unicellular form is exhibited by Candida species and show filamentous growth or complex multicellular structure in the infected tissues [31]. In the health care field, the etiology of nosocomial infections and the role of the contaminated hands play during an outbreak is suggestive of the importance of choosing the effective and right "hand hygiene product" [32]. The "hand hygiene" preparations are a major cause of skin irritations and various side-effects [32]. In this regard, NTAP is shown to be safe electrically and can be used for treating living tissues without causing any damage [33]. Application of NTAP at an optimum level has shown to have no toxicity in intact and. normal cells [34].Thus we propose the use of NTAP generated from atmospheric air and using a liquid electrode for a non-contact, efficient, and cost-friendly way for hand hygiene use in various sectors of the medical field as we also show its effectiveness in eradicating *S. aureus* and *C. albicans* biofilm. Taking into consideration all previous developments related to the generation of NTAP we have designed a system capable of producing NTAP in ambient atmospheric air under normal temperature and pressure. The active ingredients of the plasma for the therapeutic efficacy including various ROS and RNS are identified using optical emission spectroscopy of the generated plasma.

6.2. Materials and Methods:

6.2.1. NTAP Generation:

As shown in Figure. 6.1 the setup for (Non-Thermal Atmospheric Plasma)NTAP production was done using a glass di-electric barrier, 15 kV Neon Sign Transformer from Canon, and a high voltage metal electrode. A glass test-tube manufactured by Borosil was

used as a dielectric barrier and ambient atmospheric air acted as the dielectric barrier. In

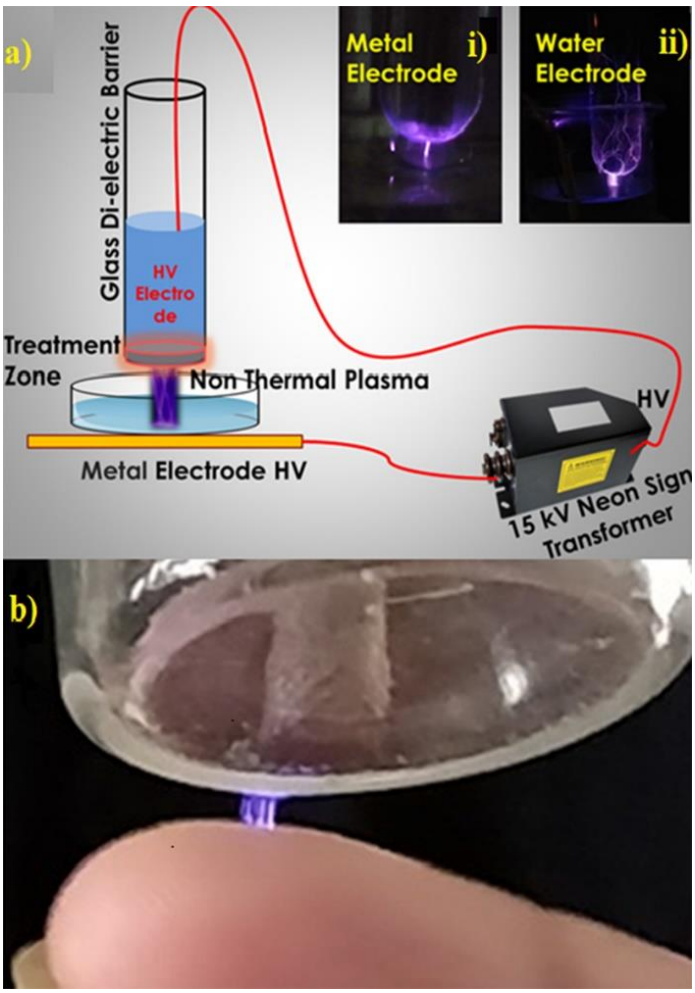

Figure 6.1: *(a) A schematic diagram of the NTAP producing device. In the inset we have shown the two types of high voltage electrode used for generating NTAP i) Metal electrode ii) Water electrode. (b) shows the application of NTAP on bare skin which produces no negative effect.*

order to incorporate uniform plasma density in the application, we have used water in the test tube. Water from a local source with a resistivity value of 1200Ω at 20°C was used as one of the electrodes. The uniform surface coverage of the tip of the test-tube by water makes the DBD discharge to be uniform. The use of water inside test-tube made of flexible dielectric materials would expectedly offer flexibility in various biomedical applications. The Spectroscopic analysis of the generated NTAP was performed using HR4000 (Ocean Optics, Florida, USA) and SpectraSuite software.

6.2.2. Characterization of the DBD-NTAP:

NTAP was generated using a high voltage neon sign transformer. It converts line voltage from 230 V at 50 Hz to 15 kV and is capable of supplying 60 mA current. The output voltage of the transformer was measured using a high voltage probe from Fluke. The electrical characterization of the high voltage was carried out and the results were evaluated for understanding the time-domain representation of the high voltage transformer output (Figure 6.2). The discharge gap was uniformly maintained at 0.5 cm throughout the experiments to

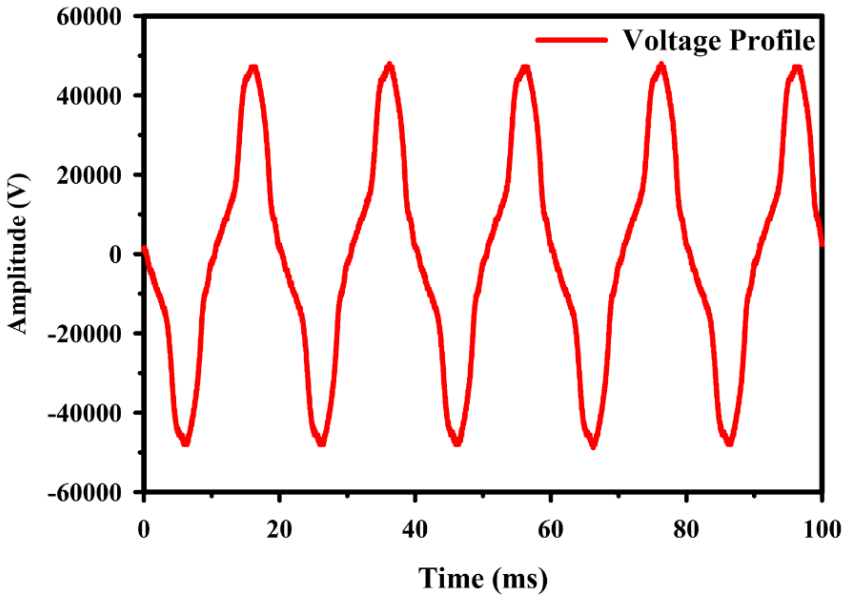

Figure 6.2: *NTAP generated using high voltage transformer of frequency 49.9 Hz of the NTAP measured using a high voltage probe from Fluke.*

maintain constant energy distribution.

6.2.3. Development of Bacterial Biofilms:

Staphylococcus aureus strain was purchased from MTCC (MTCC 3160) [35]. The bacterial culture in Luria broth having optical density OD600 ~1, was spread on 1cm/1cm cleaned Titanium plates and incubated at 37°C for 2 days. Crystal Violet (CV, purchased from Sigma-Aldrich, India) [0.1% (w/v)] was used for performing the quantification process

[36]. Unattached cells were washed with 1 mL of water after being briefly aspirated. After 30 mins of aspiration CV solution (2 mL) was added to the titanium plates kept on a petri dish. titanium plates were washed with 1 mL of water, and 95% ethanol was used to solubilize the remaining CV. The absorbance at 595 nm (A595) was used for the evaluation of the degree of CV staining. The index of bacteria adherence to the titanium plates and formation of biofilm is calculated using the A595 values [37]. Further, a UV-VIS spectrophotometer (Shimadzu UV-2600) was used to measure the extent of CV staining.

To investigate the changes in morphology after the plasma treatment, 200 µL of the *S.aureus* bacterial broth was kept for 48 Hrs at 37°C which was then consecutively washed in water. After fixing the sample with 2.5% glutaraldehyde successive dehydration with alcohol and air was carried out. Scanning electron microscopy (SEM) was performed and the appearance of the biofilm before and after the treatment was qualitatively assessed The coverslips were scanned in a field emission of SEM (Quanta FEG 250: A source of electrons, FEG source; operational accelerating voltage (200V to 30 kV), 3.0 nm resolution, 30 kV under low vacuum conditions: Detectors: Large field secondary electron detector for low vacuum operation) [36] after being coated with gold.

6.2.4. Live-cell Nuclear Magnetic Resonance (NMR) Spectroscopy:

This experiment was done according to a protocol described previously [38]. Briefly, Candida albicans SC5314 cells were grown overnight in YPD (1% yeast extract, 1% peptone, 2% dextrose) broth to get log phase (OD630 = 1.2) of cells. The next day the cells were washed thrice with 10 mM phosphate buffer [25] and re-suspended in the same. OD630nm (107 CFU) cells were treated aseptically with NTAP on a sterilized aluminum foil for 3, 6, and 9 mins respectively, and immediately subjected for NMR analysis.

All NMR experiments were done at 298 K in a Bruker AVANCE III 500MHz spectrophotometer using a 5 mm SMART probe. A series of one-dimensional proton NMR spectra were obtained after each treatment by using 'zgesgp' pulse program with 10% D_2O for locking the sample. The spectral width and number of scans were set to 12 ppm and 64, respectively while the TSP was used as an internal reference (0.0 ppm). Data acquisition and data processing were carried out using TopspinTM v3.5 software (Bruker Biospin, Switzerland).

6.2.5. Fluorescence-Assisted Cell Sorting (FACS):

C. albicans cells were grown in YPD medium and washed with PBS (pH 7.4) three times and then diluted to get 1×10^6 number of cells as described earlier [38]. The test organism was then treated at NPT for 6 and 9 minutes on a sterilized aluminum foil in a Biosafety level 2 laminar airflow workspace. Then the cells were harvested and treated with 3 µL FITC-Annexin V and 2 µL Propidium Iodide (PI) fluorescent dye in a dark room and incubated for 15 and 10 minutes, respectively. Fluorescence Assisted Cell Sorting (FACS) data were acquired by using a BD FACS instrument.

6.2.6. MTT Assay of Mature *C. albicans* Biofilm:

Biofilm viability was measured using the MTT cell proliferation assay reagent (Himedia Laboratories Pvt. Ltd., Mumbai, India) according to the manufacturer's protocol. Briefly, mid-log phase *C. albicans* cells (OD_{630} =0.5), obtained from an overnight culture of stationary phase cells in YPD media were pelleted down by centrifuging at 8000 rpm for 10 min, washed thrice with 10 mM sodium phosphate buffer, (pH 7.4), and re-suspended in the same to get 10^7 cells/mL. Finally, 10^6 cells were seeded on a 1cm/1cm aluminium sheet

submerged in 400 µL RPMI 1640 medium in a sterile 24-well plate and incubated at 37°C in steady condition for 96 Hrs to obtain mature *C. albicans* biofilm. The mature biofilm on aluminum sheets was then washed with buffer to remove non-adherent cells and treated at NPT for 1, 3, 6, and 9 minutes in aseptic condition. Sterile filtered MTT solution (final concentration was 0.5 mg/mL in RPMI 1640) was then added to the treated biofilms and incubated for 3 Hrs in a 37°C incubator. Biofilms were then washed with phosphate buffer (pH 7.4), followed by the addition of 1mL DMSO for dissolving the formazan crystal. The absorbance was measured at 570 nm. Positive and negative controls were prepared by adding 250 µg/mL Amphotericin B and 10 mM phosphate buffer, pH 7.4, respectively. Measurements were performed in triplicate.

6.2.7. Scanning Electron Microscopy (SEM):

C. albicans biofilms were prepared on sterile square aluminium sheets as described above in MTT assay and washed thrice with phosphate buffer solution (pH 7.4) to remove planktonic cells. Next, the NTAP treatment was done following the same time points used in flow cytometry assay, followed by fixing the cells with 2% glutaraldehyde. The samples were then washed thrice in PBS and dried by using 50, 80, and 100 percent ethanol gradation respectively for 5 min each. The gold coating was done before Scanning Electron Microscopy (ZEISS, Germany) data acquisition.

6.3. Results and Discussion:

The cost-effective, easy to use NTAP generator device designed in our present work has been shown in Figure. 6.1(a) A metal rod inside a glass test-tube was used as an active electrode. The counter electrode (a metal sheet) was placed under the region of treatment.

We also used water inside the test-tube instead of using the metal rod in order to generate NTAP. Contrary to other successful techniques like using a plasma jet to carry reactive oxygen and nitrogen species (RONS) to the sample under test, we have used a relatively simpler technique to electrify air using high voltage and hence keep the consumable cost down, as the research would lead to a plasma-based sterilizer to be used under low resource setting. The photographs of the generated NTAP using metal and water electrodes are shown in the insets of Figure 6.1(a). In a different experimental strategy, NTAP can also be generated in absence of a real counter electrode (floating electrode dielectric barrier discharge [39]. The strategy ensures flexibility of application and enhances the scope of the treatment in the human subject as shown in Figure 6.1(b).

We have analyzed the spectral components of the NTAP generated in metal, water, and floating electrode configurations using an optical spectrograph of 1 nm resolution as shown in Figure 6.3. It is known that all activated species do not emit light, but a species emitting

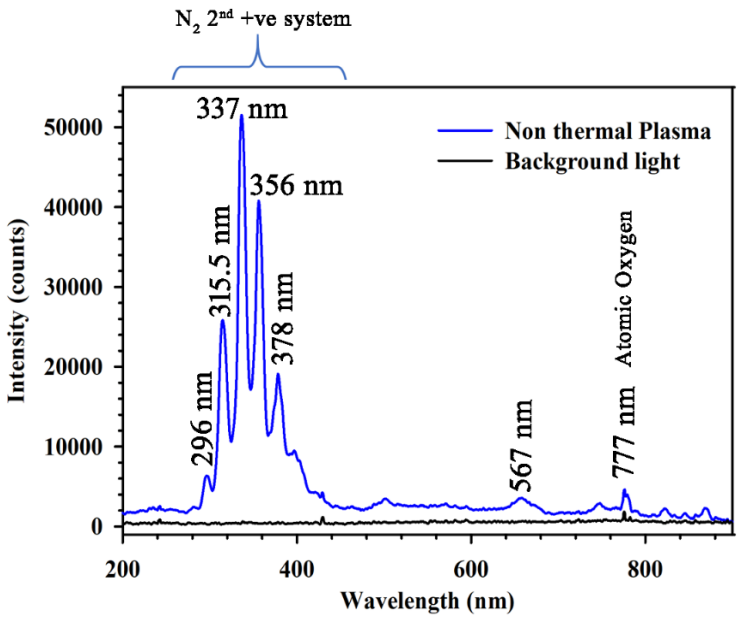

Figure 6.3: *The spectrophotometric atomic emission data obtain from NTAP showing the presence of various peaks at different wavelengths denoting the composition of NTAP.*

is considered to be the parameter of utmost importance due to its capability of performing high cellular influence [40].

It is well known that cold plasma when operated in air, releases an abundance of reactive oxygen and nitrogen species (RONS) [41]. The interactions of such species with biological target cells have been thoroughly explained in contemporary literature [42-47]. The emission lines appearing in Figure 6.3 are mostly identified as transitions of molecular nitrogen. The first positive system [N_2 * ($B^3\ \Pi_g$-$A^3\ \sum^+_u$)] transitions) is in the 500 -900 nm range, and the second positive system [N_2 * ($C^3\ \Pi_u$-$B^3\ \sum_g$)] transitions) is in the 300 -500 nm range (e.g., 337 and 354 nm). It is notable that the 777 nm wavelengths of the atomic oxygen system were also detected [48-51]. H alpha line was also observed at 656 nm.

N_2* emission lines can be broadly classified into two parts namely radiative [N_2 * ($C^3\ \Pi_u \rightarrow B^3\ \Pi_g$)] and meta-stable [$N_2$ * ($B^3\ \Pi^+_u \rightarrow A^3\ \sum^+_u$)] state, which can be attributed to high energy electron over 6.1 eV whereas, N_2^+ formation can be attributed to reactions of N_2* metastable molecules by penning ionization [52].

It is reported that free radicals contain unpaired electrons to become highly reactive [53]. These free radicals have the capacity to produce cell damage because of their oxidizing property [53]. Application of such reactive species causes the inactivation of bacterial biofilms and cause cell death. ROS and RNS produced by NTAP contribute to causing cell damage by creating redox reactions in various biomolecules ranging from lipids, proteins to DNA and RNA [54]. The concentration of Reactive species with a similar set-up was calculated in a recent scientific work [55]. We investigated the effect of NTAP on biofilm growth of S. aureus on a titanium plate prepared in the laboratory. Biofilm is a microbial

community encapsulated within a matrix which consists of an intensive network of cells that are attached to abiotic surfaces [56].

Biofilm formed by *S. aureus* was considered for NTAP treatment after 48 Hrs of incubation. The titanium plate was treated with NTAP for a period of five minutes and then CV staining was used for the quantitative assay of the total adhered biomass of *S. aureus* biofilm in the control and the NTAP treated titanium plates. The plasma-treated titanium plates showed no marked staining with CV as shown in Figure 6.4(b) whereas in the control

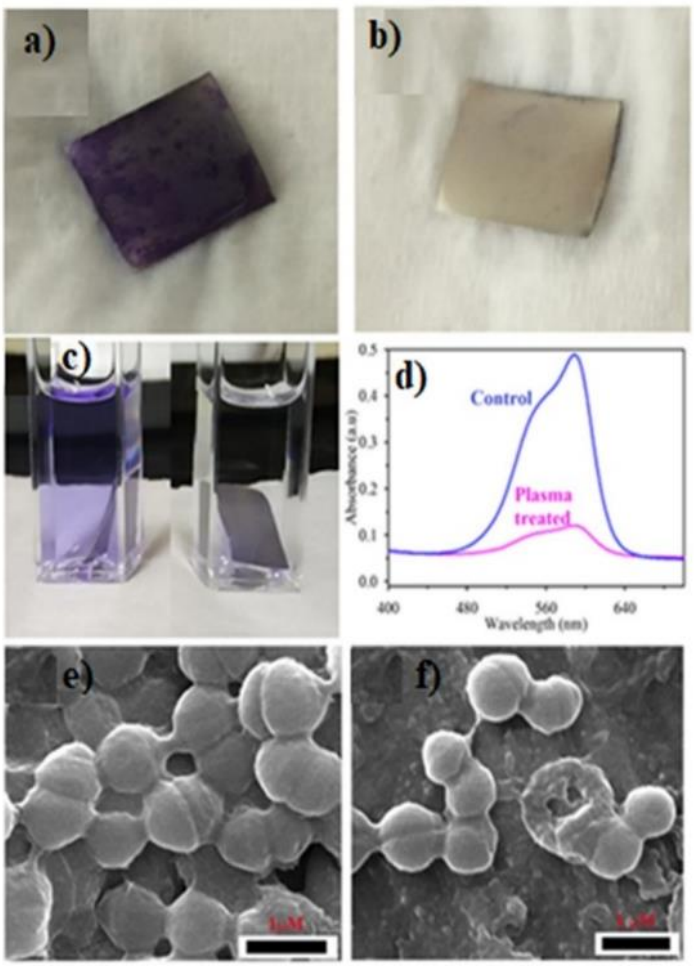

Figure 6.4: *Anti-Biofilm effect of NTAP on S. aureus bacterial biofilm (a) CV-stained biofilm in titanium plate. (b) S. aureus biofilm in titanium plate after being treated with NTAP and CV. Untreated (control) S. aureus. (c) Cuvette containing treated and untreated titanium plates immersed in 95% alcohol. (d) Spectrophotometric absorbance data at A595 for control and NTAP treated samples. (e) SEM image of untreated (Control) S. aureus biofilm (f) SEM images of NTAP treated S. aureus biofilm. Scale= 1µM.*

or untreated titanium plate presence of CV stain was visually evident as shown in Figure 6.4(a). Spectroscopic analysis of the solubilized CV (using 95% alcohol) was monitored by the absorbance at 595 nm. As the S. aureus Biofilm was completely eradicated after NTAP treatment as shown in Figure 6.4(c) CV was absent on the titanium plates and hence the A595 of the plasma-treated biofilm showed a marked decrease in intensity at the complementary absorbance depicted in Figure 6.4(d). Whereas the untreated bacterial biofilm had the presence of CV showing a marked increase at A595 absorbance peak for the presence of CV showing that the biomass of Biofilm was intact in the control or untreated plates as shown in Figure 6.4(d).

Hence treatment with NTAP exhibits the inhibition of bacterial biofilm growth. The SEM images were used for detecting structural and morphological changes of the biofilms. Figure 6.4(e) shows typical characteristics of *S. aureus* biofilms with intact cell membrane. Whereas Figure 6.4(f) shows significant changes in the morphology of the *S. aureus* biofilm with the destruction of the cell membrane of the plasma-treated sample it also shows the significantly lesser number of bacteria with loss in the proper arrangement of bacterial biofilm. The design of plasma-assisted hand sanitization has been reported to be efficient in eradicating bacteria [57]. To understand the effect of NTAP treatment on fungal cells, *Candida albicans* was used as a model system as it is well known for its deadly infections in immunocompromised patients [38].

Nuclear Magnetic Resonance (NMR) spectroscopy is a powerful technique to probe small chemical changes in a system at atomistic resolution. Solution state live-cell NMR analysis provided insight into the morphological changes of the microbial cells before and after the treatment of NTAP. To understand these changes, a series of one-dimensional proton (^{1}H)

NMR spectra were obtained by using processed *C. albicans* cells with a different treatment time of NTAP. The spectra were then compared as shown in Figure 6.5(a). Several new peaks were observed in the sample that was administered for 3 min only as compared with the negative control.

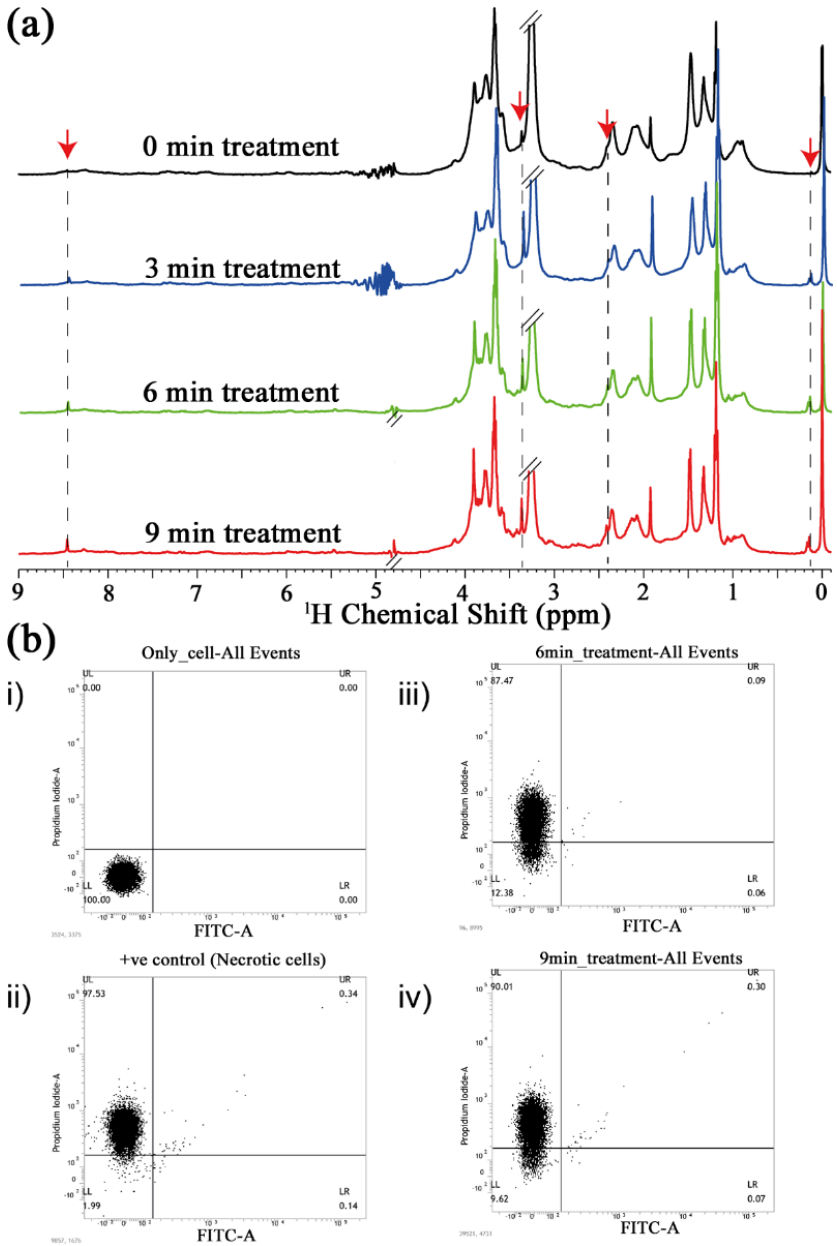

Figure 6.5: *One-dimensional NMR of C. albicans cells in the absence and after NTAP treatment with respective time points. (A) Several new sharp peaks were obtained after NTAP treatment when compared to a control cell (0 min treatment). FACS analysis. albicans cells (i) and after NTAP treatment cells for (ii) 6 min [B(iii)] and 9min, B(iv) indicates that the microorganism is following as compared to positive control [B(ii)].*

However, with increasing the treatment time till 9 min, no other ^{1}H peaks were detected, but the intensity of the new peaks got increased suggesting that the integrity of the cells got compromised and thus small metabolites were released from the altered fungal cells. The new peaks mostly came out between 0.62 - 3.35 ppm which corresponds to the upfield region and downfield regions contain only one ^{1}H peak that came at around 8.44 ppm. Thus, live-cell NMR data suggests that some alterations are happening after 3-9 minutes of NTAP treatment.

To understand if this process leads to apoptotic, necrotic, autophagy, or necrotic pathway of the fungal cells, FACS analysis was done in the next step to decipher the cell death mechanism of the treated cells. Figure 6.5(b) showed that the control cells (i) got no dye uptake in the dual dye cytometric analysis but interestingly a significant number of NTAP treated cells (both 6 and 9 minutes) had taken the propidium iodide (PI) dye than Annexin V. Annexin V is a calcium-dependent protein which binds preferentially with phosphatidylserine (PS) residues generally present in the inner leaflet of the plasma membrane.

If the cells follow programmed cell death or apoptotic pathway, then the PS lipids stay outside of the cell membrane and thus Annexin V get binds with it. On the contrary, propidium iodide (PI) is a cell-impermeant dye and only gets inside the cells when the cell barrier gets compromised.

The FACS data thus suggests that the fungal cells are either following a necrotic or late apoptotic pathway as compared with the positive control cells (ii) because there are no Annexin V signals were obtained in the whole treated population. To extend the application of NTAP as a potential tool to eradicate the resistant fungal biofilm, mature *C. albicans*

biofilms were developed on a square 1cm aluminium sheet. Plasma treatment was done at

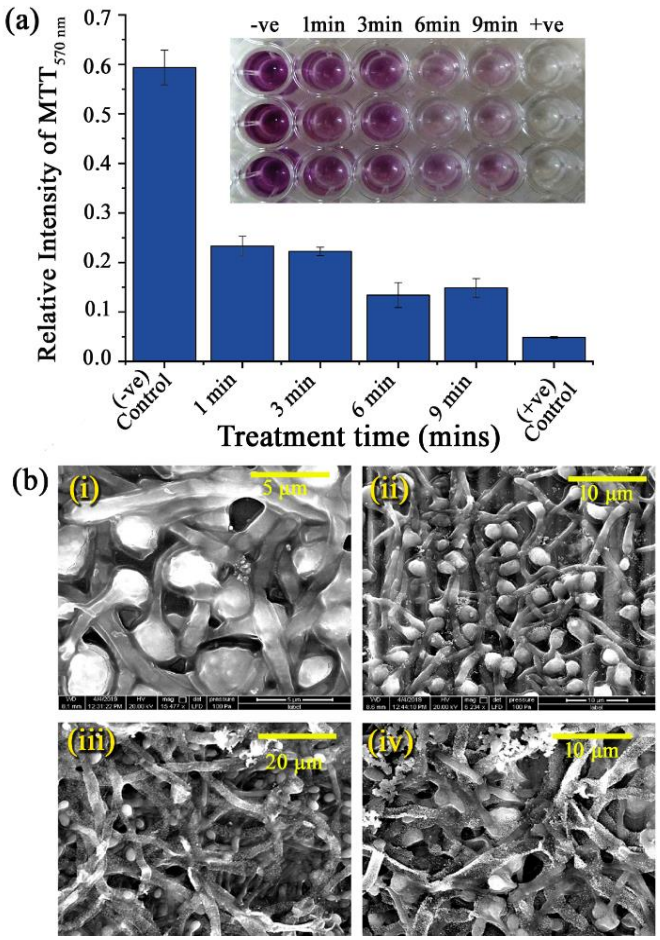

Figure 6.6: *(A) Cell viability assay of mature C. albicans biofilm. The intensity of the pink color (as shown in inset) indicates that more cells are alive in control but faded with increasing NTAP treatment time. (B) SEM images show that control biofilm is unaltered, but 6min and 9 min treated biofilms got degraded (scale 5-20µm).*

different time points starting from 1 min to 9 min, and the samples were subjected to cell viability assay or MTT assay and scanning electron microscopy (SEM) as well. Figure 6.6(a) showed a histogram plot depicting the relative intensity of the MTT at 570 nm in different sets. MTT assay provides information about the level of cellular activity using enzymatic functions. The trend of the intensity plot after NTAP treatment suggests that the viability of the fungal biofilm got gradually decreased and reach around 25% on 6 and 9-min treatment as compared to the positive control. This result correlates with NMR and FACS analysis and

suggests that plasma treatment has an adverse effect on such highly resistant pathogen. The SEM images as shown in Figure 6.6(b) also supports this finding as it is visible that the 6 and 9 min treatment had made the biofilms rough and dried whereas the control set remained smooth and unaltered. Figure 6.6(b) (iii) and (iv) showed that the cellular morphology of the *C. albicans* cells in biofilm condition got drastic change and directly indicates a necrotic cell death which again correlates with FACS analysis. Our group is actively involved in the design and development of a non-thermal plasma-based hand sanitizer without the use of consumable gas for low resource setting areas. The setup is equipped with a proximity sensor to detect the presence of hands and automatically generate a plasma shower for large scale sanitization at public places.

6.4. Conclusion:

To summarize, ambient air non-thermal plasma was generated using 15 kV potential difference, and utilizing the principle of DBD and the effect of the generated plasma on *S. aureus* and *C. albicans* biofilm was observed. The possibility of using various flexible materials e.g., a liquid electrode was investigated and found to be effective in the successful generation of NTAP. The use of ambient atmospheric air for the production of NTAP has also been designed. Atomic emission spectroscopy was utilized to evaluate the components of the generated NTAP and its mechanism of action was carefully investigated. It was found that the generated plasma was effective in dis-adherence of *S. aureus* biofilm from titanium plate. We are in the process of developing NTAP based hand sanitizer equipment. We have used 220 V, 50 Hz current, and a high voltage neon transformer for producing NTAP. Water was used as an electrode and glass acted as the dielectric barrier. The diagram depicts the NTAP shower which is to be used for hand sanitization. The setup is equipped with a

proximity sensor to detect the presence of hands and automatically generate a plasma shower.

The effect of NTAP was also investigated on *C. albicans* biofilm and the inactivation process was studied. The formation of new peaks in NMR spectra was observed confirming the compensation of integrity of cells. This was further established from SEM images of bacteria and fungi which show cell death occurs after application of NTAP. The presence of RONS in the non-thermal plasma is known to be the anti-microbial agent and hence can be an effective tool for the design of a low-cost-sterilizer under a low resource setting. The potential of the setup and the ease of installation was utilized to design and develop a wall-mounted instrument capable of generating NTAP for potential use in hand sanitization in the non-invasive and non-contact method without the application of any chemical. The set-up is extremely cost-effective and easy to use. We believe this set-up will be a cheap alternative to the conventional method of disinfection from *S. aureus* and *C. albicans* and can be used in public places e.g., hospital environments for hand and hospital tool sterilization.

References

[1] H. Harbottle, S. Thakur, S. Zhao, D. White, Genetics of antimicrobial resistance, Anim. Biotechnol. 17 (2006) 111.

[2] R. Khan, B. Islam, M. Akram, S. Shakil, A.A. Ahmad, S.M. Ali, M. Siddiqui, A. Khan, Antimicrobial activity of five herbal extracts against multi drug resistant (MDR) strains of bacteria and fungus of clinical origin, Molecules 14 (2009) 586.

[3] J.H. Park, N. Kumar, D.H. Park, M. Yusupov, E.C. Neyts, C.C. Verlackt, A. Bogaerts, M.H. Kang, H.S. Uhm, E.H. Choi, A comparative study for the inactivation of multidrug resistance bacteria using dielectric barrier discharge and nano-second pulsed plasma, Sci. Rep. 5 (2015) 13849.

[4] L.A. Torre, R.L. Siegel, A. Jemal, A. Ahmad, S. Gadgeel (Eds.), Lung cancer statistics, in lung cancer and personalized medicine: Current knowledge and therapies, 2016, Switzerland, Springer.

[5] G. Morfill, M.G. Kong, J. Zimmermann, Focus on plasma medicine, New J. Phys. 11 (2009) 115011.

[6] J. Chauvin, F. Judée, M. Yousfi, P. Vicendo, N. Merbahi, Analysis of reactive oxygen and nitrogen species generated in three liquid media by low temperature helium plasma jet, Sci. Rep. 7 (2017) 4562.

[7] Y. Zhang, Y. Li, Y. Li, S. Yu, H. Li, J. Zhang, A novel approach to the pacemaker infection with non-thermal atmospheric pressure plasma, Eur. Phys. J. Spec. Top. 226 (2017) 2901.

[8] N.N. Misra, K.M. Keener, P. Bourke, J.P. Mosnier, P.J. Cullen, In-package atmospheric pressure cold plasma treatment of cherry tomatoes, J. Biosci. Bioeng. 118 (2014) 177.

[9] H. Liu, J. Chen, L. Yang, Y. Zhou, Long-distance oxygen plasma sterilization: Effects and mechanisms, Appl. Surf. Sci. 254 (2008) 1815.

[10] B. Gweon, D. Kim, S. Moon, W. Choe, *Escherichia coli* deactivation study controlling the atmospheric pressure plasma discharge conditions, Curr. Appl. Phys. 9 (2009) 625.

[11] M. Erkan, C.Y. Wang, D.T. Krizek, UV-C irradiation reduces microbial populations and deterioration in cucurbitapepo fruit tissue, Environ. Exp. Bot. 45 (2001) 1.

[12] P. Musk, R. Campbell, J. Staples, D. Moss, P. Parsons, Solar and UVC-induced mutation in human cells and inhibition by deoxynucleosides, Mutat. Res. Lett. 227 (1989) 25.

[13] S.G. Coelho, W. Choi, M. Brenner, Y. Miyamura, Y. Yamaguchi, R. Wolber, C. Smuda, J. Batzer, L. Kolbe, S. Ito, Short-and long-term effects of UV radiation on the pigmentation of human skin, J. Investig. Dermatol. 14 (2009), 32.

[14] K.B. Andersen, A. Feilberg, J. Beukes, Use of non-thermal plasma and UV-light for removal of odour from sludge treatment, Water Sci. Technol. 66 (2012) 1656.

[15] M. López, T. Calvo, M. Prieto, R. Múgica-Vidal, I. Muro-Fraguas, F. Alba-Elías, A. Alvarez-Ordóñez, A review on non-thermal atmospheric plasma for food preservation: Mode of action, determinants of effectiveness, and applications, Front. Microbiol.10 (2019) 1.

[16] A. Mizuno, Industrial applications of atmospheric non-thermal plasma in environmental remediation, Plasma Phys. Control. Fusion. 49 (2007) A1.

[17] G. Petitpas, J.D. Rollier, A. Darmon, J. Gonzalez-Aguilar, R. Metkemeijer, L. Fulcheri, A comparative study of non-thermal plasma assisted reforming technologies, Int. J. Hydrog. Energy 32 (2007) 2848.

[18] A. Fridman, A. Chirokov, A. Gutsol, Non-thermal atmospheric pressure discharges, J. Phys. D: Appl. Phys. 38 (2005) R1.

[19] S. Kalghatgi, G. Fridman, M. Balasubramanian, A. Brooks, V. Vasilets, A. Fridman, A. Gutsol, G. Friedman, Mechanism of blood coagulation by non-thermal atmospheric pressure dielectric barrier discharge, Blood 110 (2007) 3162.

[20] A.S. Wu, S. Kalghatgi, D. Dobrynin, R. Sensenig, E. Cerchar, E. Podolsky, E. Dulaimi, M. Paff, K. Wasko, K.P. Arjunan, K. Garcia, G. Fridman, M. Balasubramanian, R. Ownbey, K.A. Barbee, A. Fridman, G. Friedman, S.G. Joshi, A.D. Brooks, Porcine intact and wounded skin responses to atmospheric nonthermal plasma, The J. Surg. Res. 179 (2013) e1.

[21] S. Kalghatgi, C.M. Kelly, E. Cerchar, B. Torabi, O. Alekseev, A. Fridman, G. Friedman, Effects of non-thermal plasma on mammalian cells, J. Azizkhan-Clifford, PloS One 6 (2011) e16270.

[22] J.R. Ferrell, F. Shen, S.F. Grey, C.J. Woolverton, Pulse-based non-thermal plasma (NTP) disrupts the structural characteristics of bacterial biofilms, Biofouling 29 (2013) 585.

[23] C. Kong, C.-F. Chee, K. Richter, N. Thomas, N. Abd. Rahman, S. Nathan, Suppression of *Staphylococcus aureus* biofilm formation and virulence by a benzimidazole derivative, Sci. Rep. 8 (2018) 2758.

[24] A.E. Paharik, A.R. Horswill, The staphylococcal biofilm: Adhesins, regulation, and host response, Microbiol. Spectr. 4 (2016).

[25] A.A. Lambrechts, I.S. Human, J.H. Doughari, Bacterial contamination of the hands of food handlers as indicator of hand washing efficacy in some convenient food industries in South Africa, Pak. J. Med. Sci. 30 (2014) 755.

[26] A. Fleming, The action of chemical and physiological antiseptics in a septic wound, Br. J. Surg. 7 (1919) 99.

[27] T. Hirsch, A. Koerber, F. Jacobsen, J. Dissemond, H.U. Steinau, S. Gatermann, S. Al-Benna, M. Kesting, H.M. Seipp, L. Steinstraesser, Evaluation of toxic side effects of clinically used skin antiseptics in vitro, J. Surg. Res. 164 (2010) 344.

[28] E. Concia, A.M. Azzini, M. Conti, Epidemiology incidence and risk factors for invasive candidiasis in high-risk patients, Drugs 69 (2009) 5.

[29] J. Sardi, L. Scorzoni, T. Bernardi, A. Fusco-Almeida, M.M. Giannini, Candida species: Current epidemiology, pathogenicity, biofilm formation, natural antifungal products and new therapeutic options, J. Med. Microbiol. 62 (2013) 10.

[30] B. Havlickova, V.A. Czaika, M. Friedrich, Epidemiological trends in skin mycoses worldwide, Mycoses 51 (2008) 2.

[31] F. Hasan, I. Xess, X. Wang, N. Jain, B.C. Fries, Biofilm formation in clinical candida isolates and its association with virulence. Microbes and infection, Microbes Infect. 11 (2009) 753.

[32] G. Kampf, A. Kramer, Epidemiologic background of hand hygiene and evaluation of the most important agents for scrubs and rubs, Clin. Microbiol. Rev. 17 (2004) 863.

[33] J.J. Vargo, Clinical applications of the argon plasma coagulator, Gastrointest. Endosc. 59 (2004) 81.

[34] D. Dobrynin, S. Kalghatgi, G. Fridman, A. Wu, E. Podolsky, K. Barbee, A. Brooks, A. Fridman, G. Friedman, Toxicity of direct nonthermal plasma treatment of living tissue, IEEE Int. Conf. Plasma Sci. (2009) 1.

[35] G. Applerot, A. Lipovsky, R. Dror, N. Perkas, Y. Nitzan, R. Lubart, A. Gedanken, Enhanced antibacterial activity of nanocrystalline zno due to increased ros-mediated cell injury, Adv. Func. Mater. 19 (2009) 842.

[36] D. Bagchi, S. Dutta, P. Singh, S. Chaudhuri, S.K. Pal, Essential dynamics of an effective phototherapeutic drug in a nanoscopic delivery vehicle: Psoralen in ethosomes for biofilm treatment, ACS Omega 2 (2017) 1850.

[37] T. Mathur, S. Singhal, S. Khan, D.J. Upadhyay, T. Fatma, A. Rattan, Detection of biofilm formation among the clinical isolates of Staphylococci: An evaluation of three different screening methods, Ind. J. Med. Microbiol. 24 (2006) 25.

[38] S.A. Mohid, A. Ghorai, H. Ilyas, K.H. Mroue, G. Narayanan, A. Sarkar, S.K. Ray, K. Biswas, A.K. Bera, M. Malmsten, Application of tungsten disulfide quantum dot-conjugated antimicrobial peptides in bio-imaging and antimicrobial therapy, Colloids Surf. B Biointerfaces 176 (2019) 360.

[39] G. Fridman, A. Shereshevsky, M.M. Jost, A.D. Brooks, A. Fridman, A. Gutsol, V. Vasilets, G. Friedman, Floating electrode dielectric barrier discharge plasma in air

promoting apoptotic behavior in melanoma skin cancer cell lines, Plasma Chem. Plasma Process. 27 (2007) 163.

[40] J. H. Lee, E. H. Choi, K. M. Kim, K. N. Kim, Effect of non-thermal air atmospheric pressure plasma jet treatment on gingival wound healing, J. Phys. D: Appl. Phys. 49 (2016) 75402.

[41] B. Ghimire, E.J. Szili, P. Lamichhane, R.D. Short, J.S. Lim, P. Attri, K. Masur, K. D. Weltmann, S. H. Hong, E.H. Choi, The role of UV photolysis and molecular transport in the generation of reactive species in a tissue model with a cold atmospheric pressure plasma jet, Appl. Phys. Lett. 114 (2019) 093701.

[42] S. Ikawa, A. Tani, Y. Nakashima, K. Kitano, Physicochemical properties of bactericidal plasma-treated water, J. Phys. D: Appl. Phys. 49 (2016) 425401.

[43] T. Kobayashi, N. Iwata, J. S. Oh, H. Hahizume, T. Ohta, K. Takeda, K. Ishikawa, M. Hori, M. Ito, Bactericidal pathway of Escherichia coli in buffered saline treated with oxygen radicals, J. Phys. D: Appl. Phys. 50 (2017) 155208.

[44] P. Attri, J. Han, S. Choi, E.H. Choi, A. Bogaerts, W. Lee, CAP modifies the structure of a model protein from thermophilic bacteria: Mechanisms of CAP-mediated inactivation, Sci. Rep. 8 (2018) 1.

[45] P. Shaw, N. Kumar, H.S. Kwak, J.H. Park, H.S. Uhm, A. Bogaerts, E.H. Choi, P. Attri, Bacterial inactivation by plasma treated water enhanced by reactive nitrogen species, Sci. Rep. 8 (2018) 1.

[46] J.H. Park, N. Kumar, D.H. Park, M. Yusupov, E.C. Neyts, C.C. Verlackt, A. Bogaerts, M.H. Kang, H.S. Uhm, E.H. Choi, A comparative study for the inactivation

of multidrug resistance bacteria using dielectric barrier discharge and nano-second pulsed plasma, Sci. Rep. 5 (2015) 1.

[47] P. Sun, H. Wu, N. Bai, H. Zhou, R. Wang, H. Feng, W. Zhu, J. Zhang, J. Fang, Inactivation of Bacillus subtilis spores in water by a direct-current, cold atmospheric-pressure air plasma microjet, Plasma Process. Polym. 9 (2012) 157.

[48] Y. Ralchenko, F. Jou, D. Kelleher, A. Kramida, A. Musgrove, J. Reader, W. Wiese, K. Olsen, NIST atom. spec. database 8 (2008) 96.

[49] I.E. Kieft, D. Darios, A.J. Roks, E. Stoffels, Plasma treatment of mammalian vascular cells: A quantitative description, IEEE Trans. Plasma Sci. 33 (2005) 771.

[50] K.D. Weltmann, E. Kindel, R. Brandenburg, C. Meyer, R. Bussiahn, C. Wilke, T. Von Woedtke, Atmospheric pressure plasma jet for medical therapy: Plasma parameters and risk estimation, Contrib. Plasma Phys. 49 (2009) 631.

[51] Y. Kubota, Spectroscopic analysis of nitrogen atmospheric plasma jet, J. Plasma Fusion Res. 8 (2009) 740.

[52] Y.-H. Choi, J.-H. Kim, K.-H. Paek, W.-T. Ju, Y. Hwang, Characteristics of atmospheric pressure N_2 cold plasma torch using 60-Hz AC power and its application to polymer surface modification, Surf. Coat. Technol. 193 (2005) 319.

[53] T.F. Slater, Biochem. Free radical mechanisms in tissue injury, Nutri. Soc. 222 (1984) 1.

[54] B.C. dickinson, C.J. Chang, Chemistry and biology of reactive oxygen species in signaling or stress responses, Nat. Chem. Biol. 7 (2011) 504.

[55] V. Gamaleev, N. Iwata, M. Hori, M. Hiramatsu, M. Ito, Direct treatment of liquids using low-current arc in ambient air for biomedical applications, Appl. Sci. 9 (2019) 3505.

[56] R.J. Marano, H.J. Wallace, D. Wijeratne, M.W. Fear, H. San Wong, R. O'Handley, Secreted biofilm factors adversely affect cellular wound healing responses in vitro, Sci. Rep. 5 (2015) 13296.

[57] C. Bailey, K. Pemmaraju, M. Phan, A. Radhakrishnan, A. Thomas, Development of nonthermal plasma-assisted hand sanitization, Plasma Med. 4 (2014) 221.

Chapter 7

Spectroscopic Studies on the Biomolecular Recognition of Toluidine Blue: Key Information Towards Development of a Non-contact, Non-invasive Device for Oral Cancer Detection

7.1. Introduction:

Oral cancer is the 11th most common cancer in the world [1] and has secured its place in the top 3 common cancers in India [2]. Oral cancer or oral cavity cancer falls in the category of head and neck cancer which includes the malignancy of the oral cavity, buccal mucosa, tongue, vermilion border of the lip, the floor of the mouth, palate, the gingiva, and also including the salivary glands, tonsils or other lymphoid tissues [3]. But the most common locations are that of the epithelia of the lining of the buccal mucosa and the lateral border of the tongue [4,5]. These types of epithelia present are squamous; hence termed as squamous cell carcinoma. Oral cancer can be developed from the de-novo or malignant transformation of Oral premalignant disorders (OPMD) [6]. Oral cancer, often referred to as "poor man's disease" [7], is triggered by a poor lifestyle and the major independent risk factors for OSCC are tobacco (through smoking and chewing), alcohol, and areca nut use whereas, poor oral hygiene, genetics, malnutrition, oral microbiome are considered as potential risk factors. [8-10]. Some risk factors are known for their etiopathogenic roles in oral cancer such as consumption of tobacco in a different form (chewing or smoking) and alcohol, phenol, viral (HPV, EPV, etc.), bacterial and fungal infections, electro-galvanic

reaction, radiation, genetics, immunosuppression and malnutrition upregulation of oncogene, depression of tumor suppressor genes and chronic irritation from the ill-fitted denture or sharp cuspal edges of the teeth [11,12]. Apart from the confirmed cases of malignancy, there are some cases of malignancy, arise from oral premalignant disorders (OPMD) like leukoplakia, erythroplakia, erythroleukoplakia, oral submucous fibrosis (OSMF) on the buccal mucosa, tongue, and the floor of the mouth, palate, etc. In India and South East Asia malignant transformation of OSF to squamous cell carcinoma (SCC) has been estimated to be between 2% and 8% and malignant transformation rates of oral leukoplakia from 0.13 to 17.5%, and the rates of 5-year cumulative malignant transformation range from 1.2 to 14.5% [13]. If these can be detected through careful visual screening in the early stage where these oral cancers haven't propagated to the lymph node yet, the patient can be treated with a high survival rate [14-16].

Toluidine Blue/Toluidine Blue O/ Basic Blue 17/Tolonium chloride/ Blutene chloride (Molecular Formula: $C_{15}H_{16}C_lN_3S$) is a phenothiazine cationic basic, hence acidophilic dye. By exploiting its metachromatic properties, it is expected to bind to acidic components of the tissues like sulfates, carboxylates, and phosphates. It interacts with macromolecules and provides us with a unique yet simple visual molecular recognition technique by staining nucleic acid and polysaccharides. This compound fulfills the criteria of being a suitably charged stain as it cannot cross the plasma membrane of the cells, thus finding its application in vivo staining. It found its first application in situ detection of cervical cancer in 1963 [17]. Similarly, for the patients, with oral lesions, cysts, or other neoplasms or for the patients with potential malignancy in their aerodigestive tracts, a 1-2% rinse of the Toluidine Blue (TB) dye or an aqueous-based or a weak acid-based application will ensure that the dye only

retains in those malignant or the potentially malignant tissues (and also the non-specific retention of the dye in dead tissues such as on the upper surface of the tongue. The relative staining of the tissues which provides almost a gradient of colors in the bluish-purple range in the localized malignancies is indicative of the presence of the malignancy and gives us a qualitative or a visual idea of the stages of the carcinoma. Since TB is a basic and a cationic dye it will have an affinity towards the negatively charged components of the tissues such as DNA and RNA. The malignant epithelia of the mouth contain more amounts of nucleic acids along with wider intracellular channels which help in an increased penetration and retention of the dye than the non-malignant tissues. Thus, after rinsing off the buccal cavity, only the malignant areas would retain the stain and the non-malignant parts would eject out the bulky stain which won't be able to cross its plasma membranes and interact with the macromolecules [16,18]. Although the TB staining is found to be effective in the screening method for the recommendation for biopsy test to diagnose oral cancer, frequent false-positive and failure of quantitative estimation of the degree of cancer are found to be limitations of the technique. The conventional technique of TB staining of the oral lesion and thereafter visual and colorimetric evaluation for detection of carcinoma is a highly qualitative process largely dependent on the experience of the practitioner and also leads to false positives in many cases.

Despite the widespread developments in medical therapeutic techniques, the survival rate of Oral Squamous Cell Carcinoma (OSCC) in the last 5 years is unchanged globally [19,20]. This can be attributed to delayed diagnosis, owing to the absence of appropriate diagnostic tools for early and quick determination of oral malignancy in human cells. Tissue cell biopsy remains to be conventional for OSCC identification. In recent developments, few optical

light-based imaging devices have been reported and few of them have been made commercially available also [19]. Most of them use autofluorescence or chemo luminance properties of live cells to represent visual gradient between the images of healthy cells and malignant cells. Although these medical advancements have shown great potential, some factors prevent the extensive use of such technology. The problem of relying on colorimetry and the qualitative nature of analysis restricts the existing devices with accuracy and measuring level of malignancy in numerical values. The molecular level identification of interactions of cells with other staining agents also remains questionable.

In our work, we are interested in exploring the basic photochemistry behind the application mentioned above and simultaneously explore the possibility of quantitatively detecting oral cancer via spectroscopic methods exploiting the interaction of TB with DNA. In a recent study, it is shown that the absorption spectrum of TB can be fitted into different bands of six different aggregation species simultaneously present in the sample under investigation [21,22]. The overall TB spectrum may be mainly attributed to the H-type aggregation, although some of the species also show the J-type bands with distinct spectrum bands. The interest is to recheck the evidence of interaction between the dye and the macromolecules such as DNA and protein. Though it has already been reported in the literature with the stress that the dye must interact with the nucleic material of the virtue of its anionic and acidic nature [18], the strong confirmation of whether this dye interacts with protein at different pH is still unrevealed and this area will be focused in our work by exploiting the spectroscopic or absorption properties of the chosen model protein and the dye. The understanding of the pH-dependent interaction of TB will enable us to exploit its character in a direction where we can use it for oral cancer detection. We are also reporting

the development of a prototype for malignant cell detection utilizing the fundamentals of reflection spectroscopy. The prototype has also been shown to be producing significantly accurate data when used in patients for preliminary clinical studies. The prototype has shown the potential to successfully measure malignancy in a small number of human subjects. Although, extensive clinical trials need to be undertaken in the future for the data to be statistically significant. We hope that the toluidine blue staining method which was considered unreliable for its classical dependence on the experience of the practitioner [19], would gain significant importance with its complementary use with "Oral-O-Scope".

7.2. Materials and Methods:

7.2.1. Characterization Techniques:

The absorption measurements were performed with Shimadzu UV-2450 UV-Visible Spectrophotometer. We have used the buffer at various pH to create the baseline for absorbance measurement of the corresponding spectra. All the picosecond resolved fluorescence transients were measured by using commercially available time-correlated single-photon counting (TCSPC) setup with MCP-PMT from Edinburgh instrument, U.K. (instrument response function (IRF) of ~80 ps) using a 409 nm excitation laser source. The details of the time-resolved fluorescence setup are identical to the previously reported article [23-28]. A quartz cuvette of path length 1 cm was used for all the optical measurements. To estimate the Forster resonance energy transfer efficiency of the donor (EtBr) to the acceptor (TB) and hence to determine the donor-acceptor pairs we have followed the previously reported methodology. The donor-acceptor distance (r) can be calculated using Eq. 7.1. where R_0 is the Forster's distance and E is the efficiency of energy transfer. Here, the

efficiency of energy transfer (E) is calculated from the lifetimes of the donor in Here, the efficiency of energy transfer (E) is calculated from the lifetimes of the donor in

$$r^6 = [{R_0}^6(1 - E)/E] \quad (7.1)$$

the absence and presence of acceptors (τ_D and τ_{DA}) using the Eq. 7.2.

$$E = 1 - \frac{\tau_{DA}}{\tau_{DE}} \quad (7.2)$$

7.2.2. Cell Culture:

Human lung carcinoma (A549) cell, human embryonic kidney (HEK293) was purchased from the National center for cell science, Pune, India. Cells were cultured in DMEM media (pH 7.4) supplemented with 10% FBS and antibiotic-antimycotic solution 100× (containing 10,000 units penicillin, 10 mg streptomycin, and 25 µg amphotericin B per mL in 0.9% normal saline). The cell lines were maintained at 37°C in an air-jacketed 5% CO_2 incubator and were routinely passaged.

7.2.3. Toluidine Blue Staining:

All the cells were separately plated at a density of ~100 cells in a 96-well plate. After 24 Hrs incubation, 2 µM TB dye was treated for 30 mins at 37°C. Then the cells were washed with 1x Phosphate Saline Buffer and OD was taken at 640 nm. The same procedure was repeated after the 2nd wash with 1x PBS.

7.2.4. Confocal Microscopy:

A549 cells and Hek cells were seeded on the coverslip and grown in DMEM media. Cells were fixed for 30 min with 4% paraformaldehyde and subjected to confocal microscopic studies. Cells were then incubated with 2 µM toluidine blue for 15 m, washed twice with 1x

PBS and incubated with EtBr for 15 m. After washing in the same procedure, cells were mounted with anti-quenching agent n-propyl gallate for microscopic slide preparation and detected by confocal fluorescence microscope.

7.2.5. Spectrometric Device for Detection of Oral Cancer (Oral-O-Scope):

Reflection spectrometry was used for the development of a device capable of non-invasive and non-contact development of oral cancer cells. This device consists of primarily a light source, a spectrograph, and a lab-grade reflectance probe. A 3 W LED light available in the local market was used to collect light and incident on the cells under test. An appropriate power supply was provided using a 5 Volt AC-DC adapter. The retro-reflected light from the sample was collected and fed to a spectrograph purchased from Pure Engineering, USA.

The optical signals after the successful analysis were passed on to a computer via a microcontroller (Arduino Uno). A self-developed software acquires the necessary information and produces the plot in real-time. A lab-grade diffuse reflectance probe (Ocean Optics, Florida) having six illumination fibers around one acquisition fiber was used to transmit the light from the LED source and to accept the diffuse optical signal from the sample and send the signal to the spectrometer respectively. The schematic of the developed device is shown in Figure 7.1. For the use of the developed device on the human subject, informed consent was obtained from the patients prior to the application of TB and data acquisition. Removal of oral debris was achieved by rinsing with water for 30 sec. This was followed by a 1% acetic acid rinse for 20 sec. Finally, the oral cavity was rinsed with (1%W/W) TB for a full 30 sec. The mechanically retained TB stain was eliminated using a 1% acetic acid rinse for 20 sec [26-28]. The clinical study was carried out in 20 patients

after obtaining ethical clearance (ADCH/OP-513/16-11/906) issued by 'The Ethical

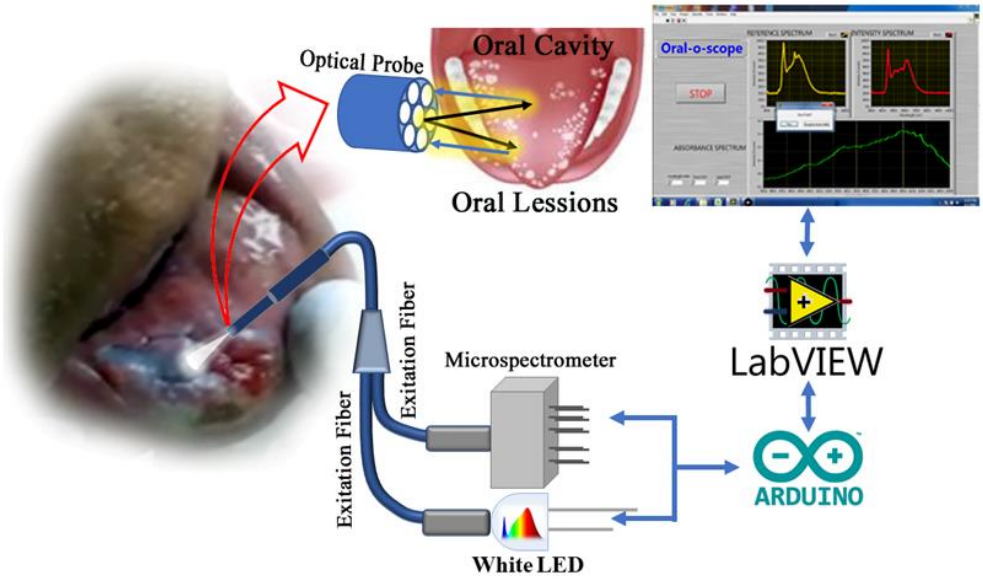

Figure 7.1: *Schematic diagram of the components in the Oral-O-Scope. Light from a 3 W LED source is allowed to incident in the Toluidine Blue (TB) stained oral lesion and collect the diffused reflected light through a 6:1 fiber optic bundle to a micro spectrometer mounted on a Arduino platform. The spectroscopic signal is analyzed through a self-developed LabVIEW based software.*

Committee', Awadh Dental College & Hospital, Jamshedpur, India. All methods in this study were carried out strictly following guidelines and regulations set by the ethical committee.

7.2.6. Software of the Device:

A GUI based software was developed to acquire signals and plot them in real-time and quickly arrive at the decision of screening the patient. The computer connects to the developed device via a USB and listens to the interface for incoming data. The acquired data will be an array of the intensity values at various wavelengths after necessary calibration. The calibration constant was provided by the manufacturer. The software developed in the LabVIEW platform is simple, intuitive, and needs no trained manpower to operate.

7.2.7. Work Flow:

The working principle of the developed instrument Oral-O-Scope has been demonstrated in Figure 7.2. After initiation of the GUI, it performs its "homework" about the availability and health of the connected equipment. After the successful establishment of the link to the

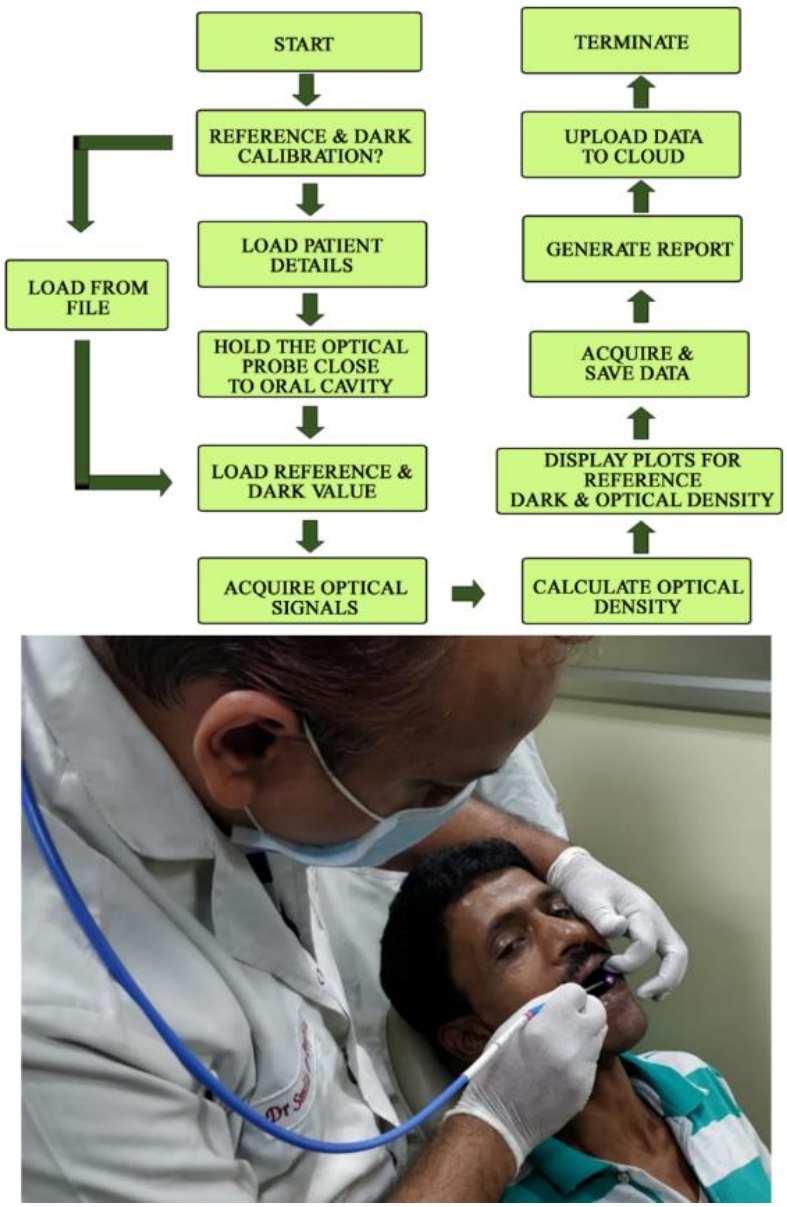

Figure 7.2: *The work flow of the developed Oral-O-Scope is shown in panel (a). Panel (b) shows actual procedure of using the device by a dentist on a human subject. Live details are shown in a supplementary video (Informed consent from all human subjects and participants to publish their respective photo/video in an open access journal was obtained).*

instrument, the software asks the user to perform a reference and dark value determination procedure. This is a very important step to arrive at the optical density guided by Beer-Lambert law. The reference and dark values can also be a preloaded set of values stored on the hard drive as text files or can be instantaneously provided. The users are then provided with the live intensity (pixel counts) window, stored values for reference intensity, and the Optical density window. The reflectance probe is held close to the oral cavity of the patient. The light incident (400-900 nm) on the tissue of the oral cavity illuminates the lesion under test and the retro-reflected is collected by the center fiber and is taken to the spectrograph. All obtained graphs were fitted with multiple Gaussian peaks to evaluate the individual contribution of each component in the plot. The process of fitting was followed according to one of our earlier work [29]. Each component of the graph corresponds to a certain form of molecular TB or some tissue spectroscopic signature. It was observed that the spectra obtained from malignant lesions showed a distinctly different pattern than the normal cells. Multiple sets of data were acquired and averaged to produce a steady trace free from errors that may arise from hand or subject shaking during the time of data acquisition. The software automatically decides to acquire the valid coming from the muscle and ignores any spurious signal.

7.3. Results and Discussion:

Although the cationic dye TB is being used as a screening stain for the diagnosis of oral cancer for a long time [30], a systematic study on the interaction of the dye with biological macromolecules is sparse in the literature. In a molecular simulation study followed by X-ray crystallographic investigation, it is shown that TB in solution may remain in six different aggregated forms [21,22]. We have observed that the aggregation behavior of the dye TB

depends on the biological macromolecules and their conformation. Figure 7.3(a) shows the absorption spectrum of TB in water and human serum albumin (HSA protein at pH 7). Even

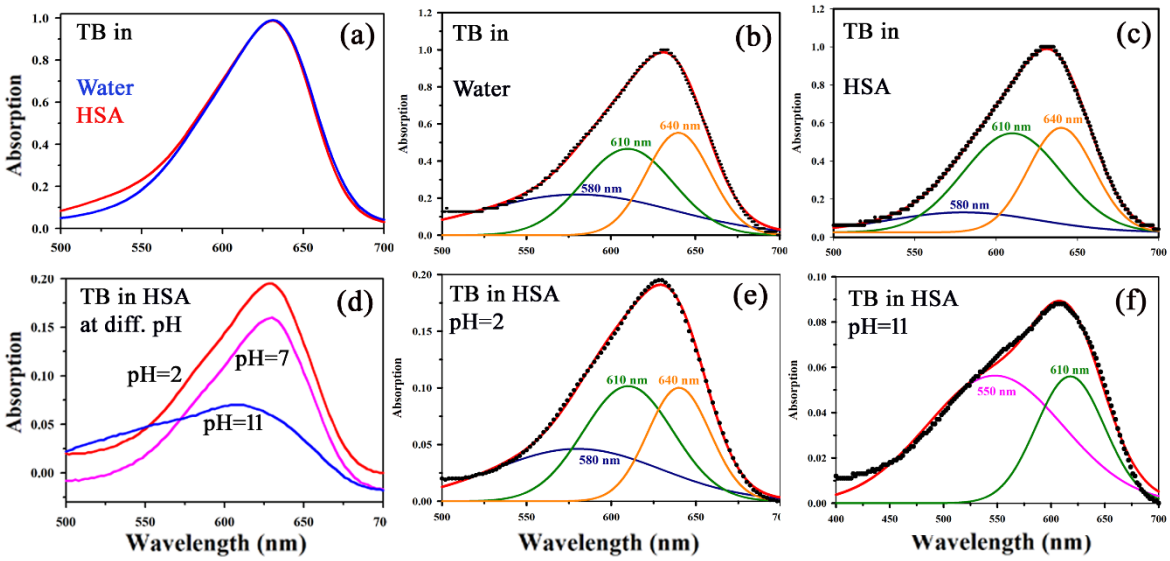

Figure 7.3: *(a) Absorption spectra showing the interaction of TB with HSA in a ratio (1:1) in water. (b) Deconvoluted spectrum of TB in water (c) Deconvoluted spectrum of TB in complexation with HAS (in a ratio of 1:1) showing the presence of monomer (610 nm) along with the dimeric form (580 nm and 640 nm). (d).Steady state absorption spectra of TB in presence of HSA in a ratio of 1:1 at pH 2, 7 and 11 (e) The deconvoluted spectrum of TB in complexation with HSA (in a ratio of 1:1) at pH 2 (f) The deconvoluted spectrum of TB in complexation with HSA (in a ratio of 1:1) at pH 11.*

with a higher concentration of HSA (1:100) no observable change in the TB spectra was noticed. Spectral deconvolution of TB in water is shown in the Figure 7.3(b); presence of monomer (610 nm) along with some dimer (580 nm and 640 nm) are evident. Figure 7.3(c) shows minor but distinct difference of TB deconvoluted spectrum in HSA at pH 7 compared to that in water. The absorption spectral characteristics of TB in HSA solution at various pH conditions are shown in Figure 7.3(d). While deconvoluted spectrum of TB-HSA in pH 2 Figure 7.3(e) is consistent with that of pH 7 (Figure 7.3(c)), the spectrum at pH 11 Figure 7.3(f) is distinctly different as the protein undergoes structural denaturation revealing the unprecedented absence of dimeric form (580 nm and 640 nm) rather indicate the presence of trimeric species (550 nm).

As high pH conditions are rare in biological systems [31] and it is almost impossible to achieve in oral cavities this study gives us the basis for using the dye as an oral cancer detection probe. As the pH condition in cancer cells are deregulated and lowered, TB will not be able to bind with protein in cancer cells in normal circumstances. However, denatured protein is shown to have a binding affinity, which may have some physiological significance. For example, it was observed that filiform papillae, when exposed to the toluidine blue, always retain the dye. Although the mechanism was not clear, it might be related to a high protein-synthesis rate [32]. In a recent study, it is also reported the presence of denatured sensory proteins in the filiform papillae [33]. Figure 7.4(a) shows the absorption spectrum of TB in Genomic DNA (from Calf Thymus). The spectrum of TB in water is also shown for comparison. An apparent shift in the TB-DNA spectrum compared to that in water is evident. The absorption peak of TB in water is at 630 nm which is shifted to 640 nm on binding to calf thymus DNA. In Figure 7.4(b), the absorption spectra show the binding between TB and calf thymus DNA with an absorption maximum at 636 nm. Figure 7.4(b) shows a deconvoluted spectrum of TB-DNA, where the presence of a monomeric form of TB (610 nm) along with dimeric form is evident (580 nm, 640 nm). This establishes that DNA interacts with the dye in a specific manner consistent with reported literature [34] and offers the opportunity to exploit the property to identify malignant cells using the spectroscopic technique. As malignant cells have more amount of nucleic acid as it is highly proliferating, therefore, the cells are expected to be strongly stained with TB [32]. In order to study the specific molecular recognition of TB by the genomic DNA, we have performed the FRET studies to investigate the energy transfer from EtBr (a known intercalary dye for DNA) to TB in the condensate. Figure 7.5(a) shows the

emission spectra of EtBr overlaps with the absorption spectrum of TB. The fluorescence

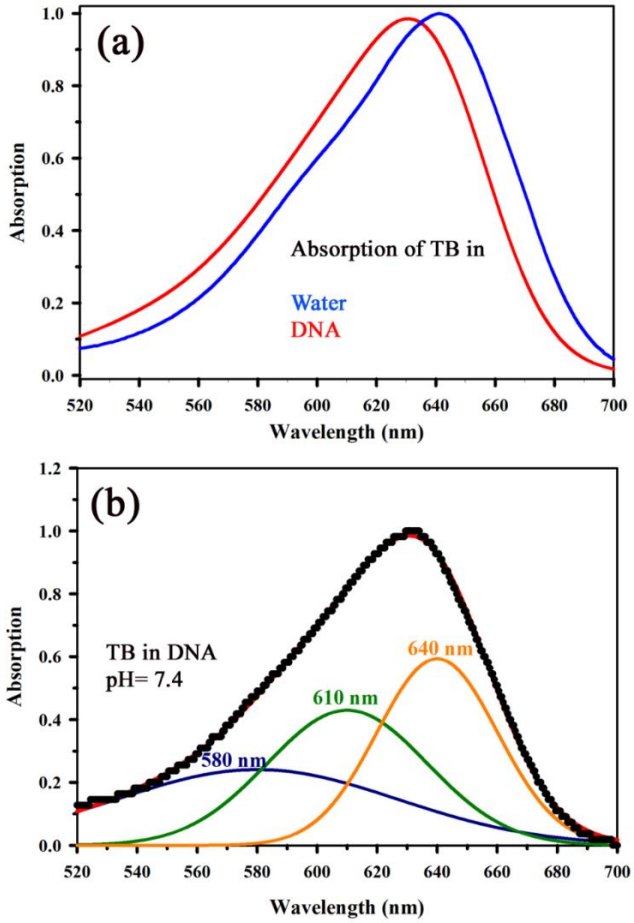

Figure 7.4: *(a) Absorption spectrum showing the interaction of Toluidine Blue (TB) with Genomic DNA (from Calf Thymus) (in a ratio of 1:1) along with the spectrum of TB in water has also been shown for comparative analysis of TB in water and in complexation with DNA.(b) shows deconvoluted spectrum of TB complexed with DNA, where the signature of monomeric form of TB (610 nm) along with the dimeric forms are visible (580 nm, 640 nm).*

transient of EtBr is quenched in presence of TB as shown in Figure 7.5(b). The efficiency of energy transfer in the above system is found to be 45% from the temporal fluorescence decay as shown in Figure 7.5(c). The distance between the donor and acceptor was calculated to be 36 Angstrom. Thus, the experimental finding indicates that EtBr and TB can be intercalated simultaneously maintaining a distance of about 10 base pairs [21]. It has to be noted that, a higher concentration in TB compromises the structural integrity of the DNA and eventually the DNA-TB complex precipitates. These results help us to conclude

that TB and EtBr both bind the DNA. Hence, TB stain can be a potential marker for an increase in nuclear materials which is the characteristic of malignant cells. After conducting

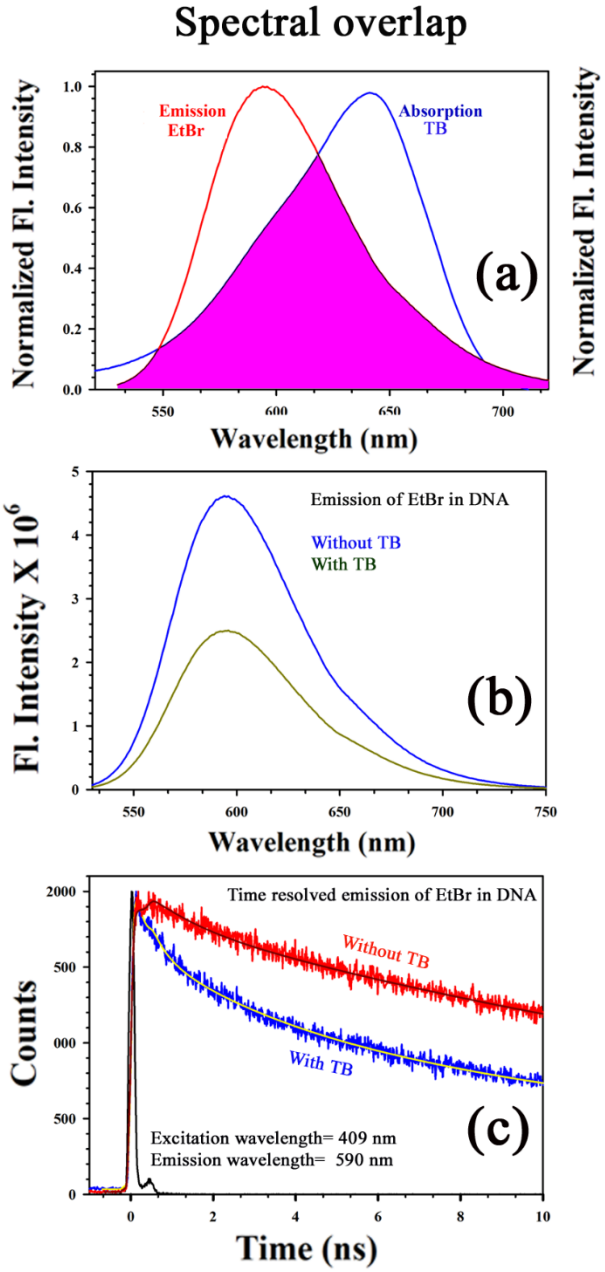

Figure 7.5: *(a) Steady state emission spectra of EtBr and absorption spectra of TB are shown. An overlapping zone between the emission of EtBr and TB has been indicated as the pink shaded zone. (b)Steady state emission spectra of EtBr (donor) in absence and presence of the acceptor molecule (TB) (c) The picosecond resolved fluorescence transients of the donor (EtBr) in absence and presence of the acceptor (TB) are shown.*

the biophysical study on the specific interaction of TB with DNA, we further investigated the effect of TB on cell lines. As our ultimate goal was to evaluate the specificity of TB in

staining of oral cancer cells, we choose epithelial cells for ex vivo evaluation. For our experiment, we have selected human embryonic kidney (HEK 293) cell line as control and A549 lung cancer cell lines as malignant cells (Figure 7.6).

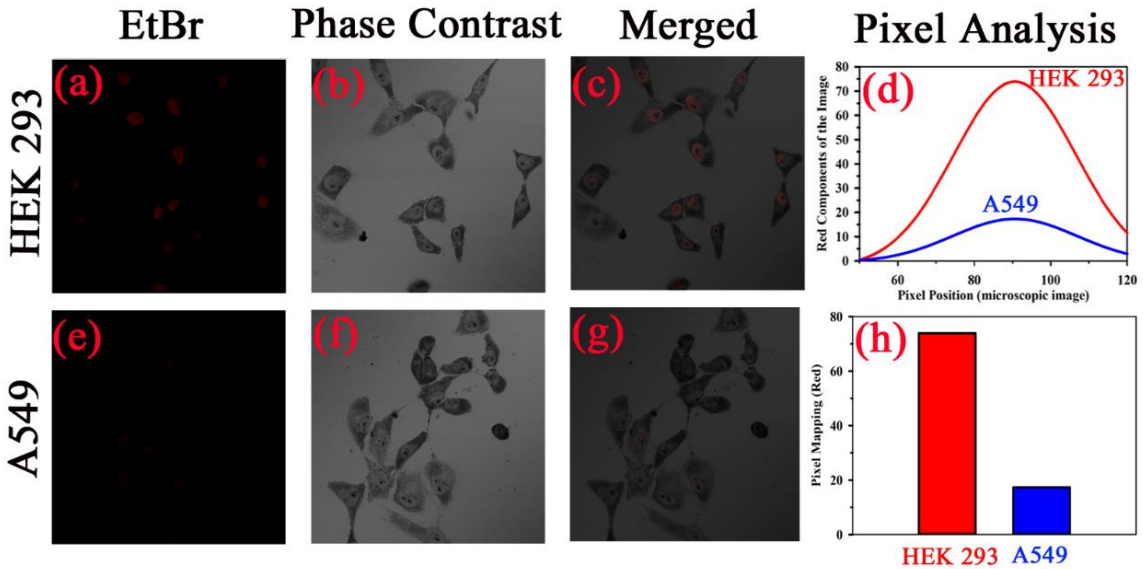

Figure 7.6: *Specific localization of TB in nucleus of malignant cells resulting into the increased FRET efficiency with EtBr. Phase contrast microscopic image human embryonic kidney (HEK293) cells and lung cancer cell (A549) is shown in in the panel (b) and (f) respectively. The fluorescence images of the cell lines with Ethidium bromide (EtBr) labelling in absence and presence of toluidine blue (TB) are shown in the panels (a) and (e) respectively. The fluorescence quenching of the EtBr-stained nucleus in presence of TB is evident. Panels (c) and (g) shows the merged image. A quantitative estimation from red component in the nucleus images from RGB analysis is shown in the panel (d). Panel (h) shows the fluorescence intensity of EtBr after TB staining in both cells as per RGB analysis.*

A phase-contrast microscopic image of HEK and lung cancer cell lines (A549) is shown in Figure 7.6(b) and (f). The fluorescence images of the HEK and A549 cell lines with Ethidium bromide (EtBr) labeling are shown in Figure 7.6(a) and (e). A quantitative estimation from a red component in the nucleus images from RGB analysis is shown in Figure 7.6(d). A marked decrease in the red fluorescence of EtBr is observed which indicates increased localization of TB in malignant cells and thus a higher amount of quenching of EtBr emission. The authors would like to point out that the focus of this study

was to examine the co-localization of TB and EtBr in the nucleus of the cell. A FRET between EtBr and TB dictates they are near each other. This further strengthens our proposition of TB being a predominant staining agent specific for malignant cells. Figure 7.7(a) depicts the photographic image of a 96-well plate containing either normal HEK 293 cells or A549 cells with TB staining of different concentrations, Only tissue with a confirmed case of malignancy were chosen to perform experiments in the laboratory as permitted by the ethical committee. The arrangement of spectroscopic investigation and

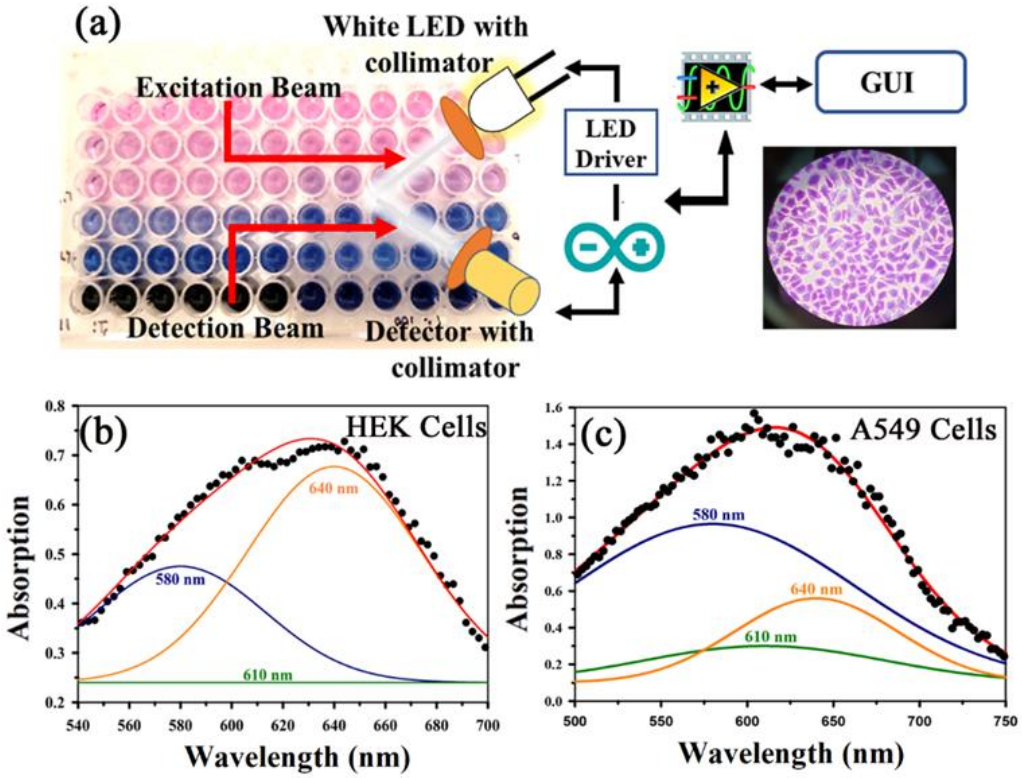

Figure 7.7: *(a) A representative photographic image of 96 well plate containing either normal embryonic kidney (HEK) cell or lung cancer (A549) cell lines with TB staining of different concentrations is shown. The arrangement of spectroscopic investigation and microscopic image of TB stained A549 cell lines is also shown. Deconvoluted TB absorption spectra for HEK and A549 are shown in (b) and (c) panels. Note that Monomeric TB form (610 nm) is only present in the cancer cell lines in contrast to its normal counterpart.*

microscopic image of TB stained A549 cell lines is also shown. Deconvoluted TB absorption spectra for HEK 293 and A549 are shown in (b) and (c) panels of Figure 7.7.

Note that Monomeric TB form (610 nm) is only present in the cancer cell lines in contrast

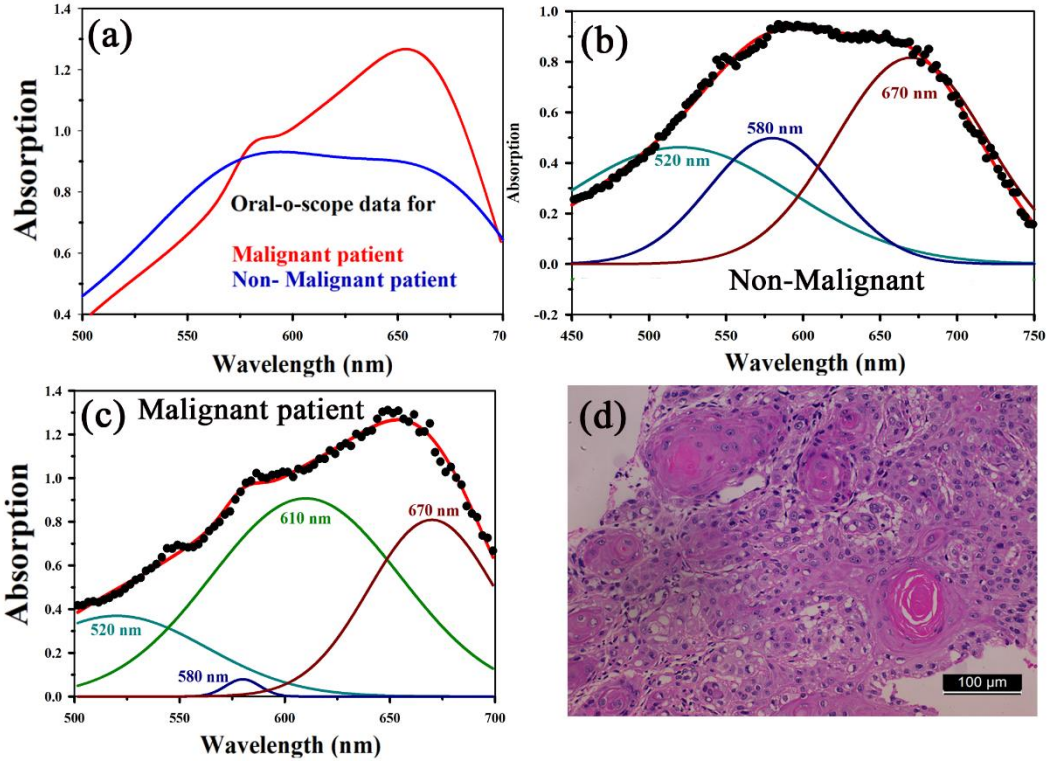

Figure 7.8: *(a) Absorption spectra acquired through "Oral-O-Scope" during a clinical trial on malignant and non-malignant human subjects. The spectral deconvolution as shown in panels (b) and (c) clearly reveals absence of monomeric form of TB (610 nm) in non-malignant lesion (b) compared to that in malignant lesion (c). The presence of monomeric TB associated with tetrameric forms (520 nm, 580 nm and 670) is distinctly evident in the malignant tissue. Corresponding confirmatory biopsy (histopathological slide) image of the TB-stained tissue from the malignant subject is shown in panel (d).*

to its normal counterpart. The experimental observation clearly depicts that presence of 610 nm spectral line may be accompanied by dimeric or trimeric TB species is indicative of malignant cell. These forms of TB can be characterized by the individual contribution of deconvoluted peaks in amplitude and width (area under the curve) obtained from the acquired data. Figure 7.8(a) shows absorption spectra acquired through our developed "Oral-O-Scope" in a clinical trial on malignant and non-malignant human subjects. It was found that the instrument was able to produce repeatable data under the clinical setting. The spectral deconvolution as shown in Figure 7.8(b) and (c) of Figure 7.8 reveals the absence

of a monomeric form of TB (610 nm) in non-malignant lesion Figure 7.8(b) compared to that in malignant lesion Figure 7.8(c). The presence of monomeric TB associated with tetrameric forms (520 nm, 580 nm, and 670) is distinctly evident in the malignant tissue. Corresponding confirmatory biopsy (histopathological slide) image of the TB-stained tissue from the malignant subject is shown in Figure 7.8(d). The provisional diagnosis suggested a solitary bit of soft tissue from the left buccal mucosa. Histopathological evaluation revealed hyperplastic squamous epithelium with the intact basement membrane. However, at one place an invasion of islands of the dysplastic epithelium with cellular changes and nuclear hyper-chromatism were observed along with few keratin pearl formations and one or two abnormal mitoses. The high power field of the microscope shows highly cellular and vascular tissue stroma as shown in Figure 7.8(d).

This is suggestive of 'well-differentiated' squamous cell carcinoma. We have also explored the possibility of detection of overstaining of the oral lesion, which often led to "false-positive" in the visual interpretation of TB-staining [32,35,36]. Figure 7.9(a) shows absorption spectra acquired through Oral-O-Scope in a clinical trial on the malignant and over-stained non-malignant human oral lesion. The corresponding deconvoluted spectra are shown in Figure 7.9(b) and (c). Note the remarkable absence of a monomeric form of TB in the nonmalignant overstained lesion. The understating of oral tissue is found to be detected by our developed Oral-O-Scope. Figure 7.10 shows absorption spectra acquired through Oral-O-Scope in a clinical trial on an under-stained non-malignant human oral lesion. Note the absence of monomeric TB form (610 nm) and presence of tissue information represented by 546 nm and 576 nm which are the signature of oxygenated hemoglobin [37]. Table 7.1 summarizes the individual contributions of all the deconvoluted peaks in percentage for all

the acquired data in this work. We have tested our device with various forms of

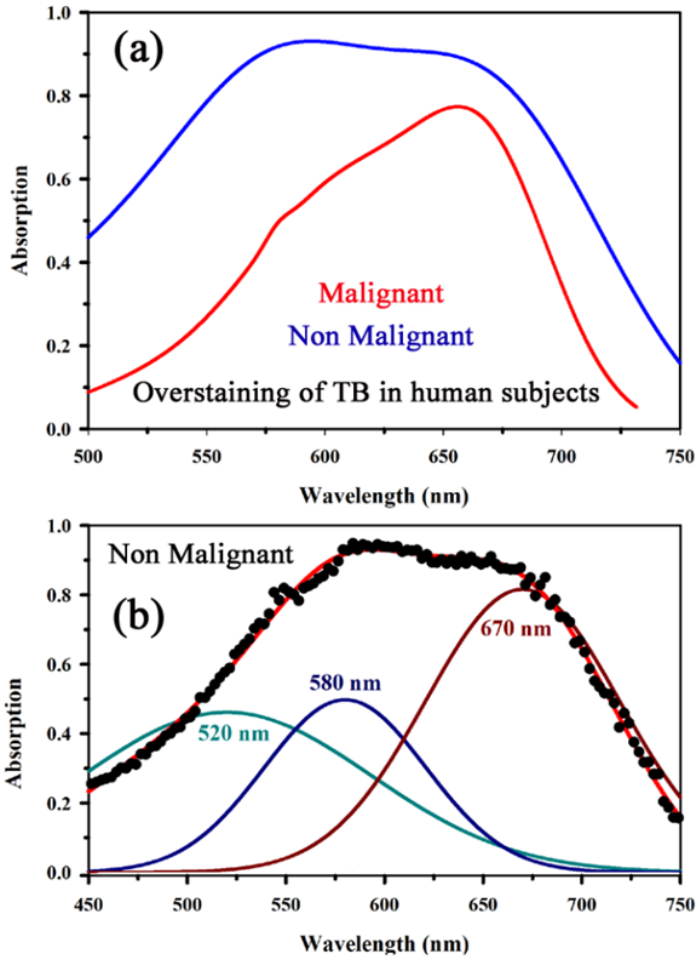

Figure 7.9: *Absorption spectra obtained through Oral-O-Scope during a clinical trial on malignant and over-stained non-malignant human oral lesion are shown in the panel (a). The deconvoluted spectra obtained from the fitted curve of over-stained non-malignant lesion are shown in the panels (b). The remarkable absence of monomeric form of TB evident by 610 nm in the nonmalignant overstained lesion is clearly visible.*

inflammations and traumatic ulcers only to find no presence of a monomeric form of TB (610 nm) indicating non-malignancy in the tissue. The proposed device showed promising potentiality to determine the molecular existence of various forms of TB interactions with DNA. The competitive market analysis and scientific literature showed the existence of few light-based devices which rely primarily on imaging and produce qualitative analysis and hence are only useful as a screening tool. Oral-O-Scope on the other hand uses absorption

spectroscopy and subsequent deconvolution of obtained peaks to ascertain the presence of TB in various forms.

***Table 7.1**: Weightage of the deconvoluted spectra of TB sample in various conditions.*

Sample (TB in)	Spectral Contributions (%)								Forms of TB
	520 nm	546 nm	550 nm	576 nm	580 nm	610 nm	640 nm	670 nm	
Water	-	-	-		32.6	33.05	34.3	-	Monomer+ Dimer
Protein (HSA), pH=7	-	-	-		15.3	49.67	35.01	-	Monomer+ Dimer
Protein (HSA), pH=2	-	-	-		33.6	39.4	26.96	-	Monomer+ Dimer
Protein (HSA), pH=11	-		66.8		-	33.2	-	-	Monomer+ Trimer
TB-DNA pH 7.4	-	-	-		26.5	43.51	30.13	-	Monomer+ Dimer
Normal cell (HEK)	-	-	-		34.4	0	65.61	-	Dimer
Lung cancer cell (A549)	-	-	-		66.3	13.15	20.50	-	Monomer+ Dimer
Non-malignant oral lesion	36.2	-	-		21.9	0	-	42.95	Tetramer only
Malignant oral lesion	19.4	-	-		0.78	49.9	-	29.87	Tetramer+ Monomer
Overstained malignant oral lesion	7.06	-	-		0.24	58.54	-	34.14	Tetramer+ Monomer
Under-stained non-malignant oral lesion	-	8.18	-	2.8	48.2	-	-	40.84	Oxygenated Hemoglobin+Tetramer

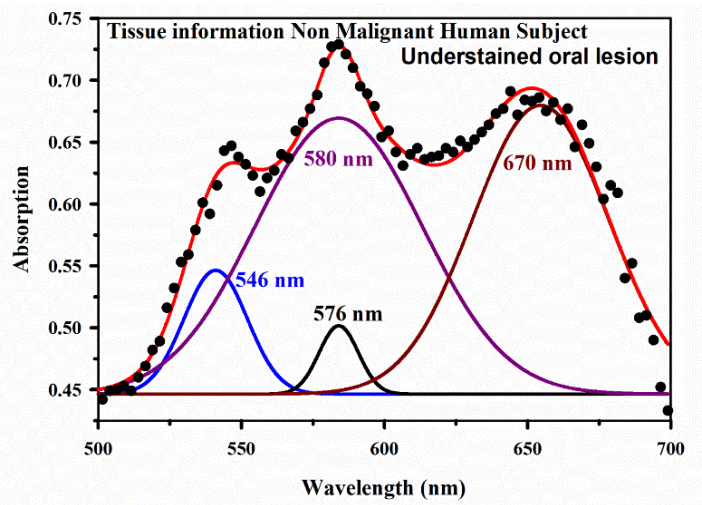

***Figure 7.10:** Absorption spectra obtained through Oral-O-Scope during a clinical trial on an under-stained non-malignant human oral lesion. The absence of monomeric TB form (610 nm) and presence of tissue information indicated by 546 nm and 576 nm which are the spectroscopic signature of oxygenated hemoglobin (see text) is clearly visible.*

Table 7.2: *Comparison of commercially available devices with Oral-O-Scope. It is evident that Quantitative representation and quick determination of the Lesion type gives Oral-O-Scope" distinct advantage over the others.*

Device	**Vizilite & Vizilite Plus**	**Velscope**	**Identafi**	**Microlux/ DLTM**	**Oral-O-Scope**
Measurement Principle	Chemilumines-cence Imaging	Autofluorescence Imaging	Fluorescence Imaging	Chem-iluminescence Imaging	Absorption Spectroscopy
Type of Lesion	PMD, OSCC, OL	PMD, OSCC	OSCC	OSCC	PMD, OSCC, OL
Analysis Type	Qualitative	Qualitative	Qualitative	Qualitative	Quantitative
Screening/Dia gnostic	Screening	Screening	Screening	Screening	Diagnostic
Sensitivity	Low	High	Low	High	High
Specificity	Low	High	High	Low	High
Molecular Identification	No	No	No	No	Yes

Table 7.2 represents a comparative representation of the commercially available devices vis-à-vis Oral-O-Scope in terms of various measurement parameters. The commercially available instruments available in the open market are dependent largely on imaging (Chemiluminescence, Autofluorescence, and Fluorescence) of tissues which provide no insight on the variety of forms of the presence of TB in tissues. Oral-O-Scope, on the contrary measures data and analyses the presence of TB in various forms confirmed by their spectroscopic signatures using reflectance spectroscopy.

7.4. Conclusion:

The present work is to study the molecular interactions of a cationic dye Toluidine Blue (TB) with protein and DNA to understand the efficacy of the dye for the diagnosis of oral cancer in human subjects. While protein (HSA) is found to be almost noninteracting with the dye TB in physiological conditions, genomic DNA shows affinity toward the dye in a similar experimental condition, which could be the key for labeling malignant cells containing more nucleic material in the cytosol. We have shown the existence of a

monomeric form of TB dye (absorption peak at 610 nm) in DNA associated with some dimeric form of the dye. The FRET studies also confirmed the strong interaction of TB with genomic DNA at the molecular level. In ex-in-vivo studies on normal (HEK) and cancer (A549), cell lines reveal consistent observation in the line of the in vitro studies on TB with genomic DNA. While cancer cells can retain TB in monomeric form (610 nm) along with some percentages of the dimer, normal can only hold the aggregated form of the dye. Our further studies on the clinical trial also confirm that the existence of monomeric TB in the cancer lesion with some aggregated form can be used to identify malignancy in the oral lesion. This contrasts with a visual or colorimetric method of evaluation where the difference of inflammation-induced atypia with tobacco-induced malignancy is not clear. The molecular-level diagnosis by Oral-O-Scope enables us to understand the interaction of TB with proliferated DNA which is absent in any inflammation-induced atypia. We have also identified over staining leading to conventional false positive in the visual examination based on dye aggregation behavior in the oral tissue. We are confident that the device and the methodology (spectral deconvolution) used in the report can also use useful for the class and degree of the malignancy of the oral lesion through a large-scale clinical trial, which is underway in our group.

As a pilot study, the sample size is appropriate for ascertaining the functioning of the instrument and the probe molecule. A larger clinical validation with a higher number of patients will be performed in the future. The degree of malignancy is a promising possibility through Oral-O-Scope by application of various statistical models over the collected data in significant numbers as the initial data proves the efficacy of the device in converting malignancy cells in numerical numbers.

References

[1] R. Sankaranarayanan, K. Ramadas, H. Amarasinghe, S. Subramanian, N. Johnson, Oral cancer: Prevention, early detection, and treatment, Dis. Contr. Prior. 3 (2015) 85.

[2] K.R. Coelho, Challenges of the oral cancer burden in India, J. Cancer Epidemiol. 2012 (2012) 1.

[3] E.E. Vokes, R.R. Weichselbaum, S.M. Lippman, W.K. Hong, Head and neck cancer, N. Engl. J. Med. 328 (1993) 184.

[4] C. Moore, D. Catlin, Anatomic origins and locations of oral cancer, Am. J. Surg. 114 (1967) 510.

[5] J. Bagan, G. Sarrion, Y. Jimenez, Oral cancer: Clinical features, Oral. Oncol. 46 (2010) 414.

[6] S.C. Sarode, G.S. Sarode, J.V. Tupkari, Oral potentially malignant disorders: A proposal for terminology and definition with review of literature, J. Oral Maxillofac. Pathol.18 (2014) S77.

[7] H.D. Sgan-Cohen, J. Mann, Health, oral health and poverty, J. Am. Dent. Assoc. 138 (2007) 1437.

[8] W.J. Blot, J.K. McLaughlin, D.M. Winn, D.F. Austin, R.S. Greenberg, S. Preston-Martin, L. Bernstein, J.B. Schoenberg, A. Stemhagen, J.F. Fraumeni, Smoking and drinking in relation to oral and pharyngeal cancer, Cancer Res. 48 (1988) 3282.

[9] P. Balaram, H. Sridhar, T. Rajkumar, S. Vaccarella, R. Herrero, A. Nandakumar, K. Ravichandran, K. Ramdas, R. Sankaranarayanan, V. Gajalakshmi, The influence of smoking, drinking, paan-chewing and oral hygiene, Int. J. Cancer 98 (2002) 440.

[10] N.W. Johnson, S. Warnakulasuriya, P. Gupta, E. Dimba, M. Chindia, E. Otoh, R. Sankaranarayanan, J. Califano, L. Kowalski, Global oral health inequalities in incidence and outcomes for oral cancer: Causes and solutions, Adv. Dent. Res. 23 (2011) 237.

[11] H. Mortazavi, M. Baharvand, M. Mehdipour, Oral potentially malignant disorders: An overview of more than 20 entities, J. Dent. Res. Dent. Clin. Dent. Prospects 8 (2014) 6.

[12] A. George, B. Sreenivasan, S. Sunil, S.S. Varghese, J. Thomas, D. Gopakumar, V. Mani, Potentially malignant disorders of oral cavity, Oral Maxillofac. Pathol. J. 2 (2011) 95.

[13] T. Amagasa, M. Yamashiro, H. Ishikawa, Oral leukoplakia related to malignant transformation, Oral Sci. Int. 3 (2006) 45.

[14] J.W. Werning, Oral Cancer: Diagnosis, Management Rehab. 16 (2007).

[15] B.W. Neville, T.A. Day, Oral cancer and precancerous lesions, CA Cancer J. Clin. 52 (2002) 195.

[16] G. Sridharan, A.A. Shankar, Toluidine blue: A review of its chemistry and clinical utility, J. Oral Maxillofac. Pathol. 16 (2012) 251.

[17] D.P. Shedd, P.B. Hukill, S. Bahn, In vivo staining properties of oral cancer, Am. J. Surg. 110 (1965) 631.

[18] J. Wang, Y. Guo, B. Liu, C. Cheng, Z. Wang, G. Han, J. Gao, X. Zhang, Spectroscopic analyses on interaction of bovine serum albumin (BSA) with toluidine blue (TB) and its sonodynamic damage under ultrasonic irradiation, J. Lumin. 131 (2011) 231.

[19] M. Mascitti, G. Orsini, V. Tosco, R. Monterubbianesi, A. Balercia, A. Putignano, M. Procaccini, A. Santarelli, An overview on current non-invasive diagnostic devices in oral oncology, Front. Physiol. 9 (2018) 1510.

[20] E. Omar, Future imaging alternatives: The clinical non-invasive modalities in diagnosis of oral squamous cell carcinoma (OSCC), Open Dent. J. 9 (2015) 311.

[21] R. Matassa, C. Sadun, L. D'Ilario, A. Martinelli, R. Caminiti, Supramolecular organization of toluidine blue dye in solid amorphous phases, J. Phys. Chem. B 111 (2007) 1994.

[22] L. D'Ilario, A. Martinelli, Toluidine blue: Aggregation properties and structural aspects, Model Simul. Mat. Sci. 14 (2006) 581.

[23] T.H. Haines, N.A. Dencher, Cardiolipin: A proton trap for oxidative phosphorylation, FEBS Lett. 528 (2002) 35.

[24] R. Sarkar, S.K. Pal, Ligand-DNA interaction in a nanocage of reverse micelle, Biopolymers 83 (2006) 675.

[25] D. Banerjee, P.K. Verma, S.K. Pal, Temperature-dependent femtosecond-resolved hydration dynamics of water in aqueous guanidinium hydrochloride solution, Photochem. Photobiol. Sci. 8 (2009) 1441.

[26] S. Patel, A. Datta, Fluorescence investigation of the binding of model PDT drugs to nonionic and zwitterionic surfactants, J Photochem. Photobiol. A: Chem. 85 (2009) 725.

[27] P.K. Verma, R.K. Mitra, S.K. Pal, A molecular picture of diffusion controlled reaction: Role of microviscosity and hydration on hydrolysis of benzoyl chloride at a polymer hydration region. Langmuir, Langmuir 25 (2009) 11336.

[28] S. Choudhury, S. Batabyal, T. Mondol, D. Sao, P. Lemmens, S.K. Pal, Ultrafast dynamics of solvation and charge transfer in a DNA-based biomaterial, Chem. Asian J. 9 (2014) 1395.

[29] A. Halder, M. Banerjee, S. Singh, A. Adhikari, P.K. Sarkar, A.M. Bhattacharya, P. Chakrabarti, D. Bhattacharyya, A.K. Mallick, S.K. Pal, A novel whole spectrum-based non-invasive screening device for neonatal hyperbilirubinemia, IEEE J. Biomed. Health Inform. 23 (2019) 2347.

[30] A. Mashberg, Final evaluation of tolonium chloride rinse for screening of high-risk patients with asymptomatic squamous carcinoma, J. Am. Dent. Assoc. 106 (1983) 319.

[31] S. Baliga, S. Muglikar, R. Kale, Salivary pH: A diagnostic biomarker, J. Indian Soc. Periodontol. 17 (2013) 461.

[32] S. Silverman Jr, C. Migliorati, J. Barbosa, Toluidine blue staining in the detection of oral precancerous and malignant lesions, Oral Surg. Oral Med. Oral Pathol. Oral Radiol. 57 (1984) 379.

[33] M. Behrens, S. Born, U. Redel, N. Voigt, V. Schuh, J.-D. Raguse, W. Meyerhof, Immunohistochemical detection of TAS2R38 protein in human taste cells, PLoS One 7 (2012) e40304.

[34] A. Miura, Y. Ohba, Structure of nucleohistone. III. Interaction with toluidine blue, Biochim.Biophys. Acta 145 (1967) 436.

[35] M.W. Lingen, J.R. Kalmar, T. Karrison, P.M. Speight, Critical evaluation of diagnostic aids for the detection of oral cancer, Oral Oncol. 44 (2008) 10.

[36] S. Hageman, R. Van Der Weijden, A. Stams, P. Van Cappellen, C. Buisman, Microbial selenium sulfide reduction for selenium recovery from wastewater, J. Hazard. Mater. 329 (2017) 110.

[37] A. Halder, P.K. Sarkar, P. Pal, S. Chakrabarti, P. Chakrabarti, D. Bhattacharyya, R. Chakraborty, S.K. Pal, Digital camera-based spectrometry for the development of point-of-care anemia detection on ultra-low volume whole blood sample, IEEE Sens. J. 17 (2017) 7149.

Chapter 8

An Optical Scattering-based Cost-effective Approach Towards Quantitative Assessment of Turbidity and Particle Size Estimation in Drinking Water Using Image Analysis

8.1. Introduction:

Increasing environmental pollution is a matter of grave concern in modern society [1]. Pollution extends from air, sound, and water [2,3]. Among these, water pollution has shown a significant increase with the growing population index particularly in Low and Middle-Income Countries (LMIC) [4,5]. A worldwide minimum of 2 billion people consumes water for drinking, contaminated with faecal matter [6]. Contaminated water is the root cause of deadly diseases such as diarrhea, cholera, dysentery as well as typhoid, and its consumption results in 502,000 diarrheal deaths annually [6,7]. These data indicate the urgent need for quantitative assessment of water quality including lakes [8] and bigger water bodies with the online determination of results indicating the readiness of consumption of available drinking water. Water quality is determined by its chemical, physical, and biological content [9-11]. The assessment is mainly a manual process and conventionally it is done by the collection of water samples and using chemical and other methods of analysis [12]. The processes are complex, suitable only for a trained person [13]. Moreover, they are time-consuming and offline [14]. With the advent and development of sensor-based systems, substantial research has been carried out to automate and real-time monitor the water quality, and Internet of

Things (IoT) enable devices are in demand for immediate intimation of human action needed anywhere [15]. Such sensor-based systems mainly focus on the total dissolved solvents (TDS) and pH properties of water and few such sensors have been made commercially available also. While online sensors ensure immediate data availability and trigger the need for urgent action, their calibration, reliability, and water-induced stains become an important concern [16]. Some alternate experimental methods were also tried by researchers like using the bioscreen microbiological growth analyzer [17] and underwater imaging systems [18,19].

Various methods of probing water quality have been tried and researched by various scientists [20]. The contemporary research in this direction includes the measurement of ocean watercolor and estimation of its effect on marine biology [21,22]. RGB analysis has been used to determine the salinity index of water by using the ratio of R to B and B to G was used to determine the chlorophyll content of water [23]. Airborne digital image photography has also been used to map water pollution and overcome the problem of cloud cover scenes [24]. Recently, computer vision and artificial intelligence have witnessed their application in the measurement of water turbidity and related parameters [25]. Various methods of estimation of coliforms in drinking water have been tried as a measure to estimate water quality [26]. In our present study, we have used image analysis of a Red and a Blue dot on an optically lit cast screen across a model turbid medium to estimate the optical density (turbidity) and computational analysis of the captured image-edge blurring phenomena to conclude on the diameter of dominant suspended particulate matter in the turbid colloidal solution. We have also explored the possibility of using a submersible camera to acquire data for long term data acquisition of a natural water body. Data acquired

remotely has been analyzed in our indigenously developed software for online monitoring. The proposed set-up finally produces real-time data of particle size estimation and fitness of consumption of contaminated water samples with sub-micron suspended particulate matter, which are difficult to assess via visual inspection. The developed set-up efficiently estimates the presence of suspended particulate matter including micro-organism to a level of 48 ppm (and hence defines the Limit of Detection of the system) which is well below the WHO level of 300 ppm in drinking water [27]. Water samples with coarser particles will be easier to identify and screen for consumption visually have not been included in this study.

8.2. Materials and Methods:

8.2.1. Cast Screen:

An optically backlit cast screen was used to draw the Red and Blue dots. The 220 VAC LED lamp was purchased from Philips and was fitted with an optical diffuser to block the direct beam saturating the receiver (camera). The dots of 1 cm diameter were printed from a calibrated true color printer (HP 2280). The wavelengths corresponding to individual colors were determined from the reverse calculation of the RGB value with wavelength correlation. The submersible camera (QAWACHH) was purchased online. The "Y-camera" app was used to acquire live images on a laptop or smartphone. Quartz cuvette was held in between as a sample holder ensuring a clear field of view of the cast screen through the sample.

8.2.2. Preparation of Samples:

The same quality milk samples were prepared at various concentrations starting from 1 μL to 40 μL in 1 mL of whole raw milk. The purchased sample was maintained at the highest

purity level to the best of knowledge. The standard pipetting apparatus (Accupipet) was used to extract the exact amount of solution under test.

8.2.3. Camera Characterization:

Computer vision mainly suffers from the problem of auto-brightness and auto saturation of pixels [28]. This leads to unequal referencing of data under various ambient light conditions. However, the choice of camera was made to be able to manually adjust the focus and exposure. Moreover, important considerations were taken to ensure submerged condition water protection for electronics and camera optics. To tackle this problem, a mobile endoscope camera enabled with in-built wireless LAN was used to capture images and transfer them to a distant computer or mobile in real-time.

8.2.4. Development of Low-Cost Instrument and Its Working Principle:

The working principle of this device is primarily based on the scattering and absorption of light by suspended particulate matter in a colloidal solution. Figure 8.1 shows the

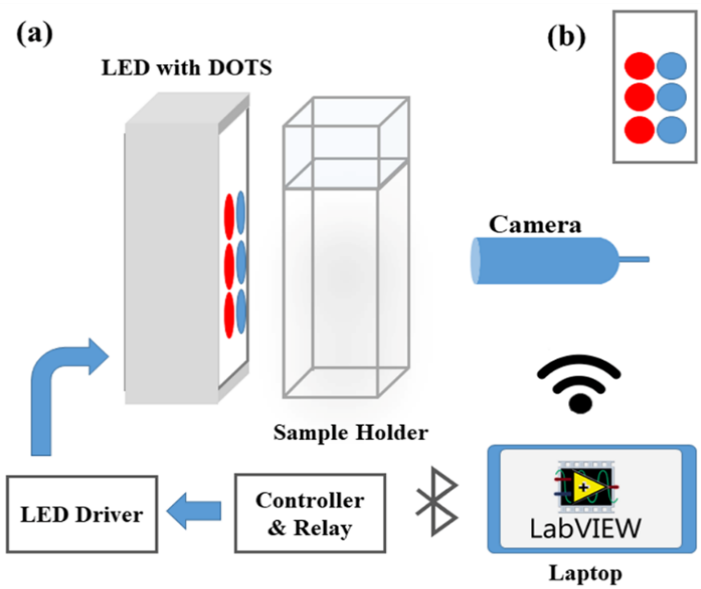

Figure 8.1: *(a) Schematic of the experimental arrangement for measuring optical signals from backlit cast screen (b) The dots of particular color representing the various segments of visible spectra.*

schematic diagram of the experimental arrangement. A backlit screen (diffusor) has been used as a cast screen. Two colors Red and Blue have been utilized as a marker of distinctly apart wavelength with no overlap of the spectrum. Light from the screen travels to the wireless camera after interacting with the sample in the cuvette. The camera has been strategically placed keeping in mind the view angle to cover both dots which are kept ensuring equal illumination behind both. The camera can be kept submerged under real-life situations and is enabled with a wireless LAN to ensure remote monitoring of the sample. Light traveling from the screen will suffer absorption by the sample guided by Beer-Lambert law. However, light traveling at the edge of the sample will suffer multiple reflections and will result in blurring of the edges as depicted conceptually in Figure 8.2(a). The

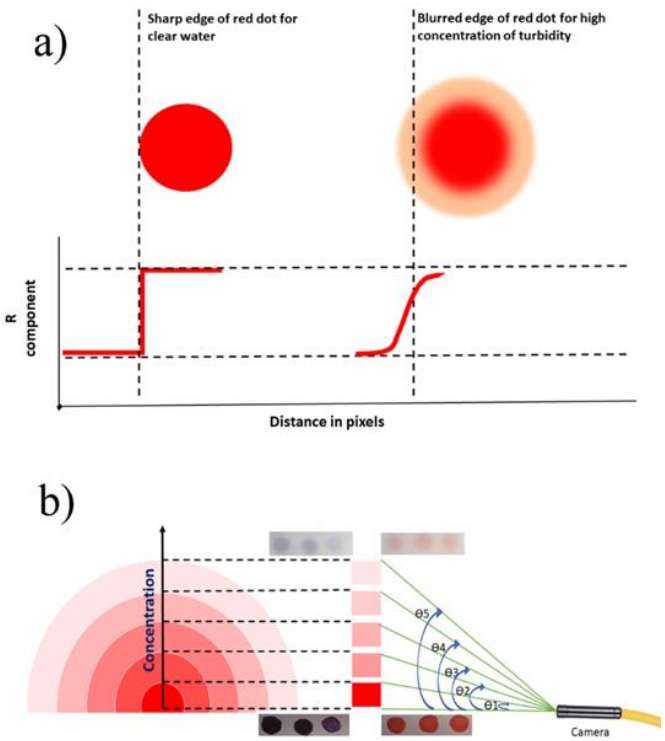

Figure 8.2: *a) Schematic of the image analysis method. Clearwater image of a dot as seen by a camera. The pixel intensity plot relative to the pixel position gives a sharp rising edge of a pulse function. Pixel intensity plot of turbid water and schematic of turbid water image b) Schematic of the relationship of blurring the edge of acquired images in turbid water.*

indigenously developed machine-computer interface will acquire live images and will do a

pixel analysis of the entire image frame to quickly calculate the amount of light absorbed as well as particle size estimation of the dominant component. Figure 8.2(b) shows the pattern of fade experienced by the edge of the image as one moves away from the center of the circle.

8.2.5. Bacterial Growth Curve:

The bactericidal activity is performed using MRSA *(*methicillin-resistant *Staphylococcus aureus)* bacteria cells. The cells are cultured in a Luria Broth (LB) medium under an incubator shaker at 37°C for 24 Hrs. The optical density of freshly grown overnight culture is fixed to 0.1 in LB medium initially. The culture is then put in a cuvette and incubated at 37°C with shaking for 9 Hrs. The absorbance is taken at every hour interval and plotted against time with baseline correction. The minimum detectable concentration of MRSA was determined using the onset of the growth curve. To estimate the limit of detection (LOD) of the suspended micro-organism (MRSA), we have converted the concentration of the micro-organism in the media from CFU/mL to ppm unit

8.2.6. Crystal Violet (CV) Staining Assay:

The freshly diluted culture of MRSA is spread over a biofilm and kept in an incubator at 37°C for 24 Hrs. Then, 1% of CV solution is spread over biofilm and incubated for 3 Hrs. After washing with water, the biofilm is exposed under a microscope (Leica digital inverted microscopes DMI8).

8.3. Results and Discussion:

The acquired video is analyzed frame by frame. Individual frames were performed a raster scan for pixel RGB information. Figure 8.3(a) shows the intensity plot of Red value (from

RGB analysis) obtained from Red-coloured dot. Similar results were obtained from the blue dot after extraction of blue value (from the RGB analysis) as evident from Figure 8.3(b).

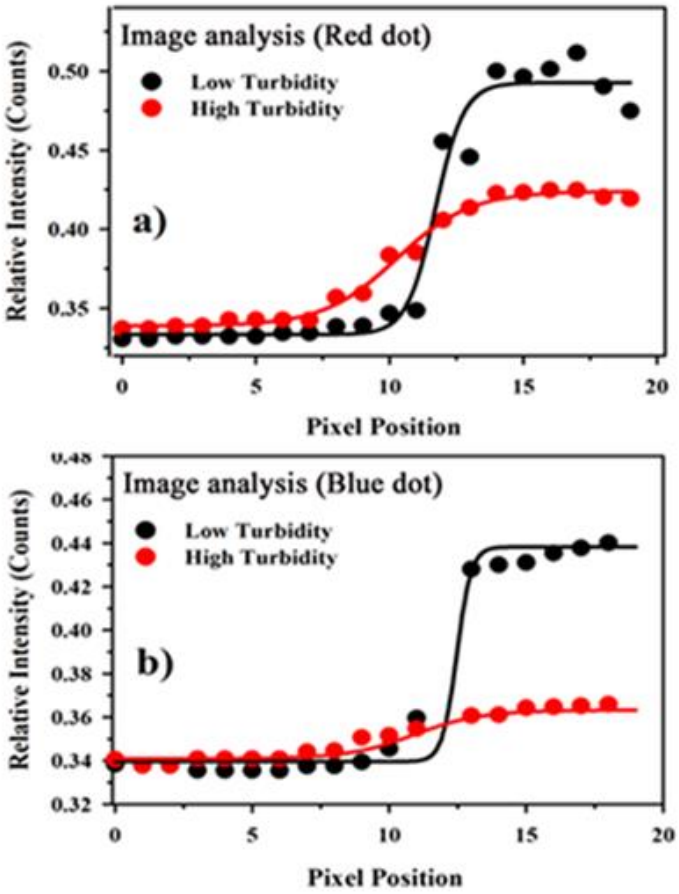

Figure 8.3: *a) Pixel intensity plot of acquired images of the Red dot in clear and turbid water and their respective Boltzmann fitting (b) Pixel intensity plot of acquired images of the Blue dot in clear and turbid water and their respective Boltzmann fittings (solid lines).*

The curves were fitted with a sigmoidal function. The fitting parameters obtained were found to be markers of absorption and scattering parameters of the sample under test. In the fitted equation (Eq. 8.1),

$$y = A_2 + \frac{(A_1 - A_2)}{\left(1 + e^{\left({}^{(x-X_0)}/_{dx}\right)}\right)} \qquad \textbf{(8.1)}$$

the value of X_0 obtained from the fitting function from individual curves is plotted against concentration for light red n blue dots as shown in Figure. 8.4(a & b) respectively.

The parameter is found to be indicative of the broadening of the edges due to the Rayleigh scattering of optical signals by the suspended particulate matter.

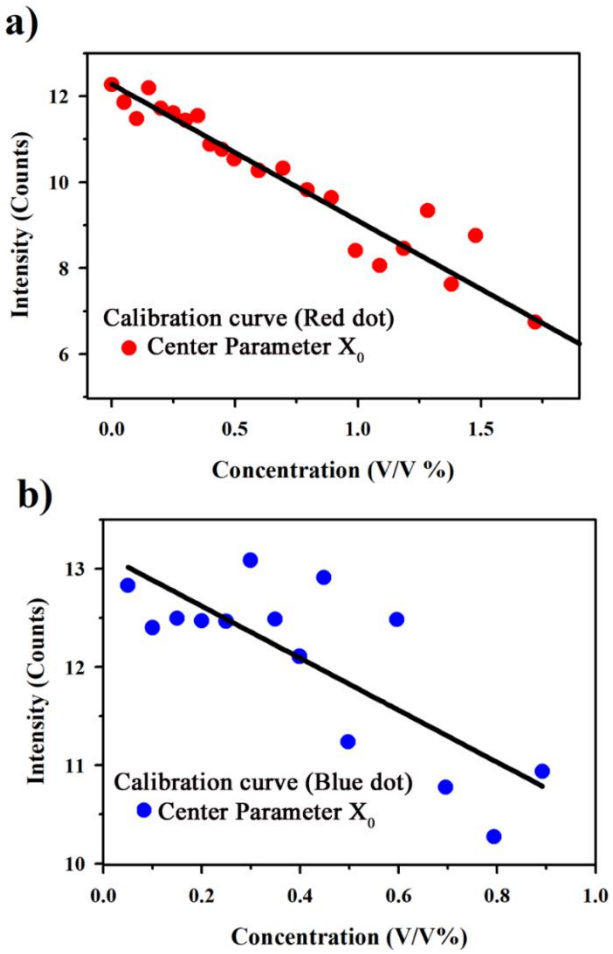

Figure 8.4: *a) Plot of fitted center parameter X_0 with concentration for red dot b) Plot of fitted center parameter X_0 with concentration for the blue dot.*

The pixel profile plot is expected to show a shift of intensities towards the negative X-axis to represent the broadening to the coloured dot on the left edge. This was confirmed by plotting the X_0 profile with concentration as shown in Figure 8.3(a & b). The curve clearly shows the linearly decreasing profile with increasing concentration suggesting a significant broadening of edges which is a signature of the number and size distribution of colloidal substance present in an optically turbid solution. Hence, the broadening of edges becomes the signature of the number of scattering materials present in the colloidal suspension.

The diameter of particles in colloidal suspension can be estimated from the following well known Rayleigh scattering equation Eq. 8.2. The intensity *I* of light scattered by any one of the small spheres of diameter *d* and refractive index n from a beam of unpolarized light of wavelength λ and intensity I_0 is given by

$$I = I_0 \frac{1 + cos^2\theta}{2R^2} (\frac{2\pi}{\lambda})^4)(\frac{n^2 - 1}{n^2 + 1})^2(\frac{d}{2})^6 \quad (8.2)$$

where *R* is the distance to the particle and θ is the scattering angle. Our experimental set-up dictates the use of two distinct wavelengths which was derived by conversion of RGB parameters to respective colors and further to specific wavelengths. The derived wavelengths were found to be λ = 700 nm for red color and λ=450 nm for blue color. The above equation (ii) can be re-written as the following:

$$d^6 = \frac{1}{(1 + cos^2\theta)(\frac{m^2 - 1}{m^2 + 2})^2} \frac{8\,R^2\lambda^4}{\pi^4} \frac{I}{I_0} \quad (8.3)$$

Therefore,

$$d^6 = K\,\frac{I}{I_0} \quad (8.4)$$

Where K is the constant and is governed by the equation

$$K = \frac{1}{(1 + cos^2\theta)(\frac{m^2 - 1}{m^2 + 2})^2} \frac{8\,R^2\lambda^4}{\pi^4} \quad (8.5)$$

After calculation using the above-mentioned values of parameters we get,

k=2.589 X 10^{-30} for blue (considering λ_{Blue}= 450nm, R=4mm and ($1+cos^2\theta$) =1.99952) and

k = 1.516 X 10^{-29} for red (considering λ_{Red}= 700nm, R=4mm and ($1+cos^2\theta$) =1.99956)

$$6 \log d = \log k + \log \frac{I}{I_0} \tag{8.6}$$

$$6 \log d = \log k - \log \frac{I_0}{I} \tag{8.7}$$

The term log $\frac{I_0}{I}$ is the signature of Beer-Lambert law which is synonymous with the parameter (A_2-A_1) of our fitting function. From equation Eq 8.7 we have calculated out for 450 nm wavelength as 252 nm and for 700 nm wavelength to be 730 nm which is in very close approximation with the standard DLS data as shown in Figure 8.5. indicating the variation of the diameter size of the dominant scatterer present in the sample with increasing concentration.

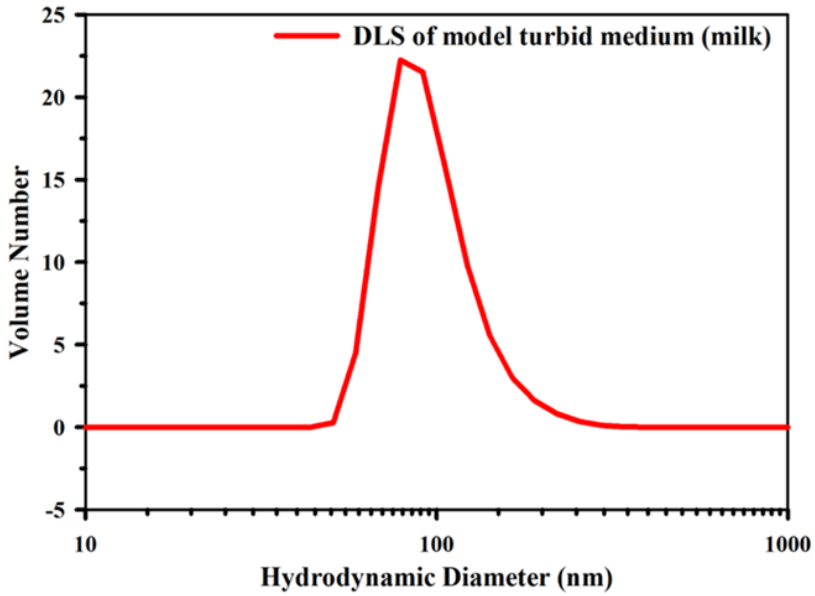

Figure 8.5: *DLS data of the fitting function of a sample colloidal solution (Milk).*

It was found that the diameter estimated using our set-up was in close agreement with the results from the DLS using the gold standard instrument. The fitting parameter (A_2-A_1) represents the extinction coefficient of the light. The amount of light traveling from the screen to the camera suffers absorption and scattering from the sample media. The difference of pixel information from normal spots to colored dotted spots represents the amount of light

lost during forwarding travel towards the camera. The two dots represent two dominant wavelengths and carry spectroscopic information relating to the colloidal sample. (A_2-A_1) is an indicative parameter towards the Optical Density of the sample governed by Beer lambert's law as shown in Figure 8.6(a & b). The choice of milk as a simulation of turbid

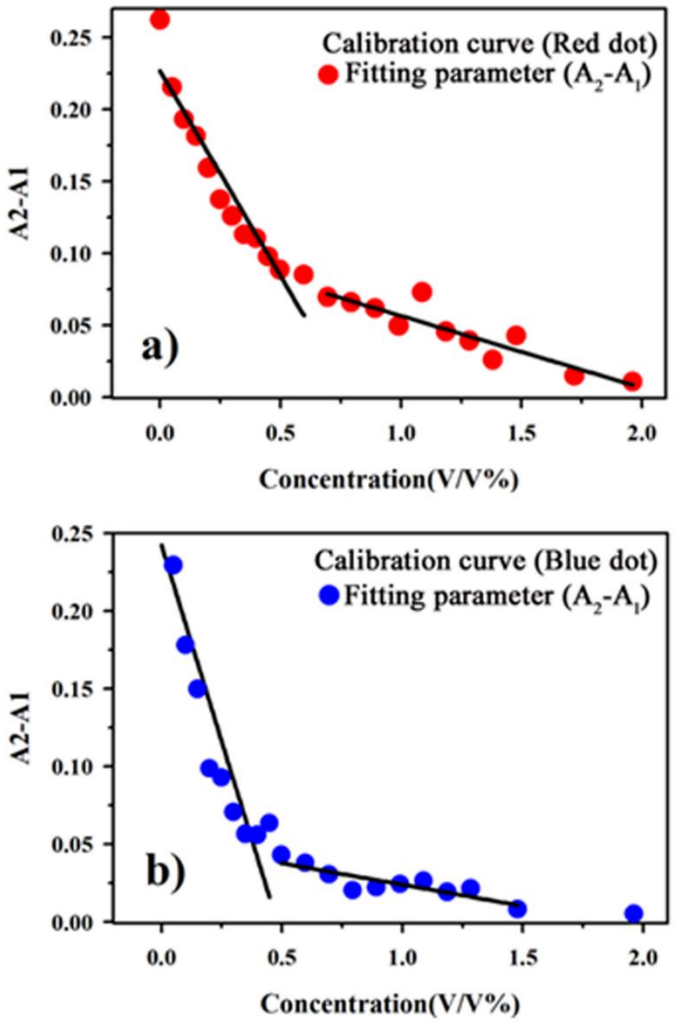

Figure 8.6: *a): Plot of the fitted parameter indicating a difference of initial and final amplitudes (A_2-A_1) and its dual linear fitting function for red dot (b) Plot of the fitted parameter indicating a difference of initial and final amplitudes (A_2-A_1) and its dual linear fitting function for the blue dot.*

water samples was found to be appropriate as we found a substantial similarity between particle size estimation from DLS instrument using the refractive index of various particles found in real-world water samples e.g., silica with the same.

Figure 8.7 shows the comparison of number concentration data obtained via DLS instrument using the refractive index of silica and milk respectively. Using our set-up, the

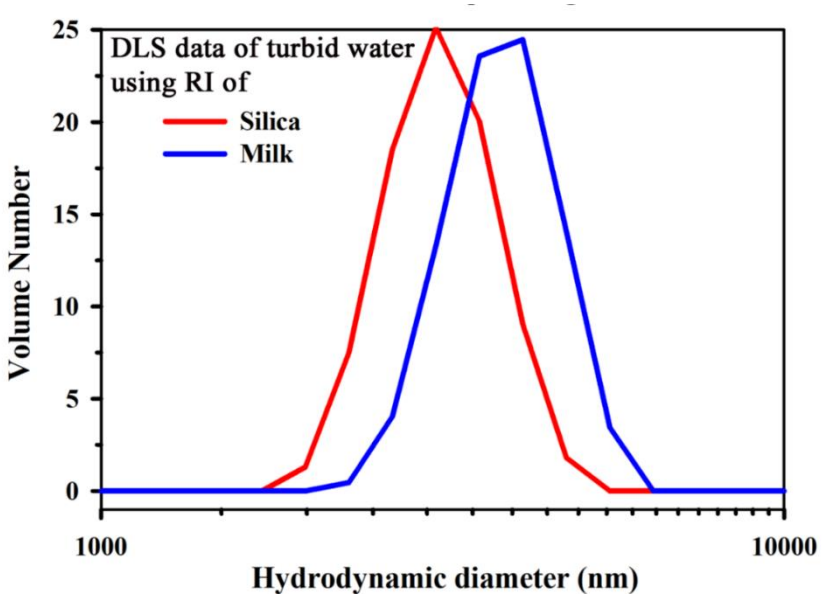

Figure 8.7: *Particle size distribution of turbid water samples collected locally and measured with DLS using refractive index (RI) of silica and milk respectively.*

effective diameters were found to be 6.8 µm using blue dot whereas using the red dot we arrived at the diameter of 10.9 µm. Once again better approximation was observed using a blue dot depicting the effectiveness of the set-up in a lower range of visible wavelengths. Figure 8.8 attributes the standardized growth curve of MRSA.

Herein, after the short (of 1 Hr) lag phase, optical density is exponentially increased up to 8 Hrs (log phase). The measurement of population growth is also manifested by image processing of red and blue dots. It is found that the growth curve exhibited by the blue dot showed much higher sensitivity and quick response to the growth of MRSA. However, it also exhibits quick saturation commensurate with a standardized growth curve. In contrast, the response obtained from the Red curve is found to be less responsive compared to the standard growth curve but showed no signs of saturation with increasing time. It can be concluded that from this strategy, we can get two sensing curves, one will better sensitivity

as well as a response but the lower dynamic range and the other with a lesser response but with a wider dynamic range. The bacterial growth curve was acquired using blue and red dot images. The minimum detectable concentration from the blue curve was found to be 48 ppm and the corresponding red curve was found to be 448 ppm. The LOD for the gold standard method was found to be 52 ppm. The average hydrodynamic diameter of MRSA is found to

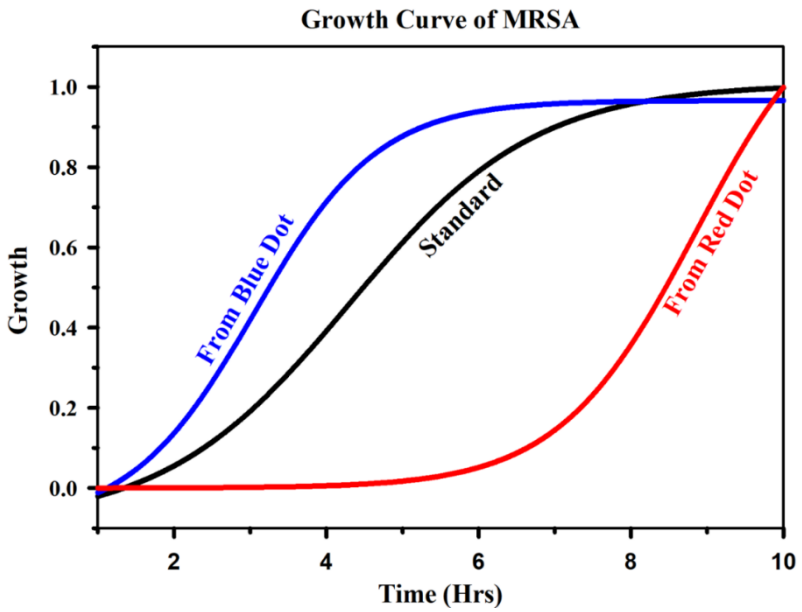

Figure 8.8: *Growth curve as obtained from the standard process in comparison to the developed strategy.*

be 1 µm from DLS as evident from Figure 8.9(a). As shown in Figure 8.9(b) the microscopic image of MRSA designates the cell diameter is approximately 0.8 µm which is in good agreement with our findings of 5.6 µm from our developed technique. It is to be noted the values are sometimes over-estimated due to the accumulation of multiple molecules as shown in Figure 8.9(b). This seems to be a good trade-off considering the cost-effectiveness and portability of the developed device.

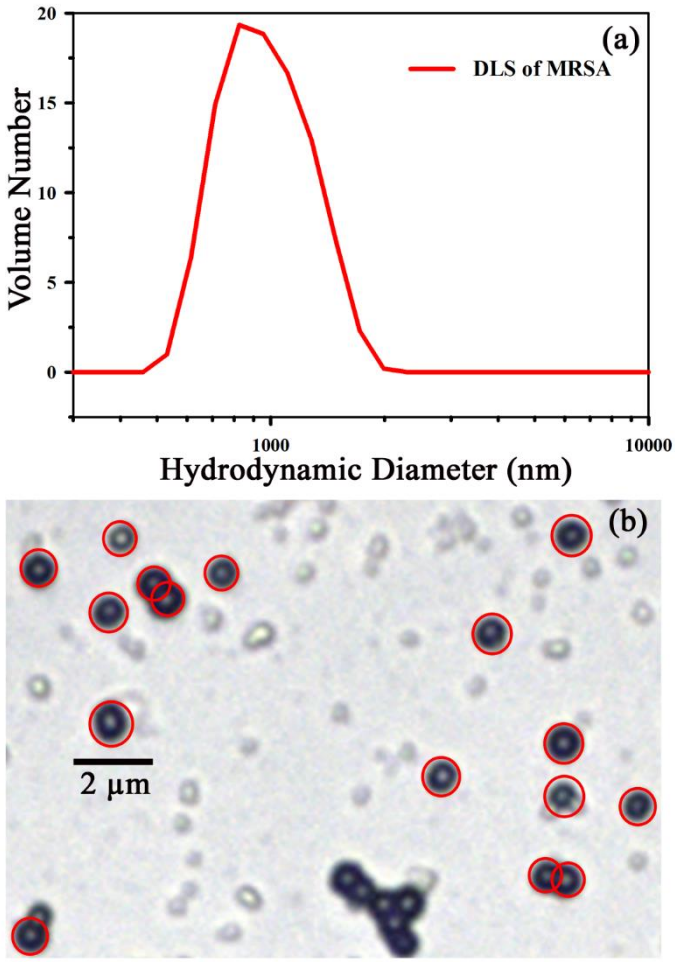

Figure 8.9: *(a) DLS data of MRSA exhibiting hydrodynamic diameter around 1 micron. (b) Microscopic image of MRSA confirming the diameter of around 1 micron.*

8.4. Conclusion:

In this work, we have presented a simple, innovative, and cost-effective technique involving the analysis of a video captured from a camera and estimate the amount of turbidity and also suspended particle size. The data have been analyzed using an indigenously developed software for online analysis of the model turbid medium. The set-up is found to be effective in calculating the above-mentioned parameters quickly and with a fair amount of accuracy. We also have investigated the possibility of assessment of bacterial presence in water with a fair amount of accuracy. We hope the developed strategy with quick, easy, and

precise determination of water quality with reasonably low LOD of suspended particulate matter (48 ppm) would offer an affordable alternative in a low resource setting for developing countries. The technology can be further applied to assess air quality and visibility assessment in a foggy atmosphere. However, more experimentation is required before the same can be established.

References

[1] M. Wang, M. Webber, B. Finlayson, J. Barnett, Rural industries and water pollution in China, J. Environ. Manage. 86 (2008) 648.

[2] H.S. Gorman, Redefining efficiency: Pollution concerns, regulatory mechanisms, and technological change in the US petroleum industry, 2001, Ohio, The University of Akron Press.

[3] K. Burningham, D. Thrush, Pollution concerns in context: A comparison of local perceptions of the risks associated with living close to a road and a chemical factory, J. Risk Res. 7 (2004) 213.

[4] E. Thomas, K. Wickramasinghe, S. Mendis, N. Roberts, C. Foster, Pollution concerns in context: A comparison of local perceptions of the risks associated with living close to a road and a chemical factory, BMC Public Health 15 (2015) 650.

[5] W.A. Suk, H. Ahanchian, K.A. Asante, D.O. Carpenter, F. Diaz-Barriga, E.-H. Ha, X. Huo, M. King, M. Ruchirawat, E.R. da Silva, Environmental pollution: An under-recognized threat to children's health, especially in low-and middle-income countries, Environ. Health Perspect. 124 (2016) A41.

[6] E.W. Kimani-Murage, A.M. Ngindu, Quality of water the slum dwellers use: The case of a Kenyan slum, J. Urban Health 84 (2007) 829.

[7] R.H. Dwight, L.M. Fernandez, D.B. Baker, J.C. Semenza, B.H. Olson, Estimating the economic burden from illnesses associated with recreational coastal water pollution-A case study in Orange County, California, J. Environ. Manage. 76 (2005) 95.

[8] R. Li, M. Dong, Y. Zhao, L. Zhang, Q. Cui, W. He, Assessment of water quality and identification of pollution sources of plateau lakes in Yunnan (China), J. Environ. Qual. 36 (2007) 291.

[9] E. Lawson, Physico-chemical parameters and heavy metal contents of water from the mangrove swamps of Lagos Lagoon, Adv. Biol. Res. 5 (2011) 8.

[10] R. Ramalho, J. Cunha, P. Teixeira, P.A. Gibbs, Improved methods for the enumeration of heterotrophic bacteria in bottled mineral waters, J. Microbiol. Methods 44 (2001) 97.

[11] G. Sadeghi, M. Mohammadian, M. Nourani, M. Peyda, A. Eslami, Microbiological quality assessment of rural drinking water supplies in Iran. Journal of agriculture & social sciences, J. Agric. Soc. Sci. 3 (2007) 31.

[12] M. Farré, D. Barceló, Toxicity testing of wastewater and sewage sludge by biosensors, bioassays and chemical analysis, TrAC Trends Analyt. Chem. 22 (2003) 299.

[13] T.H.Y. Tebbutt, Principles of water quality control, 1997, Oxford, Elsevier.

[14] D.R. Lenat, Water quality assessment of streams using a qualitative collection method for benthic macroinvertebrates, J. North Am. Benthol. Soc. 7 (1988) 222.

[15] B. O'Flynn, R. Martinez-Catala, S. Harte, C. O'Mathuna, J. Cleary, C. Slater, F. Regan, D. Diamond, H. Murphy, SmartCoast: A wireless sensor network for water quality monitoring, 2007. Dublin, IEEE.

[16] T.P. Lambrou, C.C. Anastasiou, C.G. Panayiotou, M.M. Polycarpou, A low-cost sensor network for real-time monitoring and contamination detection in drinking water distribution systems, IEEE Sens. J. 14 (2014) 2765.

[17] M.D. Johnston, A simple and rapid test for quality control of liquid media, using the bioscreen microbiological growth analyser, J. Microbiol. Methods 32 (1998) 37.

[18] B. Ouyang, F.R. Dalgleish, F.M. Caimi, T.E. Giddings, J. Shirron, A.K. Vuorenkoski, W. Britton, B. Metzger, B. Ramos, G. Nootz, Compressive sensing underwater laser serial imaging system, J. Electron. Imaging 22 (2013) 021010.

[19] D. Selmo, F. Sturt, J. Miles, P. Basford, T. Malzbender, K. Martinez, C. Thompson, G. Earl, G. Bevan, Underwater reflectance transformation imaging: A technology for in situ underwater cultural heritage object-level recording, J. Electron. Imaging 26 (2017) 011029.

[20] A.P.H. Association, A.W.W. Association, Standard methods for the examination of water and wastewater, J. Am. Public Health Assoc. 1989.

[21] P.D.L.S.L. Shujing, M. Zhihua, The application of watercolor remote sensing in general management of coast zone, spacecraft recoery & remote sensing 2 (2001) 1.

[22] V. Barale, Sea surface colour in the field of biological oceanography, Int. J. Remote Sens. 12 (1991) 781.

[23] L. Goddijn, M. White, Using a digital camera for water quality measurements in Galway Bay, Estuar. Coast. Shelf Sci. 66 (2006) 429.

[24] K. Kallio, T. Kutser, T. Hannonen, S. Koponen, J. Pulliainen, J. Vepsäläinen, T. Pyhälahti, Retrieval of water quality from airborne imaging spectrometry of various lake types in different seasons, Sci. Total Environ. 268 (2001) 59.

[25] B. Zion, The use of computer vision technologies in aquaculture-A review, Comput. Electron. Agric. 88 (2012) 125.

[26] A. Rompré, P. Servais, J. Baudart, M.-R. De-Roubin, P. Laurent, Detection and enumeration of coliforms in drinking water: Current methods and emerging approaches, J. Microbiol. Methods 49 (2002) 31.

[27] W.H. Organization, Silver in drinking-water: Background document for preparation of who guidelines for drinking-water quality, 2 (2003) 1.

[28] J. Hu, O. Gallo, K. Pulli, X. Sun, HDR deghosting: How to deal with saturation?, IEEE Conf. Comp. Vision Patt. Recog., 2013, 1163.

List of Publications

Publications in Peer-Reviewed Journals:

[1] **S. Singh**, A. Halder, O. Sinha, N. Chakrabarty, T. Chatterjee, A. Adhikari, P. Singh, D. Shikha, R. Ghosh, A. Banerjee, Spectroscopic studies on the biomolecular recognition of toluidine blue: key information towards development of a non-contact, non-invasive device for oral cancer detection, Front. Oncol. 10 (2020) 2293.

[2] **S. Singh**, A. Halder, S.A. Mohid, D. Bagchi, O. Sinha, A. Banerjee, P.K. Sarkar, A. Bhunia, S.K. Ghosh, A. Mitra, Nonthermal atmospheric plasma-induced cellular envelope damage of staphylococcus aureus and candida albicans biofilms: spectroscopic and biochemical investigations, IEEE Trans. Plasma Sci. 48 (2020) 2768.

[3] **S. Singh**, A. Halder, O. Sinha, P.K. Sarkar, P. Singh, A. Banerjee, S.A. Ahmed, A. Alharbi, R.J. Obaid, S.K. Ghosh, Nanoparticle-based 'turn-on' scattering and post-sample fluorescence for ultrasensitive detection of water pollution in wider window, PLoS One 15 (2020) e0227584.

[4] **S. Singh**, N. Polley, A. Mitra, S.K. Pal, Spark spectrometry of toxic smokes: towards a portable, inexpensive, and high-resolution environment monitoring instrument, Clean Technol. Environ. Policy 16 (2014) 1703.

[5] **S. Singh**, A. Halder, A. Banerjee, M.N. Hasan, A. Bera, O. Sinha, S.K. Ghosh, A. Mitra, S. Pal, An Optical Scattering Based Cost-Effective Approach Towards

Quantitative Assessment Of Turbidity And Particle Size Estimation In Drinking Water Using Image Analysis, Asian J. Converg. Technol. 7 (2020) 1.

[6]* **S. Singh**, B. Saha, S.S. Sinha, S.K. Pal, Construction of a low-cost laser-based multiplexed spectrometer: a potential probe for environmental pollution monitoring, Int. J. Environ. Waste Manag. 9 (2012) 388.

[7]* N. Das, N. Bhattacharyya, **S. Singh**, A. Halder, D. Shikha, S.K. Pal, Biosphere atmosphere exchange of CO2, H2O vapour and energy during spring over a high altitude Himalayan forest in eastern India, Jpn. J. Appl. Phys. 59 (2020) 96503

[8]* N. Bhattacharyya, **S. Singh**, A. Halder, A. Adhikari, R. Ghosh, D. Shikha, S. K. Tripathi, A. K. Mallick, P. Mondal & S. K. Pal, An Energy-Resolved Optical Non-invasive Device Detects Essential Electrolyte Balance in Humans at Point-of-Care, Jpn. Trans. Indian Nat. Acad. Engineer., 15 (2021) 1087

[9]* A. Halder, A. Aniruddha, G. Ria, **S. Singh**, B. Amrita, G. Nilanjana, A.M. Bhattacharya, M. Shrabani, C. Prantar, B. Debasis, Large scale validation of a new non-invasive and non-contact bilirubinometer in neonates with risk factors, Sci. Rep. 10 (2020) 11149.

[10]* A. Halder, M. Banerjee, **S. Singh**, A. Adhikari, P.K. Sarkar, A.M. Bhattacharya, P. Chakrabarti, D. Bhattacharyya, A.K. Mallick, S.K. Pal, A novel whole spectrum-based non-invasive screening device for neonatal hyperbilirubinemia, IEEE J. Biomed. Health Inform. 23 (2019) 2347.

[11]* A. Halder, **S. Singh**, A. Adhikari, P. Singh, P.K. Sarkar, U. Pal, R. Ghosh, D. Shikha, Y.S. Solanki, M. Agarwal, Selective and fast responsive sensitized micelle for

detection of fluoride level in drinking water, ACS Sustain. Chem. Eng. 7 (2019) 16355.

[12]* A. Halder, **S. Singh**, A. Adhikari, S. Ghosh, D. Shikha, D. Saha, R. Chakraborty, A. Kundu, S.K. Tripathi, S.K. Pal, NaLiK, an self-developed device for rapid, reliable and simultaneous assessment of sodium, lithium and potassium for management of fluid balance and bipolar disorder in human subjects, J. Anal. Atom. Spectrom. 34 (2019) 1875.

[13]* A. Halder, D. Shikha, A. Adhikari, R. Ghosh, **S. Singh**, T. Adhikari, S.K. Pal, Development of A Nano-Sensor (FeNSOR) Based Device for Estimation of Iron Ions in Biological and Environmental Samples, IEEE Sens. J. 20 (2019) 1268.

[14]* N. Polley, **S. Singh**, A. Giri, P.K. Mondal, P. Lemmens, S.K. Pal, Ultrafast FRET at fiber tips: Potential applications in sensitive remote sensing of molecular interaction , Sens. Actuators B: Chem. 210 (2015) 381.

[15]* N. Polley, S. Saha, **S. Singh**, A. Adhikari, S. Das, B.R. Choudhury, S.K. Pal, Development and optimization of a noncontact optical device for online monitoring of jaundice in human subjects, J. Biomed. Opt. 20 (2015) 67001.

[16]* N. Polley, **S. Singh**, A. Giri, S.K. Pal, Evanescent field: a potential light-tool for theranostics application, Rev. Sci. Instrum. 85 (2014) 33108.

[17]* L. Roy, A. Halder, **S. Singh**, J. Patwari, P. Singh, K. Bhattacharya, S. Mondal, S.K. Pal, Spectroscopy of an intrinsic fluorophore in animal and plant milk for potential identification of their quality, J. Dairy Sci. 103 (2020) 1366.

[18]* K. Kole, A. Halder, **S. Singh**, A. Samanta, S. Das, A.K. Kundu, D. Bhattacharyya, S.K. Pal, S. Jana, Chromogenic-Functionalized Silica Nanoflower Composites for the Detection of Carbon Dioxide, ACS Appl. Nano Mater. 3 (2020) 4321.

[19]* D. Mukherjee, P. Singh, **S. Singh**, D.S. Roy, S. Singha, U. Pal, J. Sengupta, R.J. Obaid, S.A. Ahmed, T.S. Dasgupta, R. Das, S.K. Pal, Host assisted molecular recognition by human serum albumin: Study of molecular recognition controlled protein/drug mimic binding in a microfluidic channel, Int. J. Biol. Macromol. 176 (2021) 137.

[20]* A. Chatterjee, N. Pan, T. K. Maji, S. S. Pasha, **S. Singh**, S. A. Ahmed, J. T. Al-Thakafy, S. K. Pal, Highly Sensitive Optical Sensor for Selective Detection of Fluoride Level in Drinking Water: Methodology to Fabrication of Prototype Device, Chem. Rxiv. 1 (2021) 1.

[21]* S. Mehta, **S. Singh**, A. Mitra, S.K. Ghosh, S. Raha, Modeling of Raindrop Size Distribution Observed Using Micro Rain Radar Over Darjeeling (27.05°N, 88.26°E): An Eastern Himalayan Region, S. Mehta, Pure Appl. Geophys. 177 (2020) 2959.

[22]* A. Chatterjee, A. Roy, S. Chakraborty, A.K. Karipot, C. Sarkar, **S. Singh**, S.K. Ghosh, A. Mitra, S. Raha, Biosphere atmosphere exchange of CO2, H2O vapour and energy during spring over a high altitude Himalayan forest in eastern India, Aerosol Air Qual. Res. 18 (2018) 2704.

[23]* S. Mehta, S.K. Mehta, **S. Singh**, A. Mitra, S.K. Ghosh, S. Raha, Characteristics of the z–r relationships observed using micro rain radar (MRR-2) over Darjeeling

(27.05°N, 88.26°E): a complex terrain region in the eastern Himalayas, Pure Appl. Geophys. 177 (2020) 4521.

[24]* D. Ray, **S. Singh**, S.K. Ghosh, S. Raha, Dynamic response of light absorption by PM2. 5 bound water-soluble organic carbon to heterogeneous oxidation, Aerosol Sci. Technol. 53 (2019) 1404.

[25]* S. Mehta, **S. Singh**, A. Mitra, S.K. Ghosh, S. Raha, Diurnal variation of the lower tropospheric water vapor observed using microwave radiometer over Darjeeling (27.05°N, 88.26°E), J. Indian Soc. Remote Sens. 47 (2019) 619.

[26]* T. Bhattacharyya, A. Chatterjee, S.K. Das, **S. Singh**, S.K. Ghosh, Study of fair weather surface atmospheric electric field at high altitude station in Eastern Himalayas, Atmos. Res. 239 (2020) 104909.

Book Chapters:

[27]* A. Halder, **S. Singh**, A. Adhikari, P.K. Sarkar, S.K. Pal, Development of spectroscopy-based medical devices for disease diagnosis in low resource point-of-care setting, Bioelectronics and Medical Devices, Elsevier, 2019, p. 483.

[28]* O. Sinha, **S. Singh**, A. Mitra, S. Ghosh, S. Raha, Development of a drowsy driver detection system based on EEG and IR-based eye blink detection analysis, Advances in Communication, Devices and Networking, Springer, 2018, p. 313.

* Not included in thesis.